Answers to Anonymous Referee #1

We thank the anonymous referee #1 for his/her constructive comments and suggestions that certainly have improved the manuscript significantly. We revised the manuscript according to his/her comments and the comments of anonymous referees #2 and #3. In the following,

- *referee's comments are given in italic*,
- our answers are outlined in normal format, and
- **textual changes in the manuscript are given in bold format**.

We would like inform the anonymous referee #1 about the following changes:

1. Driven by the specific comment (SC) #18 of anonymous referee #3 (SC3.18), we decided to drop scenario S4 from the analysis. The difference between the sub-adiabatic model (S3) and the modified one (S4) is that the latter accounts for the depletion of the liquid water content due to entrainment, precipitation, and freezing drops. Consequently, we wanted to check whether S4 captures better the vertical stratification of the modeled low-level clouds and, accordingly, if it approximates the CREs of the reference simulation with better accuracy. Since S4 does not provide any further insight, we now have decided to drop this scenario. However, we do confirm that, by considering all the case days in the analysis, we came to the same conclusions as for 3 June. As a confirmation, we updated the Tables and attached them at the end of this document. The referee is referred to Tables R1–R3.

2. In all scenarios, we decided to drop sub-case d, which employs two fixed values for the droplet number concentration representing the two modes in the corresponding histogram for 3 June 2016. This scenario separates clouds into a cluster with low/high clouds. Considering the vertical variability of the droplet number concentration, the latter clustering will link low clouds (within the boundary layer) with high N_d and, accordingly, high clouds with lower N_d values. Thus, for all scenarios, employing such values for N_d are able to approximate the reference radiative transfer simulation very well. Only the radiative transfer simulation that is supplied by the droplet number concentration weighted over the cloud geometrical extent, i.e., N_int (sub-case b) leads to smaller differences when compared to the reference simulation. However, we do confirm that, by considering all the case days into the analysis, we came to the same conclusions as for 3 June. Note that, for the latter case, the clustering was conducted on the mean N_int over all case days. As a confirmation, we updated the Tables and attached them at the end of this document. The referee is referred to Tables R1–R3.

3. We decided to add a new scenario as a replacement of sub-case d, whereby radiative transfer simulations are conducted for a mean vertical profile of the droplet number concentration over all case days. Tables R9–R11 summarize the new results. In brief, this scenario is considered as an improvement compared to the clustering case. The following parts were included within the text:

   Section 5.1.2: **Last but not least, by replacing the vertical profile of N_d by the**

mean profile of N_d over all case days (see Fig. 2), emulates the cloud radiative effects of the reference simulation quite well. Accordingly, scenario S4 slightly undersimates the mean SW CREs, with an mean error up to $-3.16\,\mathrm{W\,m^{-2}}$ and a RMSE up to $17.2\,\mathrm{W\,m^{-2}}$ for both BOA and TOA. In fact, this scenario outperforms the rest scenarios (S1–S3), except from the sub-case b (N_{int}) in all scenarios. For an illustration of the excellent linear correlation between the reference simulation and S4 by means of a bivariate kernel density (BKD) plot, the reader is referred to Fig. B1 in Appendix B. One can see that the CREs computed by these scenarios are in a very good agreement almost everywhere except towards larger values of the CREs in case of the SW radiation, with Pearson correlations larger than 0.977 for both BOA and TOA.

Section 6: **By employing a more representative profile for the N_d, i.e., a mean vertical profile of N_d over all case days leads to a rather good approximation; the RMSE is below $17.2\,\mathrm{W\,m^{-2}}$. This points to the need to better account for prognostic N_d calculations.**

Appendix B: **In sect. 5.1.2, by conducting idealized radiative transfer simulations, we estimated the impact of the representation of cloud properties in ICON-LEM on the cloud radiative effects (CREs). Special emphasis was given on identifying the droplet number concentration (N_d), which approximates the microphysical and radiative properties of low-level clouds as simulated by ICON-LEM (reference scenario). A radiative transfer simulation, which employs a mean vertical profile of N_d over all the case days (scenario S4), approximates the CREs of the reference scenario quite well. Figure B1 depicts the excellent linear correlation between the reference simulation and S4 by means of a bivariate kernel density (BKD)**.

4. Following the general comment of anonymous referee #2 for shortening the manuscript given the redundancy of many of the results shown in this study and his/her relevant specific comments (SC), i.e., (SC2.12) and (SC2.25):

   - We decided to drop Fig. B1. Figure B1 illustrates the bivariate kernel density (BKD) between the cloud optical thickness and the liquid water path on a logarithmic scale. Considering the comprehensive explanation given in Sect. 3.3.1, we decided that this illustration did not provide any additional information.
   - Figures 6 and 7 have been revised. Now, they illustrate results only for TOA (see Figs R2 and R3).
   - We now focus only on the rotational component analysis. The mention of the principal component analysis have been significantly reduced. In addition, we removed the relevant information from Table 3. For the updated version of the Table, the referees are referred to Table R5. Additionally, we replaced Figure 5 by Table R4. This table lists the contribution of each rotational component to the total variance.

Answers to general comments (GC) from referee #1 (GC1)

(GC1.1) *My major concern is that the simulations examined in this study are very limited (Page 8 Line 15-18). The authors conducted simulations using six case days, but actually looked at in details only the case of 3 June 2016. How general are they? Doesn't the vertical structure of adiabaticity depend strongly on the cloud regimes and types or their life-stage? In the present form of this paper, objectives are too narrow. The described relationship among cloud micro- and macrophysical properties and radiative effect using high resolution simulation may provide key suggestions on aerosol-cloud interactions, but the findings as they are, are by no means general. With some more simulation cases or a bit more analysis for all the case days in detail, I think this will make a publishable work.*

These days have been selected from the total set of available case days by the presence of suitable liquid water cloud fields and no known bugs in the used model version, which affect the representation of low-level clouds. We do agree that the vertical structure of adiabaticity depends on cloud regimes, types, and life-stage and, thus, it could be an interesting extension. However, due to the high horizontal resolution of ICON-LEM, for a single day, the number of "independent" cloudy columns are very large and complicates the investigation of such dependencies. Note here that the model output employed in this study, 3D HOPE data, has an output frequency of 15 min, while the domain size is limited to 45 km^2. For such studies, especially when it comes to life-stage, it would be better to use model data with higher output frequency, e.g., 1D profiles that are available every 10 sec. But, this is beyond the purpose of this study. However, we revised our manuscript according to the comments of anonymous referee #1 and the comments of anonymous referees #3 further extended our analysis over all days to improve the robustness of our results. Now, sections 3.2 and 5 outline our findings for all case days.

As we aforementioned, throughout this study, a special emphasis was given to 3 June 2016, because, regardless of the large variability in cloud properties for each day, it approximates best the mean properties over all the case days considered. Thus, the revision of these two plots did not require any significant textual alteration (see Fig. R1 and Fig. R2); only minor textual changes were made.

Answers to specific comments (SC) from referee #1 (SC1)

(SC1.1) *Section 2.3: Please describe the model resolution, domain size, as well as timestep used in the simulations. The general description of ICON-LEM on page 3 (L16-17 and L28-30) is confusing with regards to this.*

We revised the description of ICON-LEM (Section 2.1) according to this comment and the specific comment (SC) # 3 of anonymous referee #3 (SC3.3):

The ICON unified modeling framework was co-developed by the German meteorological service (DWD) and the Max Planck institute for meteorology (MPI-M) in order to support climate research and weather forecasting. Within the HD(CP)2 project, ICON was further extended towards large eddy simulations with realistic topography **and** open boundary conditions. This resulted in

ICON-LEM **deployed in restricted areas that are centered on Germany and the Tropical Atlantic [1]. The equations utilized by the model are based on the prognostic variables given by Gassmann and Herzog [2]. These variables comprise the horizontal and vertical velocity components, the density of moist air, the virtual potential temperature, and the mass and number densities of traces, e.g., specific humidity, liquid water, and different ice hydrometeors. A comprehensive description of the model and its governing equations is found in Dipankar et al. [3] and Wan et al., [4].** Concerning turbulence parameterization, the three-dimensional Smagorinsky scheme is employed [3]. The activation of cloud condensation nuclei (CCN) is based on the parameterization of Seifert and Beheng [5] and modified in order to account for the consumption of CCNs due to their activation into cloud droplets. The CCN concentration is then parameterized following the pressure profile and the vertical velocity [6].

Simulations are carried out for three different domains with 624 m, 312 m, and 156 m horizontal resolution. The model domains consist of 150 vertical levels, with resolutions ranging from ∼25 m to 70 m within the boundary layer, and from 70 m to 355 m further up until the top of the domain at 21 km. For each of the aforementioned grids, data is stored as one-dimensional (1D) profiles every 10 sec, two-(2D), and 3D snapshots [1]. In case of the 3D output, the simulation data is interpolated from the original grids (e.g., 156 m) to a 1 km grid, the 3D coarse data, and 300 m grid, the so-called HOPE data. The latter output has been created for the purpose of model evaluation with ground-based observations from the HD(CP)^2 Observational Prototype Experiment (HOPE) that took place near Jülich [7]**and is limited to a domain size of about ∼45 km^2. Note here that for the 2D and 3D output, data is stored at day- and night-time frequency. Day-time frequency begins at 06:00 UTC and lasts until 00:00 UTC, while night-time starts at midnight and lasts until 06:00 UTC. The 2D data is stored with a day-time and night-time frequency of 10 sec and 5 min, respectively. The 3D coarse data has day-time frequency of 10 min (1 hour at night-time). In this study, the 3D HOPE data has been used that is stored only at a day-time frequency of 15 min.**

(SC1.2) *Equation (7): It is better to add a sentence about the factor* 2/3*, rather than* 5/9*, citing relevant papers (e.g., Szczodrak et al., 2001; Wood and Hartmann, 2006; Lebsock and Su, 2014). Equations (14) and (15) as well.*

We revised section 2.6 according to this comment and the specific comment (SC) #4 of anonymous referee #3 (SC3.4). The following parts have been added:

P6 L24: **while the factor** 2/3 **is a scale factor resulting from the constant liquid water content and effective radius with height [8].**

P7 L21: **Compared to Eq. (7), Eq. (10) leads to a factor of** 5/9**, meaning that the sub-adiabatic liquid water path is** 5/6 **times the one of the vertically homogeneous model [9].**

P8 L11: **For vertically constant q_L and r_{eff}, this can be interpreted as the cloud optical thickness coming from the vertical homogeneous model (see Eq. 7). According to the sub-adiabatic cloud model, the cloud optical thickness is linked to the liquid**

water path and the effective radius [10],

$$\tau = \frac{9}{5}\frac{Q_{\mathrm{L}}}{\rho_{\mathrm{w}} \cdot r_{\mathrm{eff}}}$$

Alternatively, substituting r_{eff} from Eq. (13) in Eq. (15), the cloud optical thickness is given by,...

(SC1.3) *Figure 3 and caption: q_{L} -¿ Q_{L} or CLWP.*

Actually, Fig. 3 illustrates the mean liquid water content profile normalized over the cloud geometrical extent. Throughout the paper, liquid water content is denoted as q_{L}.

(SC1.4) *Figures 6, 7 and 8: The order of sub-figures is not consistent with the caption.*

The order of sub-figures has been revised for consistency.

(SC1.5) *Table 6: I found several mismatches between Table 6 and citing main text (e.g., P18 L16), which made reviewers very difficult to track...*

We apologize for the mismatches. We have now extended the analysis to all case days and, thus, tables and related text have been revised.

(SC1.6) *P23 L11-13: This sentence is too vague. Please raise more specific source of uncertainty, and describe how the scrutinization is required.*

After the additional insight given by anonymous referee #2 (see general comment 3, i.e., GC2.3) we have revised this part of the text as follows:

The vertical variability of the droplet number concentration was examined. **For all the case days**, above an altitude of **about** 2 km, values of N_{d} are about 200 cm^{-3} and are, thus, close to climatological values, while in the boundary layer, the double moment scheme predicts N_{d} values above 600 cm^{-3}. Such values are **regarded as** rather high compared to satellite remote sensing estimates [11, 12], **but such comparison is rather vague considering, firstly, the large uncertainties of the satellite-derived estimates of cloud droplet number concentration [12] and, secondly, they are not available in high resolution. However,** in situ observations, **which are considered to be the most accurate approach to determine N_{d},** suggest higher values and, hence, lie closer to those simulated by ICON-LEM. **Thus, by means of in situ observations, evaluation activities should be conducted for a better characterization of the droplet number concentration from remote sensing techniques. The latter will scrutinize the double-moment scheme implemented in ICON-LEM and could potentially lead to better simulations of cloud processes and radiation.**

We additionally revised the corresponding text in Section 3.2 as follows,

On the contrary, in situ observations suggest higher values of N_{d} and, accordingly, closer to those simulated by ICON-LEM. **Hence, efforts should be undertaken to further validate the cloud droplet number concentrations predicted by the double-moment scheme.**

(SC1.7) *P25 L12-L13: This sentence recommends double-moment cloud microphysics, but P23 L12 points weakness of the double-moment.*

After the insight given by the anonymous referee #2, the sentence at page 23, line 12, has been revised (see SC.6).

(SC1.8) *Appendix B: Please change the appendix title. Appendix section is not just a list of supporting materials. The current version does not have any explanation about the figures in the appendix (Appendix C as well).*

The Appendix B and C have been revised.

List of Figures

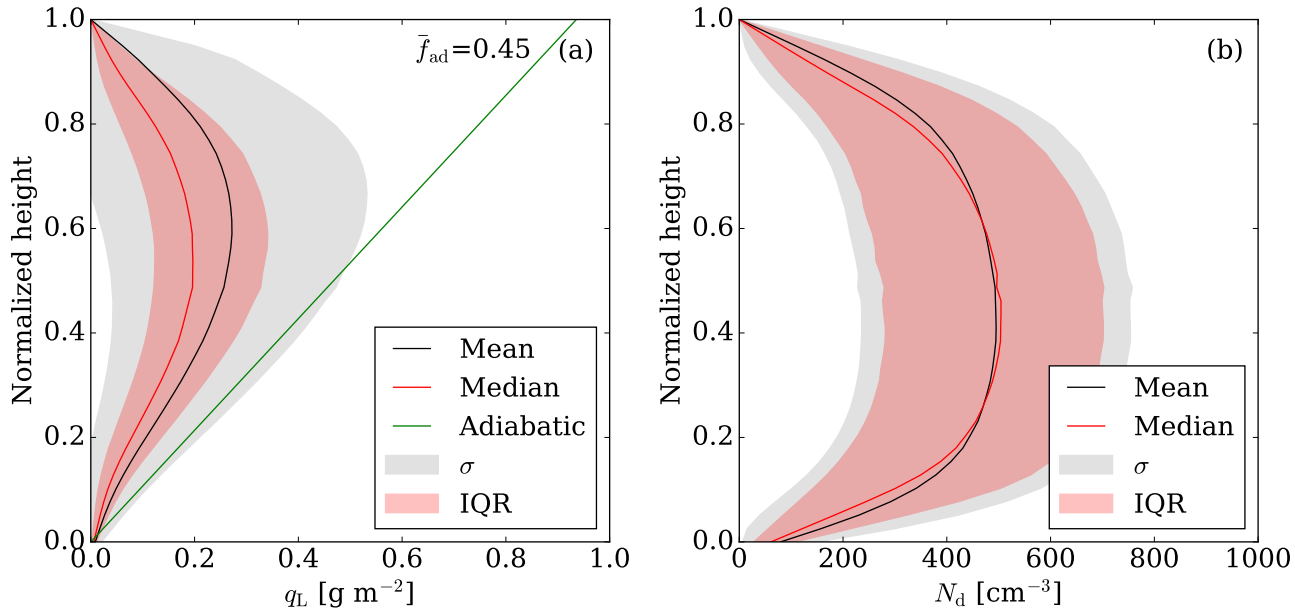

Figure R2: ICON-LEM simulated mean (a) q_L and (b) N_d profiles for all the case days on average. Profiles are normalized over height from the CBH to the CTH. Black lines denote the mean, red solid lines the median, gray shaded areas the standard deviation, red shaded areas the interquartile range (IQR), and the green solid line outline the mean adiabatic q_L profile characterized by a mean adiabatic fraction ($\bar{f}_{ad}$) of 0.45.

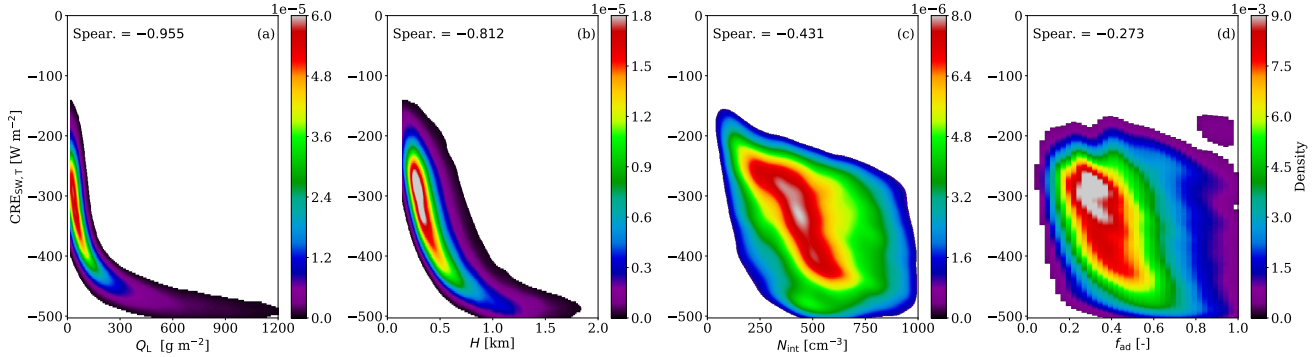

Figure R3: Bivariate kernel density (BKD) between the reference simulation (Ref.) and the cloud properties that are essential for the derivation of the cloud optical thickness that is one of the fundamental properties describing the SW cloud radiative effect. Panels illustrate the BKD between the $\mathrm{CRE_{SW,T}}$ and (a) Q_L, (b) H, (c) N_int, and (d) f_ad. The corresponding Spearman (Spear.) correlations are highlighted.

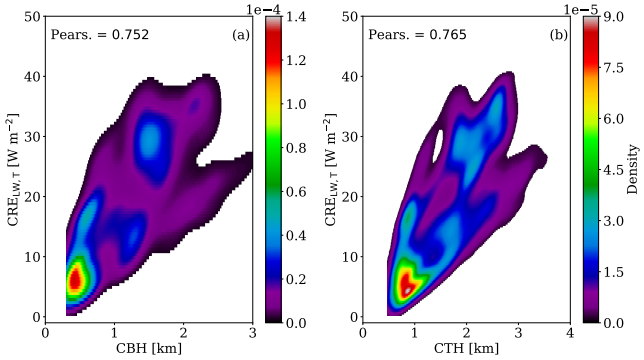

Figure R4: Bivariate kernel density (BKD) between the reference simulation (Ref.) and the cloud properties describing the LW cloud radiative effect at the TOA and (a) CBH and (b) CTH. The corresponding Pearson (Pears.) correlations are highlighted.

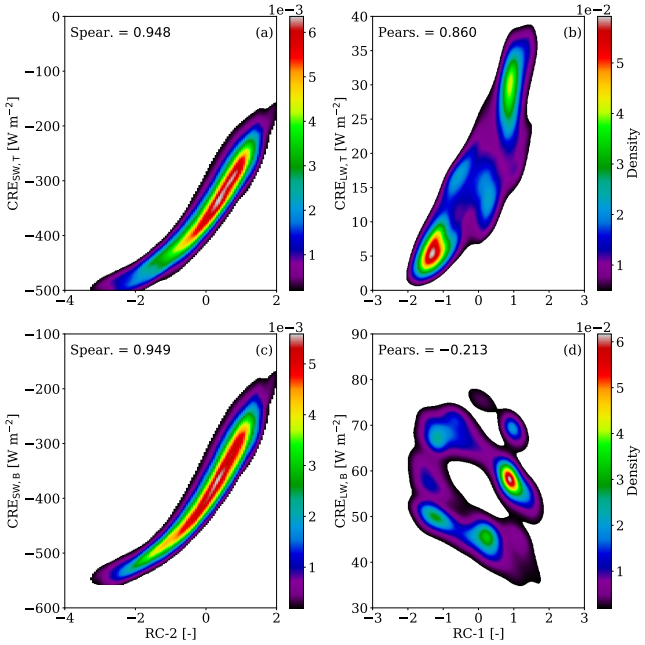

Figure R5: For the reference simulation (Ref.), bivariate kernel density (BKD) between $\mathrm{CRE_{SW}}$ and the second rotational component (RC-2) at (a) TOA, (c) BOA and between $\mathrm{CRE_{LW}}$ and the first rotational component (RC-1) at (b) TOA, (d) BOA. The corresponding Spearman (Spear.) and Pearson (Pears.) correlations are highlighted for the SW and LW radiation, respectively.

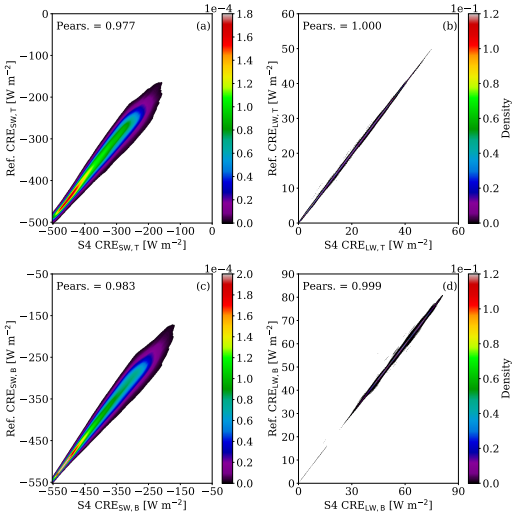

Figure R6: Bivariate kernel density (BKD) between the reference simulation (Ref.) and the scenario that employs the mean vertical N_d profile (S4). For the CREs, BKD are presented for the SW radiation at the TOA (a) and BOA (c), and for the LW radiation at the TOA (b) and BOA (d). The corresponding Pearson (Pears.) correlations are highlighted.

List of Tables

Table R1: Mean CRE ($\mathrm{W\,m^{-2}}$) for the SW radiation. Results are given as differences between the new scenario minus the reference simulation (Δ). The root mean square error (RMSE) in $\mathrm{W\,m^{-2}}$ and the Pearson (Pears.) correlation between the new scenarios and the reference simulation are also given.

Scen.	$\mathrm{CRE_{SW,B}}$			$\mathrm{CRE_{SW,T}}$		
	Δ	RMSE	Pears.	Δ	RMSE	Pears.
S1a	−39.2	46.4	0.960	−40.1	47.0	0.952
S1b	−7.04	11.7	0.995	−6.53	11.7	0.994
S1c	−2.59	23.4	0.964	−1.86	24.3	0.951
S1d	−6.57	17.6	0.982	−5.99	18.0	0.977
S2a	−26.1	39.2	0.943	−27.1	39.8	0.930
S2b	7.74	14.2	0.991	8.19	13.6	0.990
S2c	12.9	32.4	0.943	13.7	33.6	0.921
S2d	8.53	22.6	0.971	9.10	22.9	0.964
S3a	−31.1	41.4	0.950	−32.9	42.9	0.937
S3b	1.47	10.6	0.993	1.17	10.0	0.992
S3c	6.59	27.7	0.953	6.55	29.0	0.934
S3d	2.29	19.1	0.976	2.09	19.5	0.969
S4a	−28.7	40.1	0.947	−30.3	41.4	0.934
S4b	4.97	11.7	0.993	4.80	11.1	0.992
S4c	10.1	29.9	0.949	10.2	31.2	0.928
S4d	5.72	20.4	0.975	5.67	20.8	0.967

Table R2: Mean CRE ($\mathrm{W\,m^{-2}}$) for the LW radiation. Results are given as differences between the new scenario minus the reference simulation (Δ). The root mean square error (RMSE) in $\mathrm{W\,m^{-2}}$ and the Pearson (Pears.) correlation between the new scenarios and the reference simulation are also given.

Scen.	$\mathrm{CRE_{LW,B}}$			$\mathrm{CRE_{LW,T}}$		
	Δ	RMSE	Pears.	Δ	RMSE	Pears.
S1a	−0.11	0.48	0.999	−0.04	0.19	1.000
S1b	−0.05	0.40	0.999	−0.03	0.18	1.000
S1c	−0.01	0.50	0.999	−0.01	0.22	1.000
S1d	−0.04	0.45	0.999	−0.02	0.21	1.000
S2a	0.40	0.79	0.998	0.23	0.51	0.999
S2b	0.51	0.82	0.998	0.27	0.53	0.999
S2c	0.55	0.85	0.998	0.29	0.54	0.999
S2d	0.52	0.83	0.998	0.28	0.53	0.999
S3a	−0.05	0.74	0.997	0.33	0.64	0.999
S3b	−0.01	0.73	0.997	0.36	0.65	0.999
S3c	0.02	0.83	0.996	0.37	0.68	0.998
S3d	0.00	0.75	0.997	0.37	0.65	0.999
S4a	0.11	0.71	0.997	0.31	0.59	0.999
S4b	0.21	0.70	0.998	0.34	0.60	0.999
S4c	0.24	0.76	0.997	0.37	0.62	0.999
S4d	0.22	0.72	0.997	0.35	0.61	0.999

Table R3: Correlations between the cloud radiative effects and the cloud properties for the two major clusters characterized by low N_{int} values (L) and high N_{int} values (H). For the SW (LW) radiation, results are presented in case of the Spearman (Pearson) correlation.

Properties	$\mathrm{CRE_{SW,B}}$		$\mathrm{CRE_{SW,T}}$		$\mathrm{CRE_{LW,B}}$		$\mathrm{CRE_{LW,T}}$	
	L	H	L	H	L	H	L	H
Q_{L}	−0.935	−0.988	−0.930	−0.978	−0.016	−0.309	0.216	0.303
τ	−0.992	−0.994	−0.983	−0.986	0.028	−0.324	0.195	0.291
N_{int}	−0.446	−0.128	−0.410	−0.105	0.419	0.202	-0.259	−0.067
r_{int}	−0.343	−0.867	−0.353	−0.854	−0.311	−0.365	0.323	0.268
CBH	0.143	−0.213	−0.057	−0.292	−0.311	−0.239	0.752	0.786
CTH	−0.122	−0.604	−0.201	−0.663	−0.302	−0.376	0.783	0.717
H	−0.776	−0.921	−0.787	−0.925	−0.024	−0.386	0.217	0.300
f_{ad}	−0.126	−0.271	−0.129	−0.256	−0.003	0.144	0.215	0.194

Table R4: Explained variance and cumulative explained variance from different components obtained by the rotational component analysis (RC).

	RC-1	RC-2	RC-3	RC-4	RC-5	RC-6	RC-7	RC-8	RC-9
Explained variance (%)	33.8	35.5	14.8	13.6	2.10	0.10	0.10	0.00	0.00
Cumulative proportion (%)	33.8	69.3	84.1	97.7	99.8	99.9	100	100	100

Table R5: Pearson correlations between the logarithm of the cloud properties and the rotational components (RC). Degree of correlation (absolute values): (a) very weak: below 0.2, (b) weak: [0.2, 0.4), (c) moderate: [0.4, 0.6), (d) strong: [0.6, 0.8), and (e) very strong [0.8, 1.0].

Properties	RC-1	RC-2	RC-3	RC-4
CBH	0.969	0.025	−0.001	0.201
CTH	0.919	−0.282	0.076	0.237
Γ_{ad}	−0.896	−0.014	0.073	−0.183
τ	−0.062	−0.971	−0.192	−0.125
Q_{L}	0.036	−0.968	−0.240	0.052
H	0.177	−0.937	0.285	0.094
f_{ad}	−0.010	−0.099	−0.995	−0.025
N_{int}	−0.518	−0.250	−0.244	−0.778
r_{int}	0.382	−0.536	−0.314	0.681

Table R6: Input parameters for the RRTMG model.

Parameter	Value
Cosine of solar zenith angle	0.70
Carbon dioxide concentration	399 ppm
Ultraviolet/Visible surface albedo for direct radiation	0.05
Ultraviolet/Visible surface albedo for diffuse radiation	0.05
Near-infrared surface albedo for direct radiation	0.30
Near-infrared surface albedo for diffuse radiation	0.30

Table R7: Simulated scenarios. For scenarios S1–S3, three individual simulations (sub-cases) have been conducted according to different values for the droplet number concentration.

Scenarios	
Ref.	Double–moment scheme
S1	Single–moment scheme
S2	Vertical homogeneous model
S3	Sub–adiabatic model
S4	Mean vertical N_{d} profile
Sub-cases	a. 220 cm^{-3} b. N_{int} c. 480 cm^{-3}

Table R8: Mean and standard deviation of modeled CREs ($\mathrm{W\,m}^{-2}$) for the SW, LW, and NET (SW + LW) radiation for the reference simulation over all case days. ATM stands for the atmospheric cloud radiative effect defined as the difference between the CREs at the TOA and BOA.

Ref.	$\mathrm{CRE}_{\mathrm{SW}}$	$\mathrm{CRE}_{\mathrm{LW}}$	$\mathrm{CRE}_{\mathrm{NET}}$
TOA	-348.7 ± 78.39	17.51 ± 10.04	-331.2 ± 77.27
ATM	32.94 ± 12.11	-39.16 ± 13.14	-6.225 ± 12.98
BOA	-381.6 ± 86.95	56.66 ± 9.746	-324.9 ± 86.51

Table R9: Mean CRE ($\mathrm{W\,m^{-2}}$) for the SW radiation. Results are given as differences between the new scenario minus the reference simulation (Δ). The root mean square error (RMSE) in $\mathrm{W\,m^{-2}}$ and the Pearson (Pears.) correlation between the new scenarios and the reference simulation are also given.

Scen.	$\mathrm{CRE_{SW,B}}$			$\mathrm{CRE_{SW,T}}$		
	Δ	RMSE	Pears.	Δ	RMSE	Pears.
S1a	−39.2	46.4	0.960	−40.1	47.0	0.952
S1b	−7.04	11.7	0.995	−6.53	11.7	0.994
S1c	−2.59	23.4	0.964	−1.86	24.3	0.951
S2a	−26.1	39.2	0.943	−27.1	39.8	0.930
S2b	7.74	14.2	0.991	8.19	13.6	0.990
S2c	12.9	32.4	0.943	13.7	33.6	0.921
S3a	−31.1	41.4	0.950	−32.9	42.9	0.937
S3b	1.47	10.6	0.993	1.17	10.0	0.992
S3c	6.59	27.7	0.953	6.55	29.0	0.934
S4	−3.13	16.7	0.983	−3.16	17.2	0.977

Table R10: Correlations between the cloud radiative effects for the reference simulation (Ref.) and the cloud properties. For the SW (LW) radiation, results are presented in case of the Spearman (Pearson) correlation.

Properties	$\mathrm{CRE_{SW,B}}$	$\mathrm{CRE_{SW,T}}$	$\mathrm{CRE_{LW,B}}$	$\mathrm{CRE_{LW,T}}$
	Spearman		Pearson	
Q_L	−0.957	−0.955	−0.129	0.181
τ	−0.994	−0.987	0.104	0.148
N_int	−0.471	−0.431	0.428	−0.290
r_int	−0.446	−0.460	−0.395	0.344
CBH	0.148	0.063	−0.389	0.752
CTH	0.143	−0.220	−0.428	0.765
H	−0.795	−0.812	−0.200	0.226
f_ad	−0.284	−0.273	0.145	0.134

Table R11: Mean CRE ($\mathrm{W\,m^{-2}}$) for the LW radiation. Results are given as differences between the new scenario minus the reference simulation (Δ). The root mean square error (RMSE) in $\mathrm{W\,m^{-2}}$ and the Pearson (Pears.) correlation between the new scenarios and the reference simulation are also given.

Scen.	$\mathrm{CRE_{LW,B}}$			$\mathrm{CRE_{LW,T}}$		
	Δ	RMSE	Pears.	Δ	RMSE	Pears.
S1a	−0.11	0.48	0.999	−0.04	0.19	1.000
S1b	−0.05	0.40	0.999	−0.03	0.18	1.000
S1c	−0.01	0.50	0.999	−0.01	0.22	1.000
S2a	0.40	0.79	0.998	0.23	0.51	0.999
S2b	0.51	0.82	0.998	0.27	0.53	0.999
S2c	0.55	0.85	0.998	0.29	0.54	0.999
S3a	−0.05	0.74	0.997	0.33	0.64	0.999
S3b	−0.01	0.73	0.997	0.36	0.65	0.999
S3c	0.02	0.83	0.996	0.37	0.68	0.998
S4	−0.02	0.49	0.999	−0.02	0.22	1.000

References

[1] R. Heinze, A. Dipankar, C. C. Henken, C. Moseley, O. Sourdeval, S. Trömel, X. Xie, P. Adamidis, F. Ament, H. Baars, C. Barthlott, A. Behrendt, U. Blahak, S. Bley, S. Brdar, M. Brueck, S. Crewell, H. Deneke, P. Di Girolamo, R. Evaristo, J. Fischer, C. Frank, P. Friederichs, T. Göcke, K. Gorges, L. Hande, M. Hanke, A. Hansen, H.-C. Hege, C. Hoose, T. Jahns, N. Kalthoff, D. Klocke, S. Kneifel, P. Knippertz, A. Kuhn, T. van Laar, A. Macke, V. Maurer, B. Mayer, C. I. Meyer, S. K. Muppa, R. A. J. Neggers, E. Orlandi, F. Pantillon, B. Pospichal, N. Röber, L. Scheck, A. Seifert, P. Seifert, F. Senf, P. Siligam, C. Simmer, S. Steinke, B. Stevens, K. Wapler, M. Weniger, V. Wulfmeyer, G. Zängl, D. Zhang, and J. Quaas, "Large-eddy simulations over germany using icon: a comprehensive evaluation," *Q. J. R. Meteorol. Soc.*, vol. 143, no. 702, pp. 69–100, 2017.

[2] A. Gassmann and H.-J. Herzog, "Towards a consistent numerical compressible non-hydrostatic model using generalized hamiltonian tools," *Q. J. Roy. Meteor. Soc.*, vol. 134, no. 635, pp. 1597–1613, 2008.

[3] A. Dipankar, B. Stevens, R. Heinze, C. Moseley, G. Zängl, M. Giorgetta, and S. Brdar, "Large eddy simulation using the general circulation model icon," *J. Adv. Model. Earth Syst.*, vol. 7, no. 3, pp. 963–986, 2015.

[4] H. Wan, M. A. Giorgetta, G. Zängl, M. Restelli, D. Majewski, L. Bonaventura, K. Fröhlich, D. Reinert, P. Rípodas, L. Kornblueh, and J. Förstner, "The icon-1.2 hydrostatic atmospheric dynamical core on triangular grids – part 1: Formulation and performance of the baseline version," *Geosci. Model Dev.*, vol. 6, no. 3, pp. 735–763, 2013.

[5] A. Seifert and K. D. Beheng, "A two-moment cloud microphysics parameterization for mixed-phase clouds. part 1: Model description," *Meteorol. Atmos. Phys.*, vol. 92, no. 1, pp. 45–66, 2006.

[6] L. B. Hande, C. Engler, C. Hoose, and I. Tegen, "Parameterizing cloud condensation nuclei concentrations during hope," *Atmos. Chem. Phys.*, vol. 16, no. 18, pp. 12059–12079, 2016.

[7] A. Macke, P. Seifert, H. Baars, C. Barthlott, C. Beekmans, A. Behrendt, B. Bohn, M. Brueck, J. Bühl, S. Crewell, T. Damian, H. Deneke, S. Düsing, A. Foth, P. Di Girolamo, E. Hammann, R. Heinze, A. Hirsikko, J. Kalisch, N. Kalthoff, S. Kinne, M. Kohler, U. Löhnert, B. L. Madhavan, V. Maurer, S. K. Muppa, J. Schween, I. Serikov, H. Siebert, C. Simmer, F. Späth, S. Steinke, K. Träumner, S. Trömel, B. Wehner, A. Wieser, V. Wulfmeyer, and X. Xie, "The hd(cp)^2 observational prototype experiment (hope) – an overview," *Atmos. Chem. Phys.*, vol. 17, no. 7, pp. 4887–4914, 2017.

[8] M. Lebsock and H. Su, "Application of active spaceborne remote sensing for understanding biases between passive cloud water path retrievals," *J. Geophys. Res.-Atmos.*, vol. 119, no. 14, pp. 8962–8979, 2014.

[9] R. Wood and D. L. Hartmann, "Spatial variability of liquid water path in marine low cloud: The importance of mesoscale cellular convection," *J. Climate*, vol. 19, no. 9, pp. 1748–1764, 2006.

[10] R. Wood, "Relationships between optical depth, liquid water path, droplet concentration, and effective radius in adiabatic layer cloud," *University of Washington*, vol. 3, 2006.

[11] J. Quaas, O. Boucher, and U. Lohmann, "Constraining the total aerosol indirect effect in the lmdz and echam4 gcms using modis satellite data," *Atmos. Chem. Phys.*, vol. 6, no. 4, pp. 947–955, 2006.

[12] D. P. Grosvenor, O. Sourdeval, P. Zuidema, A. Ackerman, M. D. Alexandrov, R. Bennartz, R. Boers, B. Cairns, J. C. Chiu, M. Christensen, H. Deneke, M. Diamond, G. Feingold, A. Fridlind, A. Hünerbein, C. Knist, P. Kollias, A. Marshak, D. McCoy, D. Merk, D. Painemal, J. Rausch, D. Rosenfeld, H. Russchenberg, P. Seifert, K. Sinclair, P. Stier, B. van Diedenhoven, M. Wendisch, F. Werner, R. Wood, Z. Zhang, and J. Quaas, "Remote sensing of droplet number concentration in warm clouds: A review of the current state of knowledge and perspectives," *Rev. Geophys.*, vol. 56, no. 2, pp. 409–453, 2018.

Answers to Anonymous Referee #2

We thank the anonymous referee #2 for his/her constructive comments and suggestions that certainly have improved the manuscript significantly. We revised the manuscript according to his/her comments and the comments of anonymous referees #1 and #3. In the following,

- *referee's comments are given in italic*,
- our answers are outlined in normal format, and
- **textual changes in the manuscript are given in bold format**.

General changes

We would like inform the anonymous referee #2 about the following changes:

1. Driven by the specific comment (SC) #18 of anonymous referee #3 (SC3.18), we decided to drop scenario S4 from the analysis. The difference between the sub-adiabatic model (S3) and the modified one (S4) is that the latter accounts for the depletion of the liquid water content due to entrainment, precipitation, and freezing drops. Consequently, we wanted to check whether S4 captures better the vertical stratification of the modeled low-level clouds and, accordingly, if it approximates the CREs of the reference simulation with better accuracy. Since S4 does not provide any further insight, we now have decided to drop this scenario. However, we do confirm that, by considering all the case days in the analysis, we came to the same conclusions as for 3 June. As a confirmation, we updated the Tables and attached them at the end of this document. The referee is referred to Tables R1–R3.

2. In all scenarios, we decided to drop sub-case d, which employs two fixed values for the droplet number concentration representing the two modes in the corresponding histogram for 3 June 2016. This scenario separates clouds into a cluster with low/high clouds. Considering the vertical variability of the droplet number concentration, the latter clustering will link low clouds (within the boundary layer) with high N_{d} and, accordingly, high clouds with lower N_{d} values. Thus, for all scenarios, employing such values for N_{d} are able to approximate the reference radiative transfer simulation very well. Only the radiative transfer simulation that is supplied by the droplet number concentration weighted over the cloud geometrical extent, i.e., N_{int} (sub-case b) leads to smaller differences when compared to the reference simulation. However, we do confirm that, by considering all the case days into the analysis, we came to the same conclusions as for 3 June. Note that, for the latter case, the clustering was conducted on the mean N_{int} over all case days. As a confirmation, we updated the Tables and attached them at the end of this document. The referee is referred to Tables R1–R3.

3. We decided to add a new scenario as a replacement of sub-case d, whereby radiative transfer simulations are conducted for a mean vertical profile of the droplet number concentration over all case days. Tables R9–R11 summarize the new results. In brief, this scenario is considered as an improvement compared to the clustering case. The following parts were included within the text:

Section 5.1.2: **Last but not least, by replacing the vertical profile of N_d by the mean profile of N_d over all case days (see Fig. 2), emulates the cloud radiative effects of the reference simulation quite well. Accordinly, scenario S4 slightly undersimates the mean SW CREs, with an mean error up to $-3.16\,\mathrm{W\,m^{-2}}$ and a RMSE up to $17.2\,\mathrm{W\,m^{-2}}$ for both BOA and TOA. In fact, this scenario outperforms the rest scenarios (S1–S3), except from the sub-case b (N_int) in all scenarios. For an illustration of the excellent linear correlation between the reference simulation and S4 by means of a bivariate kernel density (BKD) plot, the reader is referred to Fig. B1 in Appendix B. One can see that the CREs computed by these scenarios are in a very good agreement almost everywhere except towards larger values of the CREs in case of the SW radiation, with Pearson correlations larger than 0.977 for both BOA and TOA.**

Section 6: **By employing a more representative profile for the N_d, i.e., a mean vertical profile of N_d over all case days leads to a rather good approximation; the RMSE is below $17.2\,\mathrm{W\,m^{-2}}$. This points to the need to better account for prognostic N_d calculations.**

Appendix B: **In sect. 5.1.2, by conducting idealized radiative transfer simulations, we estimated the impact of the representation of cloud properties in ICON-LEM on the cloud radiative effects (CREs). Special emphasis was given on identifying the droplet number concentration (N_d), which approximates the microphysical and radiative properties of low-level clouds as simulated by ICON-LEM (reference scenario). A radiative transfer simulation, which employs a mean vertical profile of N_d over all the case days (scenario S4), approximates the CREs of the reference scenario quite well. Figure B1 depicts the excellent linear correlation between the reference simulation and S4 by means of a bivariate kernel density (BKD)**.

4. Following the general comment of anonymous referee #2 for shortening the manuscript given the redundancy of many of the results shown in this study and his/her relevant specific comments (SC), i.e., (SC2.12) and (SC2.25):

   - We decided to drop Fig. B1. Figure B1 illustrates the bivariate kernel density (BKD) between the cloud optical thickness and the liquid water path on a logarithmic scale. Considering the comprehensive explanation given in Sect. 3.3.1, we decided that this illustration did not provide any additional information.
   - Figures 6 and 7 have been revised. Now, they illustrate results only for TOA (see Figs R2 and R3).
   - We now focus only on the rotational component analysis. The mention of the principal component analysis have been significantly reduced. In addition, we removed the relevant information from Table 3. For the updated version of the Table, the referees are referred to Table R5. Additionally, we replaced Figure 5 by Table R4. This table lists the contribution of each rotational component to the total variance.

Answers to general comments (GC) from referee #2 (GC2)

(GC2.1) *There is already a significant body of work on the topic of sub-adiabaticity (much of which the authors cite) and the results of this study seem to confirm past findings (in particular, those of Merk et al., 2016) with little added insight into process (radiative, microphysical, etc.) besides pointing out that single-moment microphysics schemes leave much to be desired (which has been explored by e.g., Igel et al., 2015, JAS). Much work has also been done with respect to statistical emulators for understanding cloud radiative effects (e.g. Feingold et al., 2016; Glassmeier et al., 2019) and the aggregation of model data over all shallow cloudy columns severely limited the authors' ability to examine details regarding differences between cumulus and stratus (which likely exhibit very different fad), the diurnal cycle, or radiative effects across spatial scales – an exploration of the latter would be especially useful since the 300 m HOPE dataset is finer in horizontal resolution than the existing remote sensing products this study is designed to improve (typically 1 km pixel size).*

We acknowledge Referee's #2 concerns with respect to the novelty of this study. However, we respectfully disagree on this point. ICON-LEM domain consists of 150 vertical levels, with resolutions ranging from 25 m to 70 m within the boundary layer, from 70 m to 100 m further up to the altitude limit for the occurrence of low-level clouds selected for this study (4000 m), and from 70 m to 355 m further up until the top of the model domain at 21 km. This unprecedented high vertical resolution enables a significantly improved investigation of the vertical distribution of microphysical properties of low-level clouds as simulated by a double-moment scheme. We do agree that the vertical structure of adiabaticity depends on cloud regimes, types, and life-stage and, thus, it could be an interesting extension. However, due to the high horizontal resolution of ICON-LEM, for a single day, the number of "independent" cloudy columns are very large and complicates the investigation of such dependencies. Note here that the model output employed in this study, 3D HOPE data, has an output frequency of 15 min, while the domain size is limited to 45 km^2. For such studies, especially when it comes to life-stage, it would be better to use model data with higher output frequency, e.g., 1D profiles that are available every 10 sec. But, this is beyond the purpose of this study.

However, we revised our manuscript according to the comments of anonymous referees #1 and #3 and further extended our analysis to consider all case days to improve the robustness of our results. Now, sections 3.2 and 5 outline our findings for all case days.

(GC2.2) *Finally, I get the sense that this paper only deals with sub-adiabaticity in passing – the latter half of the paper is primarily concerned with describing CREs with a minimal set of variables and is almost completely disconnected from the title of the paper. Sub-adiabaticity seems to have only a weak influence on CREs.*

A high-resolution model as ICON-LEM is an ideal tool to investigate the suitability of the sub-adiabatic cloud model, firstly, for the evaluation of the representation of low-level clouds and, secondly, to capture the relevant properties which determine the cloud radiative effect. This outlines our main objectives and we think that it is reflected by the title of the paper.

We do not completely agree that the sub-adiabatic fraction has only a weak influence on the cloud radiative effect (CRE). In the first place, the sub-adiabatic fraction is the key component for

deriving the cloud optical thickness that is one of the fundamental cloud properties for describing the shortwave (SW) cloud radiative effects (CREs). Based on six case days, we found that the behavior of modeled liquid water clouds over Germany more closely resembles the sub-adiabatic model than the vertically homogeneous one, with a mean sub-adiabatic fraction (f_{ad}) of about 0.45. This model suggests, e.g., scaling of $\log(\tau)/\log(Q_{\mathrm{L}})$ with 5/6 and $f_{\mathrm{ad}} < 1$. This scaling behavior has implications to, at least, the shortwave (SW) CRE. In addition, Eq. (15) contains the factor $\tau \propto f_{\mathrm{ad}}^{-1/6}$. The latter factor, in combination with the mean sub-adiabatic fraction found in this study has a significant impact in τ compared to the pure adiabatic assumption that is usually employed.

Last but not least, the rotational component analysis (principal component and varimax rotation), clearly identifies the sub-adiabatic fraction as one of the minimal set of parameters to explain the CREs. In fact, it shows up as the 3$^{\mathrm{rd}}$ rotational component (RC-3) that explains 14.8 % of the total variance.

(GC2.3) *With respect to motivation, the authors rely heavily and repeatedly on the idea that there are large uncertainties in aircraft measurements of cloud drop number concentration (N_{d} in the authors' notation), which they justify by citing the N_{d} retrieval review paper of Grosvenor et al. (2018) – specifically, I believe they refer to Grosvenor et al.'s Figure 5 (which is in turn based on data used in Siebert et al., 2013) and accompanying discussion. This is an unfortunate figure. The disagreement of two probes (Phase Doppler Interferometer and Particulate Volume Monitor; PDI and PVM, respectively) at concentrations of $N_{\mathrm{d}} > 350\,cm^{-3}$ is used as evidence that in situ probes have a general, systematic problem measuring N_{d}.*

The issue with this illustration is that one of the two probes used (PVM) is not designed to measure N_{d} and I am aware of no other publication in which this is even attempted. The PVM measures extinction from a population of cloud drops and makes no explicit count of particle density. In fact, I'm not even sure how this quantity was generated since the PVM returns only two data streams: total particle volume and surface area. The PDI, on the other hand, is frequently used by both the airborne cloud physics and industrial spray characterization communities and has been demonstrated to accurately count (and size) particles up to a concentration of O(105) cm-3. An intercomparison of PDI with other probes that explicitly count particles (CAS, FSSP, CDP, Holodec... etc. – there are a great number and I don't understand why Grosvenor et al. chose such an ill-suited probe for their figure) would likely show a much better overlap in the PDFs of N_{d} from different probes; such an intercomparison of the latest generation of cloud probes is currently underway for the recent NASA ORACLES campaign, which sampled a wide variety of concentration conditions due to the campaign's focus on interaction of clouds with overlying smoke layers during the stratocumulus to cumulus transition.

I am strongly opposed to the use of phrasing such as "large instrumental uncertainties" (e.g. page 23, lines 10-11) as I think this point is vastly overstated by Grosvenor et al. (2018), an assertion backed by their discussion of myriad other issues with retrieval assumptions ahead of any problems with in situ measurements.

We thank the anonymous referee #2 for the insight given. We revised this part of the text as follows:

The vertical variability of the droplet number concentration was examined. **For all the case days**, above an altitude of **about** 2 km, values of N_d are about 200 cm^{-3} and are, thus, close to climatological values, while in the boundary layer, the double moment scheme predicts N_d values above 600 cm^{-3}. Such values are **regarded as** rather high compared to satellite remote sensing estimates [1, 2], **but such comparison is rather vague considering, firstly, the large uncertainties of the satellite-derived estimates of cloud droplet number concentration [2] and, secondly, they are not available in high resolution. However,** in situ observations, **which are considered to be the most accurate approach to determine** N_d**,** suggest higher values and, hence, lie closer to those simulated by ICON-LEM. **Thus, by means of in situ observations, evaluation activities should be conducted for a better characterization of the droplet number concentration from remote sensing techniques. The latter will scrutinize the double-moment scheme implemented in ICON-LEM and could potentially lead to better simulations of cloud processes and radiation.**

We additionally revised the corresponding text in Section 3.2 as follows,

On the contrary, in situ observations suggest higher values of N_d and, accordingly, closer to those simulated by ICON-LEM. **Hence, efforts should be undertaken to further validate the cloud droplet number concentrations predicted by the double-moment scheme.**

Answers to specific comments (SC) from referee #2 (SC2)

(SC2.1) *P2, L7: "taking placed" should be "taking place"*

The text is corrected.

(SC2.2) *P2, L21-22: "fixed droplet number distribution" – ambiguous terminology; "fixed droplet size distribution" would be clearer.*

The text is revised.

(SC2.3) *P2, L23: "Double-moment microphysical schemes... are only recently becoming more widespread": Perhaps in the operational forecasting community this is true, but in research modeling (especially of warm clouds), double-moment schemes have been common for at least a decade.*

The referee is correct. We revised the text by adding at the end of the sentence: **in operational forecasting**.

(SC2.4) *P5, L16: Why do you use an indirect measure for rain/drizzle instead of directly examining rain water mixing ratio? I understand that it makes for a more straightforward comparison with observations, but it seems like an unnecessary step.*

The referee is correct. The reasoning was to perform a straightforward link to observations. However, we do consider the rain water content as an additional threshold. Relevant information

has been included.

(SC2.5) *P6, L2: "The model outputs the..."*

The text is revised.

(SC2.6) *Is the assumption of vertical homogeneity a "scheme?" Seems like an odd word choice.*

The text is revised accordingly and the word "scheme" is replaced by "model".

(SC2.7) *P7, L15: "Clapeyron relationship"*

The word "relationship" has been included.

(SC2.8) *P7, L16-17: This sentence is difficult to follow. Rephrase and simplify the structure for clarity.*

The text is revised as follows: **For low level clouds, Γ_{ad} varies slightly (∼20%). Consequently, in most studies, Γ_{ad} is assumed constant (e.g., Albrecht et al., 1990; Boers et al., 2006) or it is calculated from cloud bottom temperature and pressure (e.g., Merk et al., 2016) or cloud top information (e.g., Zeng et al., 2014).**

(SC2.9) *P11, L8: Remove "the" from "the 5 May..."*

The text is corrected.

(SC2.10) *P13, L12-13: "with a 5/6 slope" – possibly remove the word "fit," doesn't make sense in context.*

The text is revised accordingly.

(SC2.11) *P13, L18: If f_{ad} only accounts for 0.14% of the variance in τ, what's the point of all this?*

Actually, in Sect. 3.3.1, we try to predict the cloud optical thickness derived from the output of ICON-LEM (by using Eq. 14), via employing the relevant equation suggested by the sub-adiabatic model, i.e., Eq. (15). Note here that, based on 6 case days, f_{ad} is 0.45 on average and not 1. For further information with respect to the relative importance of the sub-adiabatic fraction, the referee is referred to our answer at (GC2.2). This section has been revised:

Correction: f_{ad} accounts for 0.2 % of the variance in τ.

With this intention, an effort has been conducted to predict the cloud optical thickness derived from Eq. (14) by employing the sub-adiabatic model and Eq. (15).

In fact, model $Y_4(Q_{\mathrm{L}}, f_{\mathrm{ad}}, N_{\mathrm{int}})$ supports the applicability of the sub-adiabatic model since it is able to approximate the cloud optical thickness with high accuracy (RMSE =

0.027)

(SC2.12) *P13, Section 4: The step by step narrative of the PC analysis is overwrought. If you primarily intend to use the results of the RC analysis to justify the minimal set of variables needed to represent CREs, skip the PC discussion; the PC and RC results are sufficiently similar that it is redundant.*

We understand the referee's concerns, but we do not entirely agree that PC and RC results are sufficiently similar. Although each PC is clearly dominated by some properties, they are found moderately or strongly correlated with the remaining properties. On the contrary, the rotational component analysis points to exactly which properties dominate at each RC. However, we do agree that we provided a comprehensive analysis and, hence, we decided to revise and shorten the text. We now focus only on the rotational component analysis. The mention of the principal component analysis have been significantly reduced. In addition, we removed the relevant information from Table 3. For the updated version of the Table, the referee is referred to Table R5. Additionally, we replaced Figure 5 by Table R4. This table lists the contribution of each rotational component to the total variance.

(SC2.13) *P13, L34: "optimal" instead of "optimized"*

The text is corrected.

(SC2.14) *P14, Table 3 caption: Remove trailing zero from "moderate [0.40, 0.6)" for consistency*

The text is revised accordingly.

(SC2.15) *P14, L7-9: Rearrange sentence beginning "However, the PCs..." to simplify structure for clarity.*

The text is revised: However, the PCs are hard to interpret**. Although each new dimension is clearly dominated by some of the cloud properties, the PCs are found moderately or strongly correlated with other properties.**

(SC2.16) *P14, L11: remove "so-called" – this makes it look like other people have a different name for it.*

The word "so-called" has been removed.

(SC2.17) *P15, L9-10: I am confused by what you're doing here – are you always running multiple simulations, or for scenarios S2-S4 are you imposing LWC/ND profiles that are not actually from the simulations?*

We only conduct radiative transfer simulations. For the reference scenario, the input for the RRTMG was constructed on the basis of ICON-LEM. In other words, temperature, pressure, and water vapour profiles, surface temperature and pressure, and cloud liquid water content and droplet number concentration. In the rest scenarios (S1-S4), we preserve the liquid water content and the k_2 parameter (taken from ICON-LEM) and we vary only the droplet number concentration. In

addition, for scenarios S2-S4, the liquid water path for each profile is re-distributed over the vertical. In this way, we can estimate the effects of the bulk microphysical parameterizations and the vertical stratification of the cloud properties on the CREs. (The relevant information is found in sections 5.1 and 5.1.1).

(SC2.18) *P15-16, L33-3: the assumptions would be more clearly expressed in a table.*

A table listing the details of all the assumptions has been added according the referee's suggestion (see Table R6).

(SC2.19) *P16, L1-2: Why are there drops in the free troposphere?.*

It is true that aerosols and their precursor gases are mostly produced in the boundary layer. However, they can be transported into the free troposphere via different mechanisms, such as trough convection and frontal uplift. There, their lifetime is much longer due to less efficient dry deposition as compared to the boundary layer and, accordingly, they can facilitate long-distance transport [3]. For example, Kupiszewski et al., (2013), reported that plumes in air aloft, above the boundary layer, can be attributed to transport of polluted air, e.g., via biomass burning. Biomass burning produces heat and moisture and this further leads to buoyancy-forced vertical and horizontal circulations of air and advection of hot gases [4]. The latter process is the main reason for the rapid uplift of smoke particles that are known to be an efficient CCN. Over the last decades, several studies reported aerosols in the free troposphere [5, 6] and even investigated CCN production there [7, 8, 9].

(SC2.20) *P16, L3: "where the liquid water path is preserved"*

The sentence is rearranged to be more clear: **Two different scenarios are considered, where the liquid water path is preserved within the vertical column, but the water content profile is redistributed.**

(SC2.21) *P16, L8: "following the climatology of a coarse..." – you only use the ECHAM value. Is this representative of what all GCMs do? If not, the generalization doesn't work.*

The same droplet number concentration profile is adopted by the regional climate model REMO [10]. A similar climatology is employed by ICON-NWP, which is the global Numerical Weather Prediction (NWP) version of ICON model heinze2017. The only difference in ICON-NWP is that the droplet number concentration within the boundary layer is $200\,\mathrm{cm}^{-3}$ and not $220\,\mathrm{cm}^{-3}$ as in ECHAM and REMO. An example study, whereby the climatology of N_d implemented in ECHAM was compared to satellite retrieved N_d, is the one by Quaas et al., (2006). They retrieved N_d from MODIS and showed slightly lower values as compared to ECHAM N_d values, but consistent land-sea contrast [1].

The following part has been included in Section 3.1:

Note here that this value is close to the fixed droplet number concentration profile suggested by single-moment microphysical schemes adopted by atmospheric **models, such as ECHAM [11] and ICON-NWP, which is the global Numerical Weather Prediction (NWP) ver-**

sion of the ICON model [12].

(SC2.22) *P17, Section 5.1.2: I found the latter half of this discussion to be very difficult to follow, especially the references to various scenarios by only a letter or number near the end of the section (i.e. last paragraph, P18).*

We feel sorry for any inconvenience caused. The text has been revised.

(SC2.23) *P18, Table 5 caption: Cosine SZA was just given in text (and will hopefully be put in a separate table of assumptions) – remove since redundant.*

A table listing the details of all the assumptions has been added according the referee's suggestion (see R6). Thus, we removed the aforementioned information from the caption of Table 5.

(SC2.24) *P18, L1: "and the rest of the simulated. . . "*

The text is revised accordingly.

(SC2.25) *P19, Table 6: Two things: 1) numbering of scenarios is off by one and 2) since BOA and TOA are almost always within 5% or 1 W/m2 of each other, can you just pick one and reduce the amount of information here? This table would be much more effective/digestible.*

We thank the referee for highlighting the mistake in the numbering. We decided to keep the results for both BOA and TOA. However, we now have reduced the amount of scenarios employed in this study, hopefully making the table and the analysis easier to follow. In brief, we dropped scenario S4 (the modified sub-adiabatic mode), the sub-scenario (d, clusters), and included a new scenario representing the mean droplet number concentration profile over all case days. For a comprehensive description of all the changes made, the referee is referred to section **General changes** of the current document.

(SC2.26) *P19, L11-14: You can test whether effective radius is outside the range. Is this an issue or isn't it?*

For all the scenarios, we inter-compared only columns with valid values for the effective radius. Thus, we revised the text as follows:

Note here that the RRTMG model is able to derive the radiative fluxes only for effective radius between $2.5\,\mu$m and $60\,\mu$m. **For all scenarios, all columns with effective radius outside this range have been excluded.**

(SC2.27) *P20, Section 5.1.3: As with the PCA results, what is the point of showing both correlations? You almost exclusively discuss Spearman, so why not just show that?*

We understand the referee's concerns with respect to the use of both Spearman and Pearson correlations. The principal component analysis reveals systematic co-variations among the cloud properties. These components can be seen as a linear combination among the original properties and, hence, we employ the Pearson correlation to describe their relation. However, in Section

5.1.3, we describe the correlation between the cloud radiative effects and the cloud properties and the rotational components. In case of the SW radiation, Spearman correlation is the ideal metric to describe the monotonic relation between the CREs and the cloud optical thickness, liquid water path, and cloud geometrical extent (and, accordingly, RC-2). On the other hand, in the LW radiation, due to the linear relationship between the CREs and the cloud bottom and top heights (and, accordingly, RC-1), the right metric to describe their relation is the Pearson correlation. We decided to keep both correlations, but revised the text so that we highlight their importance.

(SC2.28) *P20, L7: Capitalize "Spearman"*

Corrected.

(SC2.29) *P24, L3: "uncover potential shortcomings in... models": you only compared the model to itself, so how did you uncover shortcomings? Do you mean LES vs. GCM? Beyond discussing single- vs. double-moment microphysics (an already well-known issue), what shortcomings did you uncover?*

That was a mistake. We revised the text as follows: **The goal was ultimately to uncover potential shortcoming in the representation of clouds towards the computation of the cloud radiative effects.**

(SC2.30) *P24, L11: quantify contributions of 3rd/4th components to total variance here.*

We thank the referee for highlighting that we omitted an explicit reference to the contribution of the 3rd and 4th components to the total variance. These two components are clearly a function of the sub-adiabatic factor and the droplet number concentration (P20, L19), respectively, pointing to two clear degrees of freedom. They account for 14.8 % and 13.6 %, respectively, outlining their importance in identifying the minimum set of parameters for the representation of low-level clouds towards the computation of the CREs. Accordingly, we included the missing information. In addition, we decided to replace Figure 5 by a Table, where we list the contribution of each rotational component to the total variance.

(SC2.31) *P24, L11: delete "so-called"*

The word "so-called" has been removed.

(SC2.32) *P25, L9: again, is the ECHAM climatological ND representative? Is it even backed by observations? You have not made a case for why this is a good number to use, besides the fact that a single GCM uses it.*

we addressed the latter issue in (SC.21).

(SC2.33) *P25, L10: How do two fixed values constitute a profile?*

The referee is correct. The use of the word "profile" for a constant droplet number concentration over the vertical can be misleading. We have removed the profile and replace it by the word "values" throughout the manuscript.

(SC2.34) *P27, Eq A13: is exponent in denominator a typo? D^0=1.*

Indeed there was a typo. The denominator is actually the zeroth moment of the droplet size distribution, which corresponds to the droplet number concentration. The text has been revised.

List of Figures

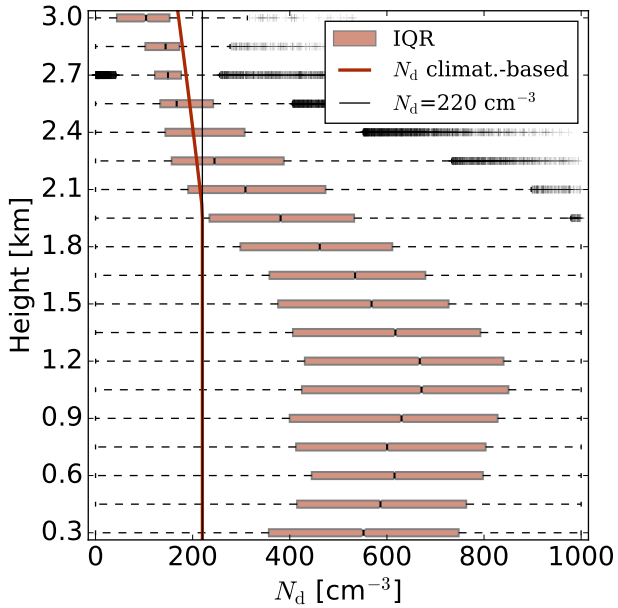

Figure R1: Box-whisker plot of the droplet number concentration for all the case days on average, describing the histograms of N_d simulated for different model levels by the double moment scheme of ICON-LEM. Boxes illustrate interquartile range (IQR), dark red line denotes the climatology-based N_d profile adopted by ECHAM, and the thin black line demonstrates the constant N_d profile of 220 cm^{-3}.

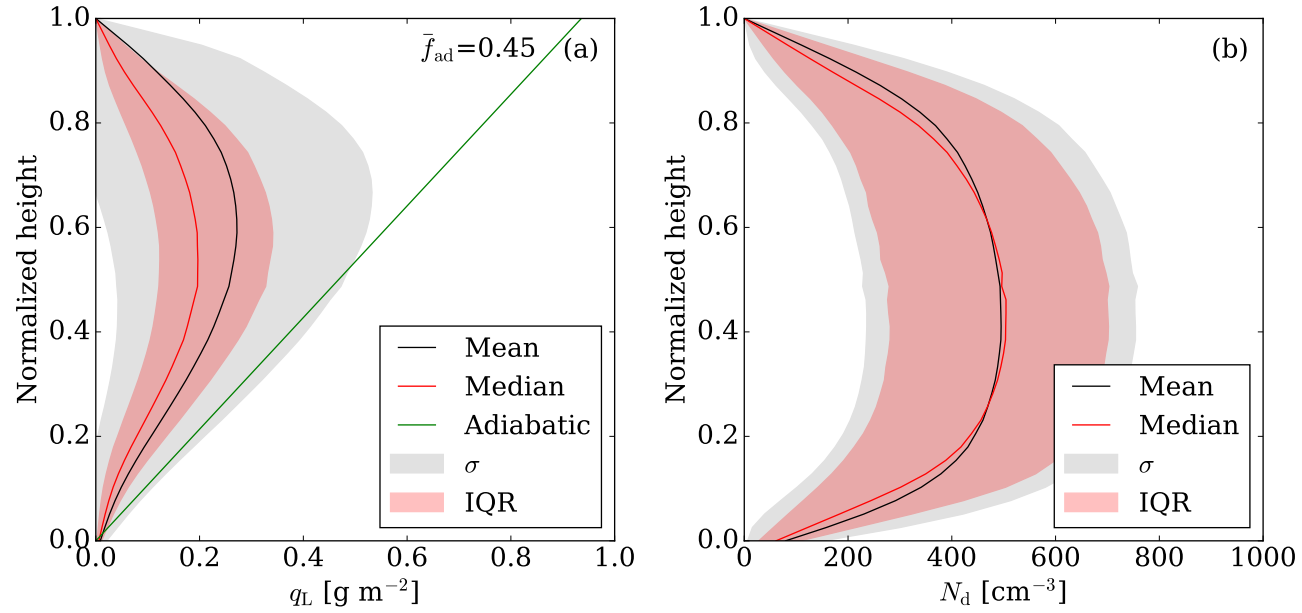

Figure R2: ICON-LEM simulated mean (a) q_L and (b) N_d profiles for all the case days on average. Profiles are normalized over height from the CBH to the CTH. Black lines denote the mean, red solid lines the median, gray shaded areas the standard deviation, red shaded areas the interquartile range (IQR), and the green solid line outline the mean adiabatic q_L profile characterized by a mean adiabatic fraction ($\bar{f}_{ad}$) of 0.45.

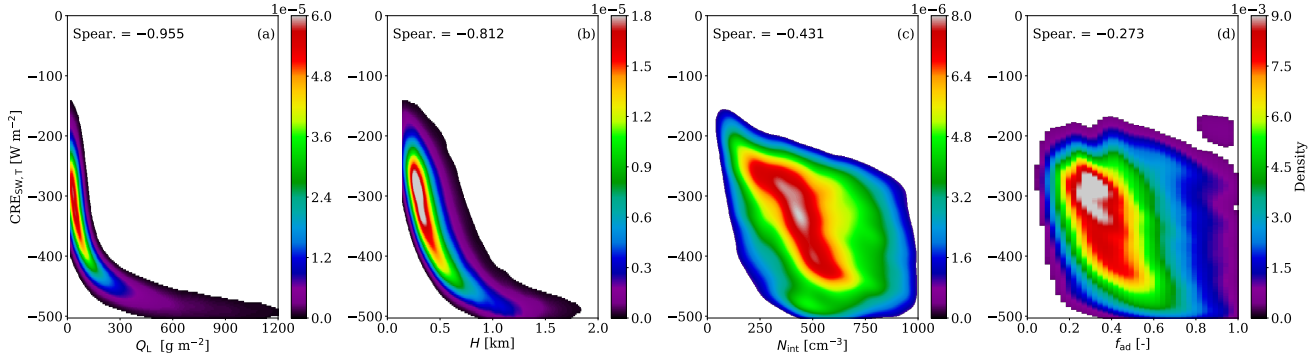

Figure R3: Bivariate kernel density (BKD) between the reference simulation (Ref.) and the cloud properties that are essential for the derivation of the cloud optical thickness that is one of the fundamental properties describing the SW cloud radiative effect. Panels illustrate the BKD between the $CRE_{SW,T}$ and (a) Q_L, (b) H, (c) N_{int}, and (d) f_{ad}. The corresponding Spearman (Spear.) correlations are highlighted.

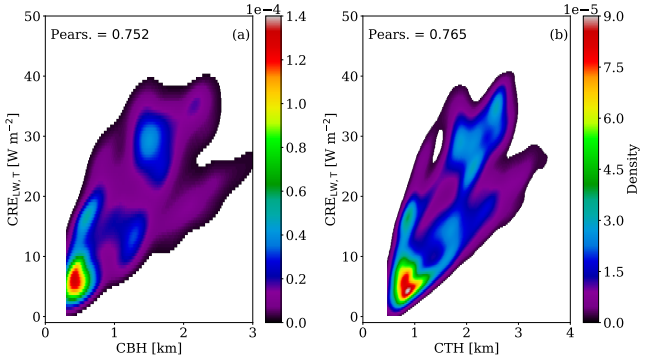

Figure R4: Bivariate kernel density (BKD) between the reference simulation (Ref.) and the cloud properties describing the LW cloud radiative effect at the TOA and (a) CBH and (b) CTH. The corresponding Pearson (Pears.) correlations are highlighted.

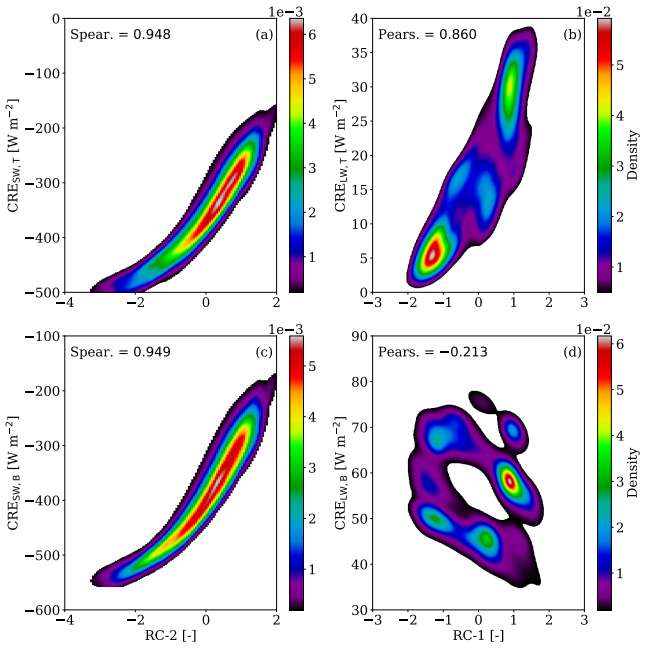

Figure R5: For the reference simulation (Ref.), bivariate kernel density (BKD) between CRE_{SW} and the second rotational component (RC-2) at (a) TOA, (c) BOA and between CRE_{LW} and the first rotational component (RC-1) at (b) TOA, (d) BOA. The corresponding Spearman (Spear.) and Pearson (Pears.) correlations are highlighted for the SW and LW radiation, respectively.

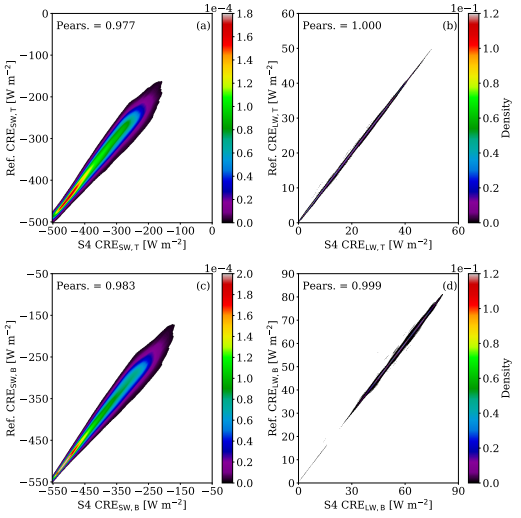

Figure R6: Bivariate kernel density (BKD) between the reference simulation (Ref.) and the scenario that employs the mean vertical N_{d} profile (S4). For the CREs, BKD are presented for the SW radiation at the TOA (a) and BOA (c), and for the LW radiation at the TOA (b) and BOA (d). The corresponding Pearson (Pears.) correlations are highlighted.

List of Tables

Table R1: Mean CRE ($\mathrm{W\,m^{-2}}$) for the SW radiation. Results are given as differences between the new scenario minus the reference simulation (Δ). The root mean square error (RMSE) in $\mathrm{W\,m^{-2}}$ and the Pearson (Pears.) correlation between the new scenarios and the reference simulation are also given.

Scen.	$\mathrm{CRE_{SW,B}}$			$\mathrm{CRE_{SW,T}}$		
	Δ	RMSE	Pears.	Δ	RMSE	Pears.
S1a	−39.2	46.4	0.960	−40.1	47.0	0.952
S1b	−7.04	11.7	0.995	−6.53	11.7	0.994
S1c	−2.59	23.4	0.964	−1.86	24.3	0.951
S1d	−6.57	17.6	0.982	−5.99	18.0	0.977
S2a	−26.1	39.2	0.943	−27.1	39.8	0.930
S2b	7.74	14.2	0.991	8.19	13.6	0.990
S2c	12.9	32.4	0.943	13.7	33.6	0.921
S2d	8.53	22.6	0.971	9.10	22.9	0.964
S3a	−31.1	41.4	0.950	−32.9	42.9	0.937
S3b	1.47	10.6	0.993	1.17	10.0	0.992
S3c	6.59	27.7	0.953	6.55	29.0	0.934
S3d	2.29	19.1	0.976	2.09	19.5	0.969
S4a	−28.7	40.1	0.947	−30.3	41.4	0.934
S4b	4.97	11.7	0.993	4.80	11.1	0.992
S4c	10.1	29.9	0.949	10.2	31.2	0.928
S4d	5.72	20.4	0.975	5.67	20.8	0.967

Table R2: Mean CRE ($\mathrm{W\,m^{-2}}$) for the LW radiation. Results are given as differences between the new scenario minus the reference simulation (Δ). The root mean square error (RMSE) in $\mathrm{W\,m^{-2}}$ and the Pearson (Pears.) correlation between the new scenarios and the reference simulation are also given.

Scen.	$\mathrm{CRE_{LW,B}}$			$\mathrm{CRE_{LW,T}}$		
	Δ	RMSE	Pears.	Δ	RMSE	Pears.
S1a	−0.11	0.48	0.999	−0.04	0.19	1.000
S1b	−0.05	0.40	0.999	−0.03	0.18	1.000
S1c	−0.01	0.50	0.999	−0.01	0.22	1.000
S1d	−0.04	0.45	0.999	−0.02	0.21	1.000
S2a	0.40	0.79	0.998	0.23	0.51	0.999
S2b	0.51	0.82	0.998	0.27	0.53	0.999
S2c	0.55	0.85	0.998	0.29	0.54	0.999
S2d	0.52	0.83	0.998	0.28	0.53	0.999
S3a	−0.05	0.74	0.997	0.33	0.64	0.999
S3b	−0.01	0.73	0.997	0.36	0.65	0.999
S3c	0.02	0.83	0.996	0.37	0.68	0.998
S3d	0.00	0.75	0.997	0.37	0.65	0.999
S4a	0.11	0.71	0.997	0.31	0.59	0.999
S4b	0.21	0.70	0.998	0.34	0.60	0.999
S4c	0.24	0.76	0.997	0.37	0.62	0.999
S4d	0.22	0.72	0.997	0.35	0.61	0.999

Table R3: Correlations between the cloud radiative effects and the cloud properties for the two major clusters characterized by low N_{int} values (L) and high N_{int} values (H). For the SW (LW) radiation, results are presented in case of the Spearman (Pearson) correlation.

Properties	$\mathrm{CRE_{SW,B}}$		$\mathrm{CRE_{SW,T}}$		$\mathrm{CRE_{LW,B}}$		$\mathrm{CRE_{LW,T}}$	
	L	H	L	H	L	H	L	H
Q_{L}	−0.935	−0.988	−0.930	−0.978	−0.016	−0.309	0.216	0.303
τ	−0.992	−0.994	−0.983	−0.986	0.028	−0.324	0.195	0.291
N_{int}	−0.446	−0.128	−0.410	−0.105	0.419	0.202	-0.259	−0.067
r_{int}	−0.343	−0.867	−0.353	−0.854	−0.311	−0.365	0.323	0.268
CBH	0.143	−0.213	−0.057	−0.292	−0.311	−0.239	0.752	0.786
CTH	−0.122	−0.604	−0.201	−0.663	−0.302	−0.376	0.783	0.717
H	−0.776	−0.921	−0.787	−0.925	−0.024	−0.386	0.217	0.300
f_{ad}	−0.126	−0.271	−0.129	−0.256	−0.003	0.144	0.215	0.194

Table R4: Explained variance and cumulative explained variance from different components obtained by the rotational component analysis (RC).

	RC-1	RC-2	RC-3	RC-4	RC-5	RC-6	RC-7	RC-8	RC-9
Explained variance (%)	33.8	35.5	14.8	13.6	2.10	0.10	0.10	0.00	0.00
Cumulative proportion (%)	33.8	69.3	84.1	97.7	99.8	99.9	100	100	100

Table R5: Pearson correlations between the logarithm of the cloud properties and the rotational components (RC). Degree of correlation (absolute values): (a) very weak: below 0.2, (b) weak: [0.2, 0.4), (c) moderate: [0.4, 0.6), (d) strong: [0.6, 0.8), and (e) very strong [0.8, 1.0].

Properties	RC-1	RC-2	RC-3	RC-4
CBH	0.969	0.025	−0.001	0.201
CTH	0.919	−0.282	0.076	0.237
Γ_{ad}	−0.896	−0.014	0.073	−0.183
τ	−0.062	−0.971	−0.192	−0.125
Q_{L}	0.036	−0.968	−0.240	0.052
H	0.177	−0.937	0.285	0.094
f_{ad}	−0.010	−0.099	−0.995	−0.025
N_{int}	−0.518	−0.250	−0.244	−0.778
r_{int}	0.382	−0.536	−0.314	0.681

Table R6: Input parameters for the RRTMG model.

Parameter	Value
Cosine of solar zenith angle	0.70
Carbon dioxide concentration	399 ppm
Ultraviolet/Visible surface albedo for direct radiation	0.05
Ultraviolet/Visible surface albedo for diffuse radiation	0.05
Near-infrared surface albedo for direct radiation	0.30
Near-infrared surface albedo for diffuse radiation	0.30

Table R7: Simulated scenarios. For scenarios S1–S3, three individual simulations (sub-cases) have been conducted according to different values for the droplet number concentration.

Scenarios			
Ref.	Double–moment scheme		
S1	Single–moment scheme		
S2	Vertical homogeneous model		
S3	Sub–adiabatic model		
S4	Mean vertical N_{d} profile		
Sub-cases	a. 220 cm^{-3}	b. N_{int}	c. 480 cm^{-3}

Table R8: Mean and standard deviation of modeled CREs (W m^{-2}) for the SW, LW, and NET (SW + LW) radiation for the reference simulation over all case days. ATM stands for the atmospheric cloud radiative effect defined as the difference between the CREs at the TOA and BOA.

Ref.	$\mathrm{CRE_{SW}}$	$\mathrm{CRE_{LW}}$	$\mathrm{CRE_{NET}}$
TOA	-348.7 ± 78.39	17.51 ± 10.04	-331.2 ± 77.27
ATM	32.94 ± 12.11	-39.16 ± 13.14	-6.225 ± 12.98
BOA	-381.6 ± 86.95	56.66 ± 9.746	-324.9 ± 86.51

Table R9: Mean CRE ($\mathrm{W\,m^{-2}}$) for the SW radiation. Results are given as differences between the new scenario minus the reference simulation (Δ). The root mean square error (RMSE) in $\mathrm{W\,m^{-2}}$ and the Pearson (Pears.) correlation between the new scenarios and the reference simulation are also given.

Scen.	$\mathrm{CRE_{SW,B}}$			$\mathrm{CRE_{SW,T}}$		
	Δ	RMSE	Pears.	Δ	RMSE	Pears.
S1a	−39.2	46.4	0.960	−40.1	47.0	0.952
S1b	−7.04	11.7	0.995	−6.53	11.7	0.994
S1c	−2.59	23.4	0.964	−1.86	24.3	0.951
S2a	−26.1	39.2	0.943	−27.1	39.8	0.930
S2b	7.74	14.2	0.991	8.19	13.6	0.990
S2c	12.9	32.4	0.943	13.7	33.6	0.921
S3a	−31.1	41.4	0.950	−32.9	42.9	0.937
S3b	1.47	10.6	0.993	1.17	10.0	0.992
S3c	6.59	27.7	0.953	6.55	29.0	0.934
S4	−3.13	16.7	0.983	−3.16	17.2	0.977

Table R10: Correlations between the cloud radiative effects for the reference simulation (Ref.) and the cloud properties. For the SW (LW) radiation, results are presented in case of the Spearman (Pearson) correlation.

Properties	$\mathrm{CRE_{SW,B}}$	$\mathrm{CRE_{SW,T}}$	$\mathrm{CRE_{LW,B}}$	$\mathrm{CRE_{LW,T}}$
	Spearman		Pearson	
Q_L	−0.957	−0.955	−0.129	0.181
τ	−0.994	−0.987	0.104	0.148
N_int	−0.471	−0.431	0.428	−0.290
r_int	−0.446	−0.460	−0.395	0.344
CBH	0.148	0.063	−0.389	0.752
CTH	0.143	−0.220	−0.428	0.765
H	−0.795	−0.812	−0.200	0.226
f_ad	−0.284	−0.273	0.145	0.134

Table R11: Mean CRE ($W\,m^{-2}$) for the LW radiation. Results are given as differences between the new scenario minus the reference simulation (Δ). The root mean square error (RMSE) in $W\,m^{-2}$ and the Pearson (Pears.) correlation between the new scenarios and the reference simulation are also given.

Scen.	$CRE_{LW,B}$			$CRE_{LW,T}$		
	Δ	RMSE	Pears.	Δ	RMSE	Pears.
S1a	−0.11	0.48	0.999	−0.04	0.19	1.000
S1b	−0.05	0.40	0.999	−0.03	0.18	1.000
S1c	−0.01	0.50	0.999	−0.01	0.22	1.000
S2a	0.40	0.79	0.998	0.23	0.51	0.999
S2b	0.51	0.82	0.998	0.27	0.53	0.999
S2c	0.55	0.85	0.998	0.29	0.54	0.999
S3a	−0.05	0.74	0.997	0.33	0.64	0.999
S3b	−0.01	0.73	0.997	0.36	0.65	0.999
S3c	0.02	0.83	0.996	0.37	0.68	0.998
S4	−0.02	0.49	0.999	−0.02	0.22	1.000

References

[1] J. Quaas, O. Boucher, and U. Lohmann, "Constraining the total aerosol indirect effect in the lmdz and echam4 gcms using modis satellite data," *Atmos. Chem. Phys.*, vol. 6, no. 4, pp. 947–955, 2006.

[2] D. P. Grosvenor, O. Sourdeval, P. Zuidema, A. Ackerman, M. D. Alexandrov, R. Bennartz, R. Boers, B. Cairns, J. C. Chiu, M. Christensen, H. Deneke, M. Diamond, G. Feingold, A. Fridlind, A. Hünerbein, C. Knist, P. Kollias, A. Marshak, D. McCoy, D. Merk, D. Painemal, J. Rausch, D. Rosenfeld, H. Russchenberg, P. Seifert, K. Sinclair, P. Stier, B. van Diedenhoven, M. Wendisch, F. Werner, R. Wood, Z. Zhang, and J. Quaas, "Remote sensing of droplet number concentration in warm clouds: A review of the current state of knowledge and perspectives," *Rev. Geophys.*, vol. 56, no. 2, pp. 409–453, 2018.

[3] S. Zhou, S. Collier, D. A. Jaffe, and Q. Zhang, "Free tropospheric aerosols at the mt. bachelor observatory: more oxidized and higher sulfate content compared to boundary layer aerosols," *Atmos. Chem. Phys.*, vol. 19, no. 3, pp. 1571–1585, 2019.

[4] P. Kupiszewski, C. Leck, M. Tjernström, S. Sjogren, J. Sedlar, M. Graus, M. Müller, B. Brooks, E. Swietlicki, S. Norris, and A. Hansel, "Vertical profiling of aerosol particles and trace gases over the central arctic ocean during summer," *Atmos. Chem. Phys.*, vol. 13, no. 24, pp. 12405–12431, 2013.

[5] R. J. Weber and P. H. McMurry, "Fine particle size distributions at the mauna loa observatory, hawaii," *J. Geophys. Res. Atmos.*, vol. 101, no. D9, pp. 14767–14775, 1996.

[6] A. L. Igel, A. M. L. Ekman, C. Leck, M. Tjernstrm, J. Savre, and J. Sedlar, "The free troposphere as a potential source of arctic boundary layer aerosol particles," *Geophys. Res. Lett.*, vol. 44, no. 13, pp. 7053–7060, 2017.

[7] G. C. Roberts, D. A. Day, L. M. Russell, E. J. Dunlea, J. L. Jimenez, J. M. Tomlinson, D. R. Collins, Y. Shinozuka, and A. D. Clarke, "Characterization of particle cloud droplet activity and composition in the free troposphere and the boundary layer during intex-b," *Atmos. Chem. Phys.*, vol. 10, no. 14, pp. 6627–6644, 2010.

[8] F. Bianchi, J. Tröstl, H. Junninen, C. Frege, S. Henne, C. R. Hoyle, U. Molteni, E. Herrmann, A. Adamov, N. Bukowiecki, X. Chen, J. Duplissy, M. Gysel, M. Hutterli, J. Kangasluoma, J. Kontkanen, A. Kürten, H. E. Manninen, S. Münch, O. Peräkylä, T. Petäjä, L. Rondo, C. Williamson, E. Weingartner, J. Curtius, D. R. Worsnop, M. Kulmala, J. Dommen, and U. Baltensperger, "New particle formation in the free troposphere: A question of chemistry and timing," *Science*, vol. 352, no. 6289, pp. 1109–1112, 2016.

[9] C. Rose, K. Sellegri, I. Moreno, F. Velarde, M. Ramonet, K. Weinhold, R. Krejci, M. Andrade, A. Wiedensohler, P. Ginot, and P. Laj, "Ccn production by new particle formation in the free troposphere," *Atmos. Chem. Phys.*, vol. 17, no. 2, pp. 1529–1541, 2017.

[10] J.-P. Pietikäinen, T. Markkanen, K. Sieck, D. Jacob, J. Korhonen, P. Räisänen, Y. Gao, J. Ahola, H. Korhonen, A. Laaksonen, and J. Kaurola, "The regional climate model remo (v2015) coupled with the 1-d freshwater lake model flake (v1): Fenno-scandinavian climate and lakes," *Geosci. Model Dev.*, vol. 11, no. 4, pp. 1321–1342, 2018.

[11] M. Giorgetta, E. Roeckner, T. Mauritsen, J. Bader, T. Crueger, M. Esch, S. Rast, L. Kornblueh, H. Schmidt, S. Kinne, C. Hohenegger, B. Möbis, T. Krismer, K.-H. Wieners, and B. Stevens, "The atmospheric general circulation model echam6 - model description," *Max-Planck-Institut für Meteorologie*, vol. 135, 01 2013.

[12] R. Heinze, A. Dipankar, C. C. Henken, C. Moseley, O. Sourdeval, S. Trömel, X. Xie, P. Adamidis, F. Ament, H. Baars, C. Barthlott, A. Behrendt, U. Blahak, S. Bley, S. Brdar, M. Brueck, S. Crewell, H. Deneke, P. Di Girolamo, R. Evaristo, J. Fischer, C. Frank, P. Friederichs, T. Göcke, K. Gorges, L. Hande, M. Hanke, A. Hansen, H.-C. Hege, C. Hoose, T. Jahns, N. Kalthoff, D. Klocke, S. Kneifel, P. Knippertz, A. Kuhn, T. van Laar, A. Macke, V. Maurer, B. Mayer, C. I. Meyer, S. K. Muppa, R. A. J. Neggers, E. Orlandi, F. Pantillon, B. Pospichal, N. Röber, L. Scheck, A. Seifert, P. Seifert, F. Senf, P. Siligam, C. Simmer, S. Steinke, B. Stevens, K. Wapler, M. Weniger, V. Wulfmeyer, G. Zängl, D. Zhang, and J. Quaas, "Large-eddy simulations over germany using icon: a comprehensive evaluation," *Q. J. R. Meteorol. Soc.*, vol. 143, no. 702, pp. 69–100, 2017.

Answers to Anonymous Referee #3

We thank the anonymous referee #3 for his/her constructive comments and suggestions that certainly have improved the manuscript significantly. We revised the manuscript according to his/her comments and the comments of anonymous referees #1 and #2. In the following,

- *referee's comments are given in italic*,
- our answers are outlined in normal format, and
- **textual changes in the manuscript are given in bold format**.

We would like inform the anonymous referee #3 about the following changes:

1. Driven by the specific comment (SC) #18 of anonymous referee #3 (SC3.18), we decided to drop scenario S4 from the analysis. The difference between the sub-adiabatic model (S3) and the modified one (S4) is that the latter accounts for the depletion of the liquid water content due to entrainment, precipitation, and freezing drops. Consequently, we wanted to check whether S4 captures better the vertical stratification of the modeled low-level clouds and, accordingly, if it approximates the CREs of the reference simulation with better accuracy. Since S4 does not provide any further insight, we now have decided to drop this scenario. However, we do confirm that, by considering all the case days in the analysis, we came to the same conclusions as for 3 June. As a confirmation, we updated the Tables and attached them at the end of this document. The referee is referred to Tables R1–R3.

2. In all scenarios, we decided to drop sub-case d, which employs two fixed values for the droplet number concentration representing the two modes in the corresponding histogram for 3 June 2016. This scenario separates clouds into a cluster with low/high clouds. Considering the vertical variability of the droplet number concentration, the latter clustering will link low clouds (within the boundary layer) with high N_d and, accordingly, high clouds with lower N_d values. Thus, for all scenarios, employing such values for N_d are able to approximate the reference radiative transfer simulation very well. Only the radiative transfer simulation that is supplied by the droplet number concentration weighted over the cloud geometrical extent, i.e., N_int (sub-case b) leads to smaller differences when compared to the reference simulation. However, we do confirm that, by considering all the case days into the analysis, we came to the same conclusions as for 3 June. Note that, for the latter case, the clustering was conducted on the mean N_int over all case days. As a confirmation, we updated the Tables and attached them at the end of this document. The referee is referred to Tables R1–R3.

3. We decided to add a new scenario as a replacement of sub-case d, whereby radiative transfer simulations are conducted for a mean vertical profile of the droplet number concentration over all case days. Tables R9–R11 summarize the new results. In brief, this scenario is considered as an improvement compared to the clustering case. The following parts were included within the text:

   Section 5.1.2: **Last but not least, by replacing the vertical profile of N_d by the**

mean profile of N_d over all case days (see Fig. 2), emulates the cloud radiative effects of the reference simulation quite well. Accordingly, scenario S4 slightly undersimates the mean SW CREs, with an mean error up to $-3.16\,\mathrm{W\,m^{-2}}$ and a RMSE up to $17.2\,\mathrm{W\,m^{-2}}$ for both BOA and TOA. In fact, this scenario outperforms the rest scenarios (S1–S3), except from the sub-case b (N_{int}) in all scenarios. For an illustration of the excellent linear correlation between the reference simulation and S4 by means of a bivariate kernel density (BKD) plot, the reader is referred to Fig. B1 in Appendix B. One can see that the CREs computed by these scenarios are in a very good agreement almost everywhere except towards larger values of the CREs in case of the SW radiation, with Pearson correlations larger than 0.977 for both BOA and TOA.

Section 6: **By employing a more representative profile for the N_d, i.e., a mean vertical profile of N_d over all case days leads to a rather good approximation; the RMSE is below $17.2\,\mathrm{W\,m^{-2}}$. This points to the need to better account for prognostic N_d calculations.**

Appendix B: **In sect. 5.1.2, by conducting idealized radiative transfer simulations, we estimated the impact of the representation of cloud properties in ICON-LEM on the cloud radiative effects (CREs). Special emphasis was given on identifying the droplet number concentration (N_d), which approximates the microphysical and radiative properties of low-level clouds as simulated by ICON-LEM (reference scenario). A radiative transfer simulation, which employs a mean vertical profile of N_d over all the case days (scenario S4), approximates the CREs of the reference scenario quite well. Figure B1 depicts the excellent linear correlation between the reference simulation and S4 by means of a bivariate kernel density (BKD)**.

4. Following the general comment of anonymous referee #2 for shortening the manuscript given the redundancy of many of the results shown in this study and his/her relevant specific comments (SC), i.e., (SC2.12) and (SC2.25):

   - We decided to drop Fig. B1. Figure B1 illustrates the bivariate kernel density (BKD) between the cloud optical thickness and the liquid water path on a logarithmic scale. Considering the comprehensive explanation given in Sect. 3.3.1, we decided that this illustration did not provide any additional information.
   - Figures 6 and 7 have been revised. Now, they illustrate results only for TOA (see Figs R2 and R3).
   - We now focus only on the rotational component analysis. The mention of the principal component analysis have been significantly reduced. In addition, we removed the relevant information from Table 3. For the updated version of the Table, the referees are referred to Table R5. Additionally, we replaced Figure 5 by Table R4. This table lists the contribution of each rotational component to the total variance.

Answers to general comments (GC) from referee #3 (GC3)

(GC3.1) *The robustness of the obtained results, such as principal components of cloud properties and their relationship with the CRE, should be discussed. These results are obtained only from the one-day data. However, the daily variation is large as shown in Table. 1, although the authors claim that the day has similar properties to the six-day average.*

We revised our manuscript according to the comments of anonymous referee #3 and the comments of anonymous referees #1 and #2. We further extended our analysis over all case days to improve the robustness of our results. Now, sections 3.2 and 5 outline our findings for all case days.

Answers to specific comments (SC) from referee #3 (SC3)

(SC3.1) *Order of diagrams in Figures*

The order of sub-figures has been revised.

(SC3.2) *Significant figures of values.*

The number of significant figures of values has been revised.

(SC3.3) *Brief descriptions of the model and configurations of the experiment are necessary, such as kind of governing equations, vertical levels, and calculation domains.*

We revised the description of ICON-LEM (Section 2.1) according to the anonymous referee 3 and the specific comment (SC3) of anonymous referee 1:.

The ICON unified modeling framework was co-developed by the German meteorological service (DWD) and the Max Planck institute for meteorology (MPI-M) in order to support climate research and weather forecasting. Within the HD(CP)2 project, ICON was further extended towards large eddy simulations with realistic topography **and** open boundary conditions. This resulted in ICON-LEM **deployed in restricted areas that are centered on Germany and the Tropical Atlantic [1]. The equations utilized by the model are based on the prognostic variables given by Gassmann and Herzog [2]. These variables comprise the horizontal and vertical velocity components, the density of moist air, the virtual potential temperature, and the mass and number densities of traces, e.g., specific humidity, liquid water, and different ice hydrometeors. A comprehensive description of the model and its governing equations is found in Dipankar et al. [3] and Wan et al., [4].** Concerning turbulence parameterization, the three-dimensional Smagorinsky scheme is employed [3]. The activation of cloud condensation nuclei (CCN) is based on the parameterization of Seifert and Beheng [5] and modified in order to account for the consumption of CCNs due to their activation into cloud droplets. The CCN concentration is then parameterized following the pressure profile and the vertical velocity [6].

Simulations are carried out for three different domains with 624 m, 312 m, and 156 m

horizontal resolution. The model domains consist of 150 vertical levels, with resolutions ranging from ∼25 m to 70 m within the boundary layer, and from 70 m to 355 m further up until the top of the domain at 21 km. For each of the aforementioned grids, data is stored as one-dimensional (1D) profiles every 10 sec, two-(2D), and 3D snapshots [1]. In case of the 3D output, the simulation data is interpolated from the original grids (e.g., 156 m) to a 1 km grid, the 3D coarse data, and 300 m grid, the so-called HOPE data. The latter output has been created for the purpose of model evaluation with ground-based observations from the HD(CP)^2 Observational Prototype Experiment (HOPE) that took place near Jülich [7]**and is limited to a domain size of about ∼45 km^2. Note here that for the 2D and 3D output, data is stored at day- and night-time frequency. Day-time frequency begins at 06:00 UTC and lasts until 00:00 UTC, while night-time starts at midnight and lasts until 06:00 UTC. The 2D data is stored with a day-time and night-time frequency of 10 sec and 5 min, respectively. The 3D coarse data has day-time frequency of 10 min (1 hour at night-time). In this study, the 3D HOPE data has been used that is stored only at a day-time frequency of 15 min.**

(SC3.4) *Equation 15. The fact 9/5 seems to be 3/2. The power of (18w4 fad ad) is not 1/6 but -1/6.*

The referee is correct. This section has been revised following also the specific comment #2 of the anonymous referee #1 (SC1.2):

P6 L24: **while the factor** $2/3$ **is a scale factor resulting from the constant liquid water content and effective radius with height [8]**.

P7 L21: **Compared to Eq. (7), Eq. (10) leads to a factor of** $5/9$**, meaning that the sub-adiabatic liquid water path is** $5/6$ **times the one of the vertically homogeneous model [9]**.

P8 L11: **For vertically constant** q_{L} **and** r_{eff}**, this can be interpreted as the cloud optical thickness coming from the vertical homogeneous model (see Eq. 7). According to the sub-adiabatic cloud model, the cloud optical thickness is linked to the liquid water path and the effective radius [10],**

$$\tau = \frac{9}{5}\frac{Q_{\mathrm{L}}}{\rho_{\mathrm{w}} \cdot r_{\mathrm{eff}}}$$

Alternatively, substituting r_{eff} **from Eq. (13) in Eq. (15), the cloud optical thickness is given by,...**

(SC3.5) *P9 L18: A close relation between the effective radius and the droplet number concentration exist. Why does the effective radius have a single-mode distribution in spite of the bimodal distribution of the droplet number concentration?*

The effective radius is defined as the ratio of the third to the second moments of the droplet size distribution and the second moment of the size distribution is closely related to the liquid water content. Accordingly, the two modes of N_{d} do not need to be at two different size regimes in r_{eff}.

(SC3.6) *P9 L18: "exist" -¿ exists.*

Corrected.

(SC3.7) *Figure 2 and Figure 3 (b) Both diagrams show the distribution of the Nd, the magnitude of the median is quite different. What makes such a big difference?*

Figure 2 shows the histogram as a box-whisker plot of the droplet number concentration for each model level. On the other hand, Fig. 3 depicts the mean profile of N_{d} normalized over the cloud geometrical extent, illustrating the vertical change in N_{d} within individual clouds. The aforementioned normalization is the reason of the differences between the two figures. As we aforementioned, we further extended the analysis over all case days. Thus, fig. (2) and fig. (3) have been revised (see Fig. R1 and Fig. R2).

(SC3.8) *Section 3.3.1: There is a large relationship between Q_{L} and fad, and then this analysis has multicollinearity problem. Therefore, the amount obtained must be much interpolated more carefully. Furthermore, I do not agree that the is proportional to $Q_{\mathrm{L}}^{5/6}$, since Eq. (15) has f_{ad}.*

We acknowledge referee's concerns with respect to our multicollinearity analysis. However, we respectfully disagree on this point. In this section, we tried to predict the cloud optical thickness derived from the output of ICON-LEM (by using Eq. 14), via employing the relevant equation suggested by the sub-adiabatic model, i.e., Eq. (15). In the analysis, results from all case days has been considered. By employing the sub-adiabatic model, i.e., model $Y_4(Q_{\mathrm{L}}, f_{\mathrm{ad}}, N_{\mathrm{int}})$, we managed to approximate the cloud optical thickness quite well. In fact, Y_4 explains 99.9% of the variance in cloud optical thickness with a root mean square error of 0.027. In addition, we found only a weak correlation between the liquid water path and the sub-adiabatic factor (Pearson correlation of 0.28), in contrast to the very strong correlation between the cloud optical thickness and the liquid water path (Pearson correlation of 0.99). The referee is referred to Figure 4 in section 4.

However, we did revise section 3.1.1, in order to avoid any confusion. The following parts have been included:

P13 L2: **With this intention, an effort has been conducted to predict the cloud optical thickness derived from Eq. (14) by employing the sub-adiabatic model and Eq. (15).**

Caption of Table 2: Prediction of cloud optical thickness by ordinary least squares regression method:

P13 L20: **In fact, model $Y_4(Q_{\mathrm{L}}, f_{\mathrm{ad}}, N_{\mathrm{int}})$ supports the applicability of the sub-adiabatic model since it is able to approximate the cloud optical thickness with high accuracy** (RMSE = 0.027)

(SC3.9) *P17 L19: resulting in a net cooling. There exists large uncertainty, and I wondered if the negative value has statistical significance.*

We acknowledge the referee's concerns with regard to the uncertainty in the resulting cloud radiative effects. However, low-level clouds tend to be rather warm and, hence, having a generally

small influence on the TOA lowngwave radiation. In contrast, they are characterized by a large albedo, leading to an overall net cooling effect. The latter net cooling effect has been reported by several observational studies [11, 12, 13, 14, 15, 16].

(SC3.10) *P18 L1, Table 6 lists the mean CREs between... It should be "Table 6 lists the difference of the mean CREs between...". The same corrections are necessary for the following sentences.*

We thank the referee for highlighting the mistake. The text has been revised.

(SC3.11) *P18 L8. For a given liquid water path, the smaller... Check if it is grammatically correct.*

We double-checked the sentence and think it is correct.

(SC3.12) *P18 L16, a Pearson correlation of 0.950 (0.928) is yielded. The values are 0.952 (0.930) in Table 6.*

We thank the referee for highlighting the mismatches between the table and the text. Nevertheless, we now extended the analysis over all days and, thus, tables and related text have been revised.

(SC3.13) *P18 L19, a Pearson correlation of 0.995. The value is 0.996 in Table 6.*

The same as in (SC3.12).

(SC3.14) *P18 L19, and P20 L13, no suprise considering surprise*

The text has been revised as follows:

The latter can be explained by the way the droplet number concentration is derived (see Eq. 4)...

(SC3.15) *P18 L25, of about -6.52 Wm^{-2} with a RMSE of 10.4 Wm^{-2} for b and -9.31 Wm^{-2} with a RMSE of 19.4 Wm^{-2} for d The sign of -6.52 and -9.31 is different from that in Table 6. The mismatch is also in the number of -0.11 and -3.64 at Page 19 Line 1.*

We thank the referee for highlighting the mismatches between the table and the text. We have now extended the analysis over all days and, thus, tables and related text have been revised.

(SC3.16) *Table 6. The names of Scen. are wrong.*

The referee is correct. However, we now have decided to replace the sub-scenario (d, clusters) with a new scenario 4, whereby we employ the mean droplet number concentration profile over all days. Accordingly, Table 6 has been revised. The referee is referred to the section **General changes**.

(SC3.17) *P19 L3, For instance, in case of the adiabatic scenarios... the sub-adiabatic.*

The text is revised accordingly.

(SC3.18) *P19 L7, slightly larger scatter is found for S4 as compared to S3. Why is the result of S4 worth than that of S3?*

The difference between the sub-adiabatic model (S3) and the modified one (S4) is that the latter accounts for the depletion of the liquid water content due to entrainment, precipitation, and freezing drops. Consequently, we wanted to check whether it captures better the vertical stratification of the modeled low-level clouds and, accordingly, if it approximates the CREs of the reference simulation with better accuracy. Since S4 does not provide any further insight, we now have decided to drop this scenario. However, we do confirm that, by considering all the case days into the analysis, we came to the same conclusions as for 3 June. As a confirmation, we updated the Tables and attached them at the end of this document. The referee is referred to Tables R1–R3.

(SC3.19) *P20 L7: -0.76. It has different significant figures from that in Table 7. Same for 0.21 at P20 L13.*

We thank the referee for highlighting the mismatches. We have now extended the analysis over all days and, thus, tables and related text have been revised.

(SC3.20) *Logarithmic axis is preferred. The saturation may not be found in the logarithmic plot.*

We acknowledge the referee's suggestion for the logarithmic axis. However, we respectfully disagree on this point. Firstly, we would like to highlight that, in the SW radiation, an excellent monotonic relation is found between the CREs and cloud optical thickness, liquid water path, and cloud geometrical extent for both BOA and TOA. Secondly, the SW CRE is negative and the logarithm of a negative number is undefined. Even if we take the absolute value of the CRE, we still see the monotonic relation, but, it is less pronounced.

(SC3.21) *P21 L3, e.g., Fig. 6 panels (a) or (b) with Fig. 8 panel (b) Fig. 8 panel (a).*

We thank the referee for pointing to the mistake. Nevertheless, we now have reduced the amount of plots. Following the general comment of the anonymous referee #2, we now illustrate only the results for TOA (see Figs. R3 and R4).

(SC3.22) *P21 L3, The resulting Spearman and Pearson correlations larger than 0.96 and 0.91, respectively. The values seem to be 0.816 and 0.914.*

The correct panels of Fig. 8 are (a) and (d). Accordingly, the Spearman correlation is 0.96 and 0.935. Nevertheless, we now extended the analysis over all case days and, thus, the correlations have slightly changed.

(SC3.23) *P21 L14, with Spearman and Pearson correlations above -0.796 and -0.82, respectively. The values should be -0.820 and -0.796. The author should mention that these values are only for high values of the droplet number concentration.*

The referee is correct. However, we now have decided to replace the sub-scenario (d, clusters)

with a new scenario 4, whereby we employ the mean droplet number concentration profile over all case days. For details with respect to the relevant changes, the referee is referred to section **General changes**.

List of Figures

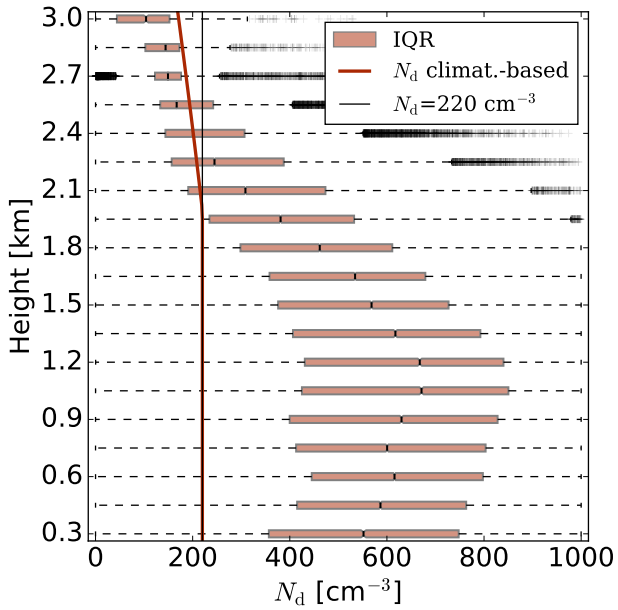

Figure R1: Box-whisker plot of the droplet number concentration for all the case days on average, describing the histograms of N_d simulated for different model levels by the double moment scheme of ICON-LEM. Boxes illustrate interquartile range (IQR), dark red line denotes the climatology-based N_d profile adopted by ECHAM, and the thin black line demonstrates the constant N_d profile of 220 cm^{-3}.

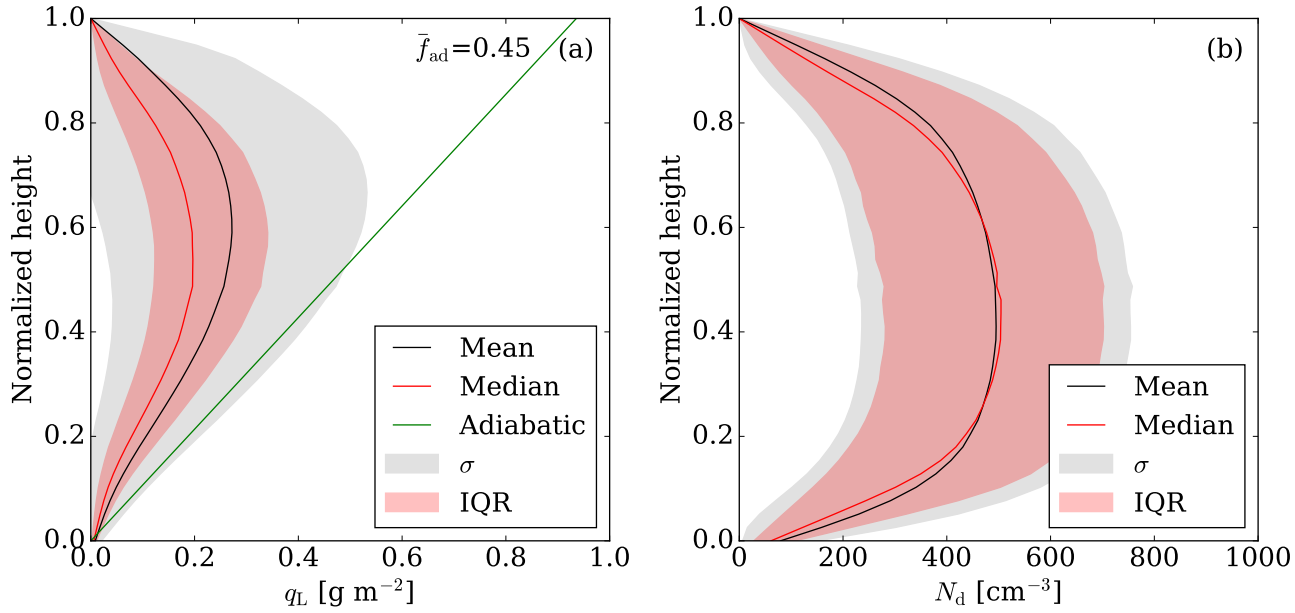

Figure R2: ICON-LEM simulated mean (a) q_L and (b) N_d profiles for all the case days on average. Profiles are normalized over height from the CBH to the CTH. Black lines denote the mean, red solid lines the median, gray shaded areas the standard deviation, red shaded areas the interquartile range (IQR), and the green solid line outline the mean adiabatic q_L profile characterized by a mean adiabatic fraction ($\bar{f}_{ad}$) of 0.45.

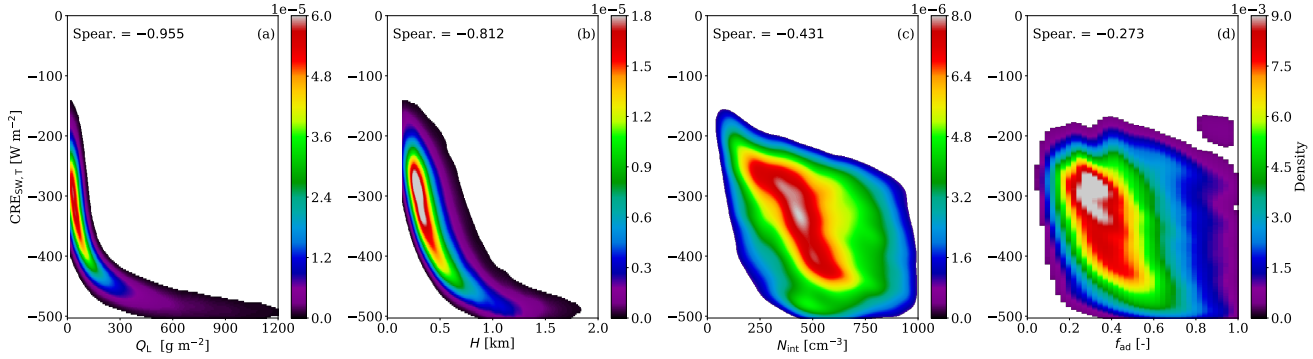

Figure R3: Bivariate kernel density (BKD) between the reference simulation (Ref.) and the cloud properties that are essential for the derivation of the cloud optical thickness that is one of the fundamental properties describing the SW cloud radiative effect. Panels illustrate the BKD between the $CRE_{SW,T}$ and (a) Q_L, (b) H, (c) N_{int}, and (d) f_{ad}. The corresponding Spearman (Spear.) correlations are highlighted.

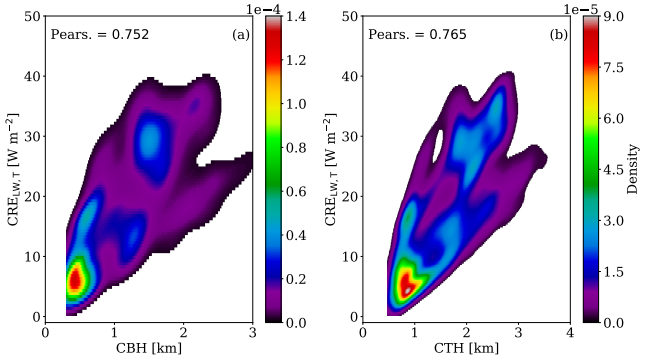

Figure R4: Bivariate kernel density (BKD) between the reference simulation (Ref.) and the cloud properties describing the LW cloud radiative effect at the TOA and (a) CBH and (b) CTH. The corresponding Pearson (Pears.) correlations are highlighted.

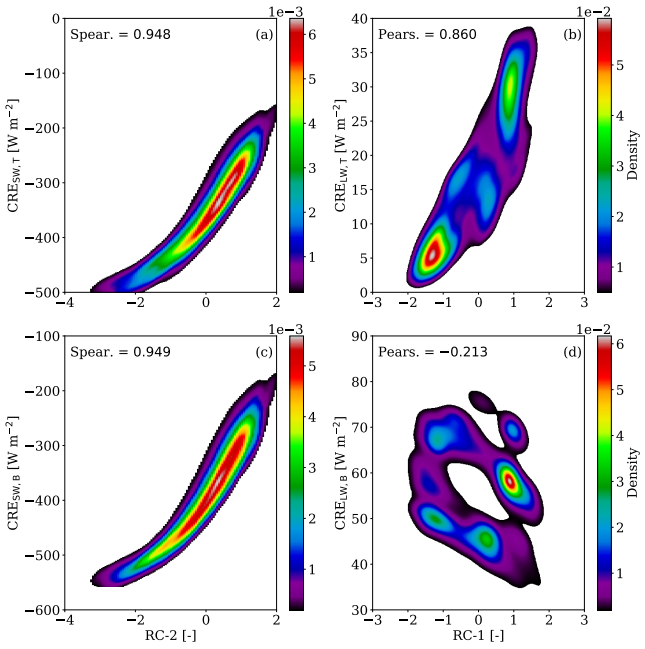

Figure R5: For the reference simulation (Ref.), bivariate kernel density (BKD) between CRE_{SW} and the second rotational component (RC-2) at (a) TOA, (c) BOA and between CRE_{LW} and the first rotational component (RC-1) at (b) TOA, (d) BOA. The corresponding Spearman (Spear.) and Pearson (Pears.) correlations are highlighted for the SW and LW radiation, respectively.

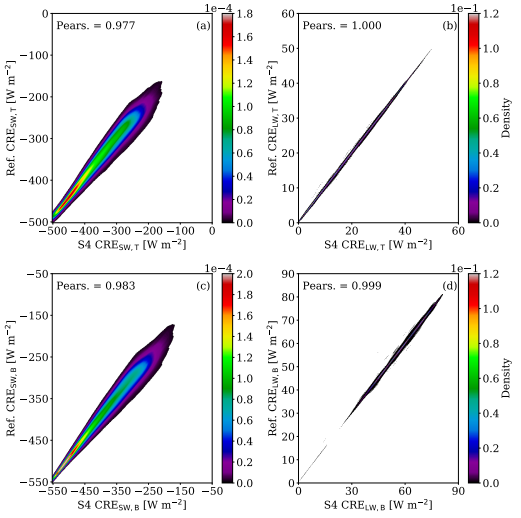

Figure R6: Bivariate kernel density (BKD) between the reference simulation (Ref.) and the scenario that employs the mean vertical N_{d} profile (S4). For the CREs, BKD are presented for the SW radiation at the TOA (a) and BOA (c), and for the LW radiation at the TOA (b) and BOA (d). The corresponding Pearson (Pears.) correlations are highlighted.

List of Tables

Table R1: Mean CRE ($\mathrm{W\,m^{-2}}$) for the SW radiation. Results are given as differences between the new scenario minus the reference simulation (Δ). The root mean square error (RMSE) in $\mathrm{W\,m^{-2}}$ and the Pearson (Pears.) correlation between the new scenarios and the reference simulation are also given.

Scen.	$\mathrm{CRE_{SW,B}}$			$\mathrm{CRE_{SW,T}}$		
	Δ	RMSE	Pears.	Δ	RMSE	Pears.
S1a	−39.2	46.4	0.960	−40.1	47.0	0.952
S1b	−7.04	11.7	0.995	−6.53	11.7	0.994
S1c	−2.59	23.4	0.964	−1.86	24.3	0.951
S1d	−6.57	17.6	0.982	−5.99	18.0	0.977
S2a	−26.1	39.2	0.943	−27.1	39.8	0.930
S2b	7.74	14.2	0.991	8.19	13.6	0.990
S2c	12.9	32.4	0.943	13.7	33.6	0.921
S2d	8.53	22.6	0.971	9.10	22.9	0.964
S3a	−31.1	41.4	0.950	−32.9	42.9	0.937
S3b	1.47	10.6	0.993	1.17	10.0	0.992
S3c	6.59	27.7	0.953	6.55	29.0	0.934
S3d	2.29	19.1	0.976	2.09	19.5	0.969
S4a	−28.7	40.1	0.947	−30.3	41.4	0.934
S4b	4.97	11.7	0.993	4.80	11.1	0.992
S4c	10.1	29.9	0.949	10.2	31.2	0.928
S4d	5.72	20.4	0.975	5.67	20.8	0.967

Table R2: Mean CRE ($\mathrm{W\,m^{-2}}$) for the LW radiation. Results are given as differences between the new scenario minus the reference simulation (Δ). The root mean square error (RMSE) in $\mathrm{W\,m^{-2}}$ and the Pearson (Pears.) correlation between the new scenarios and the reference simulation are also given.

Scen.	$\mathrm{CRE_{LW,B}}$			$\mathrm{CRE_{LW,T}}$		
	Δ	RMSE	Pears.	Δ	RMSE	Pears.
S1a	−0.11	0.48	0.999	−0.04	0.19	1.000
S1b	−0.05	0.40	0.999	−0.03	0.18	1.000
S1c	−0.01	0.50	0.999	−0.01	0.22	1.000
S1d	−0.04	0.45	0.999	−0.02	0.21	1.000
S2a	0.40	0.79	0.998	0.23	0.51	0.999
S2b	0.51	0.82	0.998	0.27	0.53	0.999
S2c	0.55	0.85	0.998	0.29	0.54	0.999
S2d	0.52	0.83	0.998	0.28	0.53	0.999
S3a	−0.05	0.74	0.997	0.33	0.64	0.999
S3b	−0.01	0.73	0.997	0.36	0.65	0.999
S3c	0.02	0.83	0.996	0.37	0.68	0.998
S3d	0.00	0.75	0.997	0.37	0.65	0.999
S4a	0.11	0.71	0.997	0.31	0.59	0.999
S4b	0.21	0.70	0.998	0.34	0.60	0.999
S4c	0.24	0.76	0.997	0.37	0.62	0.999
S4d	0.22	0.72	0.997	0.35	0.61	0.999

Table R3: Correlations between the cloud radiative effects and the cloud properties for the two major clusters characterized by low N_{int} values (L) and high N_{int} values (H). For the SW (LW) radiation, results are presented in case of the Spearman (Pearson) correlation.

Properties	$\mathrm{CRE_{SW,B}}$		$\mathrm{CRE_{SW,T}}$		$\mathrm{CRE_{LW,B}}$		$\mathrm{CRE_{LW,T}}$	
	L	H	L	H	L	H	L	H
Q_{L}	−0.935	−0.988	−0.930	−0.978	−0.016	−0.309	0.216	0.303
τ	−0.992	−0.994	−0.983	−0.986	0.028	−0.324	0.195	0.291
N_{int}	−0.446	−0.128	−0.410	−0.105	0.419	0.202	-0.259	−0.067
r_{int}	−0.343	−0.867	−0.353	−0.854	−0.311	−0.365	0.323	0.268
CBH	0.143	−0.213	−0.057	−0.292	−0.311	−0.239	0.752	0.786
CTH	−0.122	−0.604	−0.201	−0.663	−0.302	−0.376	0.783	0.717
H	−0.776	−0.921	−0.787	−0.925	−0.024	−0.386	0.217	0.300
f_{ad}	−0.126	−0.271	−0.129	−0.256	−0.003	0.144	0.215	0.194

Table R4: Explained variance and cumulative explained variance from different components obtained by the rotational component analysis (RC).

	RC-1	RC-2	RC-3	RC-4	RC-5	RC-6	RC-7	RC-8	RC-9
Explained variance (%)	33.8	35.5	14.8	13.6	2.10	0.10	0.10	0.00	0.00
Cumulative proportion (%)	33.8	69.3	84.1	97.7	99.8	99.9	100	100	100

Table R5: Pearson correlations between the logarithm of the cloud properties and the rotational components (RC). Degree of correlation (absolute values): (a) very weak: below 0.2, (b) weak: [0.2, 0.4), (c) moderate: [0.4, 0.6), (d) strong: [0.6, 0.8), and (e) very strong [0.8, 1.0].

Properties	RC-1	RC-2	RC-3	RC-4
CBH	0.969	0.025	−0.001	0.201
CTH	0.919	−0.282	0.076	0.237
Γ_{ad}	−0.896	−0.014	0.073	−0.183
τ	−0.062	−0.971	−0.192	−0.125
Q_{L}	0.036	−0.968	−0.240	0.052
H	0.177	−0.937	0.285	0.094
f_{ad}	−0.010	−0.099	−0.995	−0.025
N_{int}	−0.518	−0.250	−0.244	−0.778
r_{int}	0.382	−0.536	−0.314	0.681

Table R6: Input parameters for the RRTMG model.

Parameter	Value
Cosine of solar zenith angle	0.70
Carbon dioxide concentration	399 ppm
Ultraviolet/Visible surface albedo for direct radiation	0.05
Ultraviolet/Visible surface albedo for diffuse radiation	0.05
Near-infrared surface albedo for direct radiation	0.30
Near-infrared surface albedo for diffuse radiation	0.30

Table R7: Simulated scenarios. For scenarios S1–S3, three individual simulations (sub-cases) have been conducted according to different values for the droplet number concentration.

Scenarios	
Ref.	Double–moment scheme
S1	Single–moment scheme
S2	Vertical homogeneous model
S3	Sub–adiabatic model
S4	Mean vertical N_{d} profile
Sub-cases	a. 220 cm^{-3} b. N_{int} c. 480 cm^{-3}

Table R8: Mean and standard deviation of modeled CREs ($\mathrm{W\,m^{-2}}$) for the SW, LW, and NET (SW + LW) radiation for the reference simulation over all case days. ATM stands for the atmospheric cloud radiative effect defined as the difference between the CREs at the TOA and BOA.

Ref.	$\mathrm{CRE_{SW}}$	$\mathrm{CRE_{LW}}$	$\mathrm{CRE_{NET}}$
TOA	-348.7 ± 78.39	17.51 ± 10.04	-331.2 ± 77.27
ATM	32.94 ± 12.11	-39.16 ± 13.14	-6.225 ± 12.98
BOA	-381.6 ± 86.95	56.66 ± 9.746	-324.9 ± 86.51

Table R9: Mean CRE ($\mathrm{W\,m^{-2}}$) for the SW radiation. Results are given as differences between the new scenario minus the reference simulation (Δ). The root mean square error (RMSE) in $\mathrm{W\,m^{-2}}$ and the Pearson (Pears.) correlation between the new scenarios and the reference simulation are also given.

Scen.	$\mathrm{CRE_{SW,B}}$			$\mathrm{CRE_{SW,T}}$		
	Δ	RMSE	Pears.	Δ	RMSE	Pears.
S1a	−39.2	46.4	0.960	−40.1	47.0	0.952
S1b	−7.04	11.7	0.995	−6.53	11.7	0.994
S1c	−2.59	23.4	0.964	−1.86	24.3	0.951
S2a	−26.1	39.2	0.943	−27.1	39.8	0.930
S2b	7.74	14.2	0.991	8.19	13.6	0.990
S2c	12.9	32.4	0.943	13.7	33.6	0.921
S3a	−31.1	41.4	0.950	−32.9	42.9	0.937
S3b	1.47	10.6	0.993	1.17	10.0	0.992
S3c	6.59	27.7	0.953	6.55	29.0	0.934
S4	−3.13	16.7	0.983	−3.16	17.2	0.977

Table R10: Correlations between the cloud radiative effects for the reference simulation (Ref.) and the cloud properties. For the SW (LW) radiation, results are presented in case of the Spearman (Pearson) correlation.

Properties	$\mathrm{CRE_{SW,B}}$	$\mathrm{CRE_{SW,T}}$	$\mathrm{CRE_{LW,B}}$	$\mathrm{CRE_{LW,T}}$
	Spearman		Pearson	
Q_L	−0.957	−0.955	−0.129	0.181
τ	−0.994	−0.987	0.104	0.148
N_int	−0.471	−0.431	0.428	−0.290
r_int	−0.446	−0.460	−0.395	0.344
CBH	0.148	0.063	−0.389	0.752
CTH	0.143	−0.220	−0.428	0.765
H	−0.795	−0.812	−0.200	0.226
f_ad	−0.284	−0.273	0.145	0.134

Table R11: Mean CRE ($\mathrm{W\,m^{-2}}$) for the LW radiation. Results are given as differences between the new scenario minus the reference simulation (Δ). The root mean square error (RMSE) in $\mathrm{W\,m^{-2}}$ and the Pearson (Pears.) correlation between the new scenarios and the reference simulation are also given.

Scen.	$\mathrm{CRE_{LW,B}}$			$\mathrm{CRE_{LW,T}}$		
	Δ	RMSE	Pears.	Δ	RMSE	Pears.
S1a	−0.11	0.48	0.999	−0.04	0.19	1.000
S1b	−0.05	0.40	0.999	−0.03	0.18	1.000
S1c	−0.01	0.50	0.999	−0.01	0.22	1.000
S2a	0.40	0.79	0.998	0.23	0.51	0.999
S2b	0.51	0.82	0.998	0.27	0.53	0.999
S2c	0.55	0.85	0.998	0.29	0.54	0.999
S3a	−0.05	0.74	0.997	0.33	0.64	0.999
S3b	−0.01	0.73	0.997	0.36	0.65	0.999
S3c	0.02	0.83	0.996	0.37	0.68	0.998
S4	−0.02	0.49	0.999	−0.02	0.22	1.000

References

[1] R. Heinze, A. Dipankar, C. C. Henken, C. Moseley, O. Sourdeval, S. Trömel, X. Xie, P. Adamidis, F. Ament, H. Baars, C. Barthlott, A. Behrendt, U. Blahak, S. Bley, S. Brdar, M. Brueck, S. Crewell, H. Deneke, P. Di Girolamo, R. Evaristo, J. Fischer, C. Frank, P. Friederichs, T. Göcke, K. Gorges, L. Hande, M. Hanke, A. Hansen, H.-C. Hege, C. Hoose, T. Jahns, N. Kalthoff, D. Klocke, S. Kneifel, P. Knippertz, A. Kuhn, T. van Laar, A. Macke, V. Maurer, B. Mayer, C. I. Meyer, S. K. Muppa, R. A. J. Neggers, E. Orlandi, F. Pantillon, B. Pospichal, N. Röber, L. Scheck, A. Seifert, P. Seifert, F. Senf, P. Siligam, C. Simmer, S. Steinke, B. Stevens, K. Wapler, M. Weniger, V. Wulfmeyer, G. Zängl, D. Zhang, and J. Quaas, "Large-eddy simulations over germany using icon: a comprehensive evaluation," *Q. J. R. Meteorol. Soc.*, vol. 143, no. 702, pp. 69–100, 2017.

[2] A. Gassmann and H.-J. Herzog, "Towards a consistent numerical compressible non-hydrostatic model using generalized hamiltonian tools," *Q. J. Roy. Meteor. Soc.*, vol. 134, no. 635, pp. 1597–1613, 2008.

[3] A. Dipankar, B. Stevens, R. Heinze, C. Moseley, G. Zängl, M. Giorgetta, and S. Brdar, "Large eddy simulation using the general circulation model icon," *J. Adv. Model. Earth Syst.*, vol. 7, no. 3, pp. 963–986, 2015.

[4] H. Wan, M. A. Giorgetta, G. Zängl, M. Restelli, D. Majewski, L. Bonaventura, K. Fröhlich, D. Reinert, P. Rípodas, L. Kornblueh, and J. Förstner, "The icon-1.2 hydrostatic atmospheric dynamical core on triangular grids – part 1: Formulation and performance of the baseline version," *Geosci. Model Dev.*, vol. 6, no. 3, pp. 735–763, 2013.

[5] A. Seifert and K. D. Beheng, "A two-moment cloud microphysics parameterization for mixed-phase clouds. part 1: Model description," *Meteorol. Atmos. Phys.*, vol. 92, no. 1, pp. 45–66, 2006.

[6] L. B. Hande, C. Engler, C. Hoose, and I. Tegen, "Parameterizing cloud condensation nuclei concentrations during hope," *Atmos. Chem. Phys.*, vol. 16, no. 18, pp. 12059–12079, 2016.

[7] A. Macke, P. Seifert, H. Baars, C. Barthlott, C. Beekmans, A. Behrendt, B. Bohn, M. Brueck, J. Bühl, S. Crewell, T. Damian, H. Deneke, S. Düsing, A. Foth, P. Di Girolamo, E. Hammann, R. Heinze, A. Hirsikko, J. Kalisch, N. Kalthoff, S. Kinne, M. Kohler, U. Löhnert, B. L. Madhavan, V. Maurer, S. K. Muppa, J. Schween, I. Serikov, H. Siebert, C. Simmer, F. Späth, S. Steinke, K. Träumner, S. Trömel, B. Wehner, A. Wieser, V. Wulfmeyer, and X. Xie, "The hd(cp)^2 observational prototype experiment (hope) – an overview," *Atmos. Chem. Phys.*, vol. 17, no. 7, pp. 4887–4914, 2017.

[8] M. Lebsock and H. Su, "Application of active spaceborne remote sensing for understanding biases between passive cloud water path retrievals," *J. Geophys. Res.-Atmos.*, vol. 119, no. 14, pp. 8962–8979, 2014.

[9] R. Wood and D. L. Hartmann, "Spatial variability of liquid water path in marine low cloud: The importance of mesoscale cellular convection," *J. Climate*, vol. 19, no. 9, pp. 1748–1764, 2006.

[10] R. Wood, "Relationships between optical depth, liquid water path, droplet concentration, and effective radius in adiabatic layer cloud," *University of Washington*, vol. 3, 2006.

[11] V. Ramanathan, R. D. Cess, E. F. Harrison, P. Minnis, B. R. Barkstrom, E. Ahmad, and D. Hartmann, "Cloud-radiative forcing and climate: Results from the earth radiation budget experiment," *Science*, vol. 243, no. 4887, pp. 57–63, 1989.

[12] E. F. Harrison, P. Minnis, B. R. Barkstrom, V. Ramanathan, R. D. Cess, and G. G. Gibson, "Seasonal variation of cloud radiative forcing derived from the earth radiation budget experiment," *J. Geophys. Res.*, vol. 95, no. D11, pp. 18687–18703, 1990.

[13] T. Chen, W. B. Rossow, and Y. Zhang, "Radiative effects of cloud-type variations," *J. Climate*, vol. 13, no. 1, pp. 264–286, 2000.

[14] J. M. Futyan, J. E. Russell, and J. E. Harries, "Cloud radiative forcing in pacific, african, and atlantic tropical convective regions," *J. Climate*, vol. 17, no. 16, pp. 3192–3202, 2004.

[15] N. G. Loeb, B. A. Wielicki, D. R. Doelling, G. L. Smith, D. F. Keyes, S. Kato, N. Manalo-Smith, and T. Wong, "Toward optimal closure of the earth's top-of-atmosphere radiation budget," *J. Climate*, vol. 22, no. 3, pp. 748–766, 2009.

[16] B. Lin, P. Minnis, T.-F. Fan, Y. Hu, and W. Sun, "Radiation characteristics of low and high clouds in different oceanic regions observed by ceres and modis," *Int. J. Remote Sens.*, vol. 31, no. 24, pp. 6473–6492, 2010.

The sub-adiabatic model as a concept for evaluating the representation and radiative effects of low-level clouds in a high-resolution atmospheric model

Vasileios Barlakas[1,a], Hartwig Deneke[1], and Andreas Macke[1]

[1]Leibniz Institute for Tropospheric Research, Leipzig, Germany
[a]now at: Chalmers University of Technology, Gothenburg, Sweden

Correspondence: barlakas@tropos.de

Abstract. The realistic representation of low-level clouds, including their radiative effects, in atmospheric models remains challenging. A sensitivity study is presented to establish a conceptual approach for the evaluation of low-level clouds and their radiative impact in a highly resolved atmospheric model. Considering simulations for six case days, the analysis supports that the properties of clouds more closely match the assumptions of the sub-adiabatic rather than the vertically homogeneous cloud model, suggesting its use as basis for evaluation. For the considered cases, 95.7 % of the variance in cloud optical thickness is explained by the variance in the liquid water path, while the droplet number concentration and the sub-adiabatic fraction contribute only 3.5 % and ~~0.14~~0.2 % to the total variance, respectively. A mean sub-adiabatic fraction of 0.45 is found, which exhibits strong inter-day variability. Applying a principal component analysis and subsequent varimax rotation to the considered set of nine properties, four dominating modes of variability are identified, which explain ~~98~~97.7 % of the total variance. The first and second components correspond to the cloud base and top height, and to liquid water path, optical thickness, and cloud geometrical extent, respectively, while the cloud droplet number concentration and the sub-adiabatic fraction are the strongest contributors to the third and fourth components. Using idealized offline radiative transfer calculations, it is confirmed that the shortwave and longwave cloud radiative effect exhibits little sensitivity to the vertical structure of clouds. This reconfirms, based on an unprecedented large set of highly resolved vertical cloud profiles, that the cloud optical thickness and the cloud top and bottom heights are the main factors dominating the shortwave and longwave radiative effect of clouds, and should be evaluated together with radiative fluxes using observations, to attribute model deficiencies in the radiative fluxes to deficiencies in the representation of clouds. Considering the different representations of cloud microphysical processes in atmospheric models, the analysis has been further extended and the deviations between the radiative impact of the single- and double-moment schemes are assessed. Contrasting the shortwave cloud radiative effect obtained from the double-moment scheme to that of a single moment scheme, differences of about $\sim 40\,\mathrm{W\,m^{-2}}$ and significant scatter are observed. The differences are attributable to a higher cloud albedo resulting from the high values of droplet number concentration in particular in the boundary layer predicted by the double-moment scheme, which reach median values of around $\sim 600\,\mathrm{cm^{-3}}$.

1 Introduction

Clouds play a crucial role in the global energy budget and climate. One important aspect is their strong influence on the shortwave (SW) and longwave (LW) radiation budget. Despite significant progress over the past decades, the relevant processes and resulting climate feedbacks of clouds have not been fully understood, and cannot be reliably represented in climate projections (IPCC, 2013). The representation of boundary layer clouds (i.e., shallow cumulus, stratiform) is particularly problematic (Turner et al., 2007), due to their high spatio-temporal variability. In addition, the coarse resolution of general circulation models ($\sim 100\,\mathrm{km}$) is not sufficient to resolve processes taking ~~placed~~ place at sub-grid scale, nor allows to explicitly take vertical and horizontal heterogeneity into consideration.

Clouds are characterized by complicated three-dimensional (3D) shapes with highly variable macrophysical, microphysical, and radiative properties. Full 3D radiative transfer calculations in complex cloudy atmospheres are computationally expensive and, hence, a number of simplifications are commonly adopted for calculating their radiative effect in atmospheric models. The plane-parallel (PP) approximation is often utilized, which implies that radiative transfer simulations are conducted assuming horizontally homogeneous clouds covering a fraction of the model grid (Di Giuseppe and Tompkins, 2003; Chosson et al., 2007). One particular shortcoming of this assumption is the so-called plane-parallel albedo bias, which refers to the fact that inhomogeneous clouds reflect less solar radiation than otherwise identical homogeneous clouds (Werner et al., 2014). To account for this bias, and to consider horizontal heterogeneities in GCMs, several correction schemes have been developed over the last years, e.g., scaling the liquid water path by a constant reduction factor, renormalization techniques, among others (e.g., Cahalan et al., 1994; Barker, 2000; Cairns et al., 2000; Barker and Räisänen, 2004; Pincus et al., 2003; Shonk and Hogan, 2008).

The optical properties of a cloudy layer are largely determined by two of their physical properties, the liquid water content (q_L) and the effective radius (r_eff) (Slingo, 1989; Collins et al., 2006). The latter is mostly obtained by assuming a fixed droplet ~~number~~ size distribution (Chosson et al., 2007). Double-moment cloud microphysical schemes, which also constrain the effective radius through prognostic equations, are only recently becoming more widespread in use in operational forecasting.

To improve the scientific understanding of clouds and their representation in models, high-quality observations from active (i.e., lidar and cloud radar) and passive (i.e., radiometers) instruments from both ground and space are essential. Currently, such instrumentation is available, i.e., from the Cloudnet program (Illingworth et al., 2007), the A-train constellation (Stephens et al., 2002), the geostationary satellite Meteosat Second Generation (MSG) (Roebeling et al., 2006), while upcoming missions comprise the Earth Cloud Aerosol Radiation Explorer (EarthCARE) satellite mission (Illingworth et al., 2015) and Meteosat Third Generation (MTG) (Stuhlmann et al., 2005). A variety of algorithms have been developed for inferring cloud properties from these observations (e.g., Nakajima and King, 1990; Bennartz, 2007; Roebeling et al., 2013). However, the underlying observational techniques often rely heavily on assumptions about the cloud vertical structure.

High-resolution atmospheric models at cloud-resolving scales are another promising avenue to gain insights into cloud processes and the effects of small-scale cloud variability, and to improve their representation in GCMs. They can resolve relevant processes up to a much smaller scale ($\sim 100\,\mathrm{m}$ for Large Eddy Simulations), and can, thus, serve as basis for developing more

accurate parameterizations. Enabled by the exponential growth in computer power over the past decades, they are increasingly utilized for simulations covering larger domains and longer time periods. In contrast to observations, they also offer the opportunity to assess the interplay of all relevant state variables simultaneously, while instrumental capabilities are generally limited to a small subset, sometimes affected by large measurement uncertainties (Miller et al., 2016).

It is, however, crucial to also critically evaluate the performance of high-resolution ~~atmospheric~~models with observations. Like coarse-resolution models, they include various assumptions and parameterizations, and their shortcomings need to be identified and mitigated. Given the complexity of atmospheric models and the level of detail available from the output of such models, it is, ~~however~~though , often a daunting task to identify the physical reasons for model shortcomings. Inconsistent or even conflicting assumptions made in observation-based products add additional complications to the evaluation of models with observations. Examples for such assumptions include a vertically homogeneous or a sub-adiabatic cloud, which is often made in satellite retrievals (Brenguier et al., 2000; Chosson et al., 2007), or the assumption of a vertically constant cloud droplet number concentration commonly used in ground-based remote sensing of clouds, which is a significant simplification of the profiles available from in situ observations or double-moment cloud microphysical schemes.

In this work, the highly resolved ICON-LEM atmospheric model (ICOsahedral Non-hydrostatic Large-Eddy Model) is employed that was recently developed within the HD(CP)^2 (High Definition Clouds and Precipitation for advancing Climate Prediction) project (Dipankar et al., 2015; Heinze et al., 2017). ~~ICON-LEM provides an unprecedented horizontal resolution of 156, 312, and 625 m covering a large domain over Germany~~. We introduce a conceptual approach for evaluating the representation of low-level clouds in this and other high-resolution atmospheric models, with particular focus on the correct representation of their radiative effect. A sensitivity study is conducted in order to investigate the relevance of the vertical distribution of microphysical properties for their radiative effect, aiming for the identification of suitable column-effective cloud properties for the purpose of model evaluation. The suitability of the sub-adiabatic cloud model is compared to that of the vertically homogeneous cloud model, both of which are commonly used in remote sensing. In addition, differences in cloud radiative properties arising from the availability of the cloud droplet number concentration provided by the double-moment cloud microphysical scheme of Seifert and Beheng (2006) compared to a single-moment scheme are highlighted.

2 Data and methods

2.1 ICON-LEM

The ICON unified modeling framework was co-developed by the German meteorological service (DWD) and the Max Planck institute for meteorology (MPI-M) in order to support climate research and weather forecasting. Within the HD(CP)^2 project, ICON was further extended towards large eddy simulations with realistic topography ~~,~~ and open boundary conditions~~, and a nesting approach with grids varying from 624 to 312 , and 156 resolution~~. This resulted in ICON-LEM ~~(Heinze et al., 2017).~~ deployed in restricted areas that are centered on Germany and the Tropical Atlantic (Heinze et al., 2017). The equations utilized by the model are based on the prognostic variables given by Gassmann and Herzog (2008). Concerning turbulence parameterization, the three-dimensional Smagorinsky scheme is employed (Dipankar et al., 2015). These variables comprise the horizontal

and vertical velocity components, the density of moist air, the virtual potential temperature, and the mass and number densities of traces, e.g., specific humidity, liquid water, and different ice hydrometeors. A comprehensive description of the model and its governing equations are found in Dipankar et al. (2015) and Wan et al. (2013). The activation of cloud condensation nuclei (CCN) is based on the parameterization of Seifert and Beheng (2006) and modified in order to account for the consumption of CCNs due to their activation into cloud droplets. The CCN concentration is then parameterized following the pressure profile and the vertical velocity (Hande et al., 2016).

ICON-LEM utilizes the double-moment mixed-phase bulk microphysical parameterization scheme introduced by Seifert and Beheng (2006). Following their comprehensive description, a generalized gamma distribution is utilized to describe the mass (x_m) of hydrometeors,

$$f(x_\mathrm{m}) = A_\mathrm{m} \cdot x^\nu \cdot \exp\left(-B_\mathrm{m} \cdot x_\mathrm{m}^\xi\right). \quad (1)$$

The coefficients ν, ξ are constants taken from Table 1 in Seifert and Beheng (2006) while the coefficients A_m and B_m are prognostic quantities expressed by the number and mass densities (see Appendix A).

~~The model~~ Simulations are carried out for three different domains with 624 m , 312 m, and 156 m horizontal resolution. The model domains consist of 150 vertical levels, with resolutions ranging from ∼25 m to 70 m within the boundary layer, and from 70 m to 355 m further up until the top of the domain at 21 km. For each of the aforementioned grids, data is stored as one-dimensional (1D) profiles every 10 sec, two-(2D), and 3D snapshots (Heinze et al., 2017).~~yields output on each of the aforementioned grids with the data stored as one-dimensional (1D) profiles, two-(2D), and 3D snapshots~~ . In case of the 3D output, the simulation data is interpolated from the original grids (e.g., 156 m) to a 1 km grid, the 3D coarse data, and 300 m grid, the so-called HOPE data. The latter output has been created for the purpose of model evaluation with ground-based observations from the HD(CP)^2 Observational Prototype Experiment (HOPE) that took place near Jülich (Macke et al., 2017)and is limited to a domain size of about $\sim 45\,\mathrm{km}^2$. Note here that for the 2D and 3D output, data is stored at day- and night-time frequency. Day-time frequency begins at 06:00 UTC and lasts until 00:00 UTC, while night-time starts at midnight and lasts until 06:00 UTC. The 2D data is stored with a day-time and night-time frequency of 10 sec and 5 min, respectively. The 3D coarse data has day-time frequency of 10 min (1 hour at night-time). In this study, the 3D HOPE data has been used that is stored only at a day-time frequency of 15 min.

2.2 RRTMG

For radiative transfer simulations, ICON-LEM employs the rapid radiative transfer model (RRTM) for GCM applications (RRTMG) (Mlawer et al., 1997; Iacono et al., 2008). For the purpose of this investigation, an interface of the RRTMG for use with the Python programming language has been developed, which allows the offline calculation of the radiative fluxes using ICON-LEM outputs as basis.

RRTMG is a fast and accurate broadband radiative transfer model developed by the Atmospheric Environmental Inc. The model employs the correlated-k approach for efficient fluxes and heating rates computations (Mlawer et al., 1997). Molecular absorption information for the k-distributions is taken from the line-by-line radiative transfer model (LBLRTM) (Clough et al.,

2005). Fluxes and heating rates are derived for 14 bands in the SW and 16 bands in the LW. RRTMG considers major absorbing gases, i.e., water vapor, ozone, and carbon dioxide, but also minor absorbing species, i.e., methane, oxygen, nitrogen, and aerosols. Optical properties (optical thickness, single-scattering albedo, and asymmetry parameter) of liquid water clouds are parameterized according to Hu and Stamnes (1993). Note that the RRTMG is a 1D plane-parallel radiative transfer model. For the representation of the sub-grid cloud variability, a Monte Carlo independent column approximation (McICA) method is used (Pincus et al., 2003). Multiple-scattering is considered employing a two-stream algorithm (Oreopoulos and Barker, 2006).

RRTMG provides the SW and LW radiative fluxes for both the upward ($F^{\uparrow}$) and downward ($F^{\downarrow}$) radiation. These two components can be combined to define the net flux (F^{net}),

$$F^{\mathrm{net}} = F^{\downarrow} - F^{\uparrow}. \tag{2}$$

Accordingly, the cloud radiative effect (CRE) is defined as the difference between the cloudy and clear sky net radiative fluxes,

$$\mathrm{CRE} = F^{\mathrm{net}}_{\mathrm{cloudy}} - F^{\mathrm{net}}_{\mathrm{clear}}. \tag{3}$$

The CRE can be computed for the LW, SW, or the net CRE, defined by the sum of the SW and LW radiation.

2.3 Case days

In this study, the 3D HOPE data has been used and a set of 6 days of simulations has been considered, including: 24–25 April 2013, 5 May 2013, 29 July 2014, 14 August 2014, and 3 June 2016. Only a limited subset of variables is stored including the specific humidity, cloud water, ice, rain and snow mixing ratio, wind, vertical velocity, temperature, pressure, cloud cover, and turbulent diffusion coefficient for heat. These days have been selected from the total set of available case days by the presence of suitable liquid water cloud fields and no known bugs in the used model version, which affect the representation of low-level clouds.

2.4 Column selection

In order to investigate the characteristics of liquid water clouds in ICON-LEM, only idealized cloud profiles (i.e., stratiform and cumulus) are considered, corresponding to single-layer non-drizzling clouds. The selection of such cloudy columns has been conducted according to requiring the following threshold criteria:

- For each cloudy layer, a liquid water content of $q_{\mathrm{L}} > 0.01\,\mathrm{g\,m^{-3}}$ and a liquid water path (Q_{L}) larger than $20\,\mathrm{g\,m^{-2}}$.
- No occurrence of rain/drizzle. A rain water path below $0.1\,\mathrm{g\,m^{-2}}$ and $Z_{\mathrm{max}} < -15\,\mathrm{dBZ}$, denoting the maximum radar reflectivity (see Eq. 6) within the cloud profile (Rémillard et al., 2013; Merk et al., 2016).
- A cloud geometrical extent (H) larger than $100\,\mathrm{m}$ (at least two subsequent model layers).
- Clouds located between $300\,\mathrm{m}$ and $4000\,\mathrm{m}$.
- No vertical gaps are allowed.

- Mixed-phase clouds are excluded. The ice water content for the first 4000 m must be zero.
- Superadiabatic clouds have been excluded.

The cloud bottom height (CBH) and cloud top height (CTH) are determined by the bottom and top of the lowermost and uppermost layers for the aforementioned ideal low-level clouds, respectively.

2.5 Cloud property diagnostics

The model ~~provides in the output the~~ outputs the droplet number concentration and liquid water content for each model layer representing the zeroth and the first moments of the mass size distribution (MSD, see Eq. 1). Following Petty and Huang (2011), the mass size distribution is transformed into a droplet size distribution (DSD). For details on the derivation of the moments of DSD and the cloud microphysical properties, the reader is referred to Appendix A.

Following Hansen and Travis (1974), the effective radius, r_{eff}, is defined as the ratio of the third to the second moments of the DSD,

$$r_{\mathrm{eff}} = \frac{1}{2}\frac{\int_0^\infty n(D)(D)^3 \mathrm{d}D}{\int_0^\infty n(D)(D)^2 \mathrm{d}D}. \tag{4}$$

The division by 2 is carried out for diameter-to-radius conversion. The effective radius is linked to the volume-equivalent radius (r_{V}) by the k_2 factor, which depends only on the effective variance (υ) of the droplet size distribution,

$$k_2 = \frac{r_{\mathrm{V}}^3}{r_{\mathrm{eff}}^3} = (1-\upsilon)(1-2\upsilon). \tag{5}$$

For ICON-LEM, the effective variance of the reconstructed Gamma DSD is $\upsilon = 0.052$, corresponding to $k_2 = 0.849$. Typical values of k_2 reported in the literature vary between 0.5 and 1 (e.g., Brenguier et al., 2000; Zeng et al., 2014; Merk et al., 2016). Furthermore, the radar reflectivity is defined as the sixth moment of the size distribution,

$$Z = \int_0^\infty n(D)(D)^6 \mathrm{d}D. \tag{6}$$

Note, that in ICON-LEM, the droplet number concentration varies with height, but the width of the DSD is assumed invariant.

2.6 Cloud models

2.6.1 Vertically homogeneous cloud model

A widely used assumption for passive satellite and ground-based retrievals is the vertically homogenous cloud ~~scheme~~model. Accordingly, a vertically homogeneous DSD is assumed, meaning vertically constant microphysical properties. It follows that the cloud liquid water path is given by,

$$Q_{\mathrm{L}} = \frac{2}{3}\rho_{\mathrm{w}} \cdot \tau \cdot r_{\mathrm{eff}}, \tag{7}$$

describing a positive linear relationship between Q_{L} and both the cloud optical thickness (τ) and effective radius (r_{eff}). Here, ρ_{w} stands for the water density, while the factor $2/3$ is a scale factor resulting from the constant liquid water content and effective radius with height (Lebsock and Su, 2014). Assuming a vertically constant cloud droplet number concentration additionally implies that the cloud geometric extent depends linearly on the cloud water path for a fixed effective radius.

2.6.2 Sub-adiabatic cloud model

The sub-adiabatic cloud ~~scheme~~ model describes the evolution of a convective closed parcel of moist air. According to Albrecht et al. (1990), the liquid water content (q_{L}) of such an air parcel increases linearly with height,

$$q_{\mathrm{L}}(z) = f_{\mathrm{ad}} \cdot \Gamma_{\mathrm{ad}}(T(z), P(z)) \cdot z, \tag{8}$$

where Γ_{ad} is the adiabatic increase of the liquid water content (Bennartz, 2007), z is the height over the cloud base, f_{ad} denotes the sub-adiabatic fraction, T is the temperature, and P is the pressure. f_{ad} describes the deviation from the linear increase with height of q_{L} caused by entrainment of dry air resulting in evaporation and $f_{\mathrm{ad}} < 1$ (sub-adiabaticity). In case of a pure adiabatic cloud, $f_{\mathrm{ad}} = 1$ and Eq. (8) yields to the adiabatic liquid water content ($q_{\mathrm{L,ad}}$). For low-level liquid water clouds, typical values of f_{ad} found in the literature are in the range of 0.3 to 0.9 (Boers et al., 2006). An alternative definition for the liquid water content accounting for the depletion of the liquid water content due to entrainment, precipitation, and freezing drops, is described by,

$$q_{\mathrm{L}} = q_{\mathrm{L,ad}}[1.239 - 0.145 \cdot \ln(z)], \tag{9}$$

following a modified sub-adiabatic profile (Karstens et al., 1994; Foth and Pospichal, 2017). Γ_{ad} depends on temperature (weak function of pressure) following the first law of thermodynamics and the Clausius–Clapeyron relationship. For low-level clouds, ~~its values vary~~ Γ_{ad} varies slightly ($\sim 20\,\%$)~~and for most studiesare~~ . Consequently, in most studies, Γ_{ad} is assumed constant (e.g., Albrecht et al., 1990; Boers et al., 2006) or ~~are~~ it is calculated from cloud bottom temperature and pressure (e.g., Merk et al., 2016) or cloud top information (e.g., Zeng et al., 2014). For this study, an average value of Γ_{ad} between cloud bottom and cloud top has been used.

Integrating the liquid water content between cloud base height and cloud top height, the cloud liquid water path is obtained,

$$Q_{\mathrm{L}} = \int_{\mathrm{CBH}}^{\mathrm{CTH}} q_{\mathrm{L}}\,(z)\,\mathrm{d}z = \frac{1}{2} f_{\mathrm{ad}} \cdot \Gamma_{\mathrm{ad}} \cdot H^2. \tag{10}$$

Hereby, H denotes the cloud geometrical extent. ~~Note that the ratio of the~~ Compared to Eq. (7), Eq. (10) leads to a factor of $5/9$, meaning that the sub-adiabatic liquid water path ~~to the equivalent vertically homogeneous one yields a factor of~~ is $5/6$ times the one of the vertically homogeneous model (Wood and Hartmann, 2006). Dividing Q_{L} by its adiabatic value (inserting $f_{\mathrm{ad}} = 1$ into Eq. 10), the sub-adiabatic fraction can be computed,

$$f_{\mathrm{ad}} = \frac{Q_{\mathrm{L}}}{Q_{\mathrm{L,ad}}}. \tag{11}$$

For low-level liquid water clouds, the droplet number concentration (N_d) depends on the availability of cloud condensation nuclei (CCN) that could get activated at cloud base (Bennartz, 2007). Considering the adiabatic increase of the liquid water content, it follows that at any given height, q_L is distributed over the activated CCN (per unit volume). Consequently, there is no dependency of the mean volume radius r_V on the shape of the droplet size distribution, but only on N_d and q_L,

$$r_\mathrm{V} = \left(\frac{3 q_\mathrm{L}}{4\pi \cdot \rho_\mathrm{w} \cdot N_\mathrm{d}} \right)^{\frac{1}{3}}. \tag{12}$$

Combining Eqs. ~~5 and 12~~(5) and (12), the effective radius for the uppermost cloud layer can be written in terms of the liquid water path, the droplet number concentration, and the adiabatic fraction,

$$r_\mathrm{eff}(Q_L, f_\mathrm{ad}, N_d) = (18 f_\mathrm{ad} \cdot \Gamma_\mathrm{ad} \cdot Q_\mathrm{L})^{\frac{1}{6}} (4\pi \rho_w \cdot k_2 \cdot N_d)^{-\frac{1}{3}}. \tag{13}$$

In the geometric optics regime, the extinction coefficient, b_ext, can be written as a function of the liquid water content and the effective radius. Consequently, the cloud optical thickness can be computed by integrating b_ext over the cloud geometrical extent, i.e., from cloud base height to cloud top height,

$$\tau = \int_\mathrm{CBH}^\mathrm{CTH} b_\mathrm{ext}(z)\,\mathrm{d}z = \int_\mathrm{CBH}^\mathrm{CTH} \frac{3}{2\rho_\mathrm{w}} \frac{q_\mathrm{L}(z)}{r_\mathrm{eff}(z)} \mathrm{d}z. \tag{14}$$

For vertically constant q_L and r_eff, this can be interpreted as the cloud optical thickness coming from the vertical homogeneous model (see Eq. 7). According to the sub-adiabatic cloud model, the cloud optical thickness is linked to the liquid water path and the effective radius (Wood, 2006),

$$\tau = \frac{9}{5} \frac{Q_\mathrm{L}}{\rho_\mathrm{w} \cdot r_\mathrm{eff}} \tag{15}$$

Alternatively, substituting r_eff from Eq. (13) in Eq. (~~14~~15), the cloud optical thickness is given by,

$$\tau(Q_\mathrm{L}, f_\mathrm{ad}, N_\mathrm{d}) = \frac{9}{5} (4\pi k_2 \cdot N_\mathrm{d})^{\frac{1}{3}} \left(18 \rho_\mathrm{w}^4 \cdot f_\mathrm{ad} \cdot \Gamma_\mathrm{ad}\right)^{-\frac{1}{6}} Q_\mathrm{L}^{\frac{5}{6}}. \tag{16}$$

$$\tau(Q_\mathrm{L}, f_\mathrm{ad}, N_\mathrm{d}) = \frac{9}{5} (4\pi k_2 \cdot N_\mathrm{d})^{\frac{1}{3}} \left(18 \rho_\mathrm{w}^4 \cdot f_\mathrm{ad} \cdot \Gamma_\mathrm{ad}\right)^{\frac{1}{6}} Q_\mathrm{L}^{\frac{5}{6}}.$$

3 Cloud characteristics

3.1 General features

Table 1 lists the statistics of the cloud properties for all the case days individually and on average as simulated ~~from~~ by ICON-LEM, while Fig. 1 illustrates the corresponding histograms~~in case of 3 June 2016 and the average over all days. Throughout this study, a special emphasis is given on 3 June 2016 cause it approximates best the mean properties over all the case days considered.~~ for the latter case only. Note that for the droplet number concentration and the effective radius, results are presented as follows:

Table 1. Statistics of cloud properties of low-level clouds for all the case days individually and on average as simulated by ICON-LEM. n stands for the sample size. For the fraction of clouds two values are presented: values in brackets denote the fraction of selected clouds (FC) according to the column selection (see Sect. 2.4), while values outside brackets stand for the actual cloud fraction (CF) in terms of the following threshold for the liquid water path, $Q_{\mathrm{L}} > 1\,\mathrm{g\,m^{-2}}$.

Days	n [-]	Q_{L} [$\mathrm{g\,m^{-2}}$]	τ [-]	CBH [m]	CTH [m]	H [m]	N_{int} [$\mathrm{cm^{-3}}$]	r_{int} [μm]	f_{ad} [-]	CF (FC) [%]
24 April 2013	5822	41.9 ± 20.7	14.9 ± 6.38	641 ± 163	907 ± 166	266 ± 55.7	686 ± 164	4.1 ± 0.4	0.59 ± 0.19	1.75 (0.36)
25 April 2013	29543	159.1 ± 65.5	37.4 ± 43.8	1721 ± 285	2262 ± 323	541 ± 273	380 ± 154	5.5 ± 1.1	0.47 ± 0.21	5.18 (1.83)
5 May 2013	9465	60.2 ± 48.8	20.0 ± 12.7	1238 ± 279	1630 ± 334	391 ± 127	576 ± 187	4.2 ± 0.6	0.46 ± 0.19	2.57 (0.59)
29 July 2014	48661	156.3 ± 236.3	39.3 ± 48.8	1063 ± 601	1599 ± 662	535 ± 303	464 ± 195	5.2 ± 1.2	0.40 ± 0.19	7.92 (3.02)
14 August 2014	35105	114.3 ± 192.7	32.1 ± 41.8	779 ± 533	1214 ± 625	435 ± 248	612 ± 229	4.6 ± 1.0	0.48 ± 0.19	5.79 (2.18)
3 June 2016	32768	116.0 ± 152.0	28.6 ± 33.0	1361 ± 874	1851 ± 926	491 ± 241	388 ± 262	5.7 ± 1.4	0.45 ± 0.21	17.2 (2.04)
All days	161364	129.7 ± 199.8	33.2 ± 41.5	1177 ± 675	1644 ± 746	487 ± 268	480 ± 232	5.1 ± 1.2	0.45 ± 0.21	6.73 (1.67)

– droplet number concentration weighted over the cloud geometrical extent, given by,

$$N_{\mathrm{int}} = \frac{1}{H} \int_{\mathrm{CBH}}^{\mathrm{CTH}} N_{\mathrm{d}}(z) \cdot \mathrm{d}z, \tag{17}$$

– effective radius weighted over the extinction coefficient at each layer,

$$r_{\mathrm{int}} = \frac{1}{\tau} \int_{\mathrm{CTH}}^{\mathrm{CBH}} b_{\mathrm{ext}}(z) \cdot r_{\mathrm{eff}}(z) \cdot \mathrm{d}z. \tag{18}$$

~~Statistics of cloud properties of low-level clouds for all the case days individually and on average as simulated from ICON-LEM. For the fraction of clouds two values are presented: values in brackets denote the fraction of selected clouds (FC) according to the column selection (see Sect. 2.4), while values outside brackets stand for the actual cloud fraction (CF) in terms of the following threshold for the liquid water path, $Q_{\mathrm{L}} > 1$.~~ It can be shown that the latter equation reduces to Eq. (7), which implies that the calculated effective radius corresponds to that of a vertically homogeneous cloud with identical liquid water path and optical thickness. The different cloud properties are characterized by a large variability from day to day, but even within the same day driven by entrainment processes. In addition, the differences are also subject to the sample size (n) for each day depending on the column selection filter that applied to ICON-LEM output. Recall here that a cloudy column is taken under consideration when $q_{\mathrm{L}} > 0.01\,\mathrm{g\,m^{-3}}$ for each cloud model level while the liquid water path for the entire column should be larger than $20\,\mathrm{g\,m^{-2}}$. Subsequently, the fraction of clouds (FC) selected in this study is quite low ($\mathrm{FC} < 3\,\%$). Alternatively, if only a liquid water path filter is applied to the data, defining as cloudy the columns with Q_{L} larger than $1\,\mathrm{g\,m^{-2}}$, the actual cloud fraction (CF) is obtained. The rather large value of the CF found for 3 June 2016 is associated with very low (with $100 < \mathrm{CBH} < 200\,\mathrm{m}$) overcast cloudy conditions in the early hours.

Looking at the mean histograms of CTH and CBH, one can identify multimodal distributions. Note here that, in this study, all ~~the~~ low-level clouds are considered (i.e., cumuli-like, stratiform) increasing the variability of the different properties.

The double-moment microphysical scheme adopted in ICON-LEM is reflected on the histograms of the droplet number concentration. The mean ~~distribution~~ histogram of N_{int} for all the case days on average suggests a bimodal distribution with peaks centered around $200\,\mathrm{cm}^{-3}$ and $450\,\mathrm{cm}^{-3}$. ~~For~~ These two modes are clearly found for 29 July 2014, 14 August 2014, and 3 June 2016. Especially, for 3 June 2016, the peak around $200\,\mathrm{cm}^{-3}$ is even more notable (not shown here). Note here that this value is close to the fixed droplet number concentration profile suggested by single-moment microphysical schemes adopted by atmospheric models~~(~~, such as ECHAM ~~)~~(Giorgetta et al., 2013) and ICON-NWP, which is the global Numerical Weather Prediction (NWP) version of the ICON model (Heinze et al., 2017). For 5 May 2013, the corresponding histrogram is characterized by a right-skewed distribution, with a rather long tail towards large values of N_{int} and a very small peak that appears around $800\,\mathrm{cm}^{-3}$. On the contrary, for ~~the~~ 24–25 April 2013, ~~only a single mode is clearly identified~~ the distributions of N_{int} are described by skewed distributions (not shown here) ~~, with a peak towards large N_{d} values for the~~ with well-defined single peaks. For the 24^{th} ~~and small values for the~~ , the peak veers towards large N_{int} values (left-skewed), while, for the 25^{th} the peak is located at small N_{int} values (right-skewed), which are centered around $686\,\mathrm{cm}^{-3}$ and $380\,\mathrm{cm}^{-3}$, respectively. A close relation between the effective radius and the droplet number concentration ~~exist~~exists. On average, the larger the N_{int} the smaller the r_{int}.

3.2 Vertical variability

Figure 2 shows a box-whisker plot of the droplet number concentration for ~~3 June 2016~~all the case days on average, describing the histograms of N_{d} simulated for different model levels by the double moment scheme of ICON-LEM. For comparison, the red line shows the climatology-based droplet number concentration profile adopted by ECHAM (Giorgetta et al., 2013). While above $2\,\mathrm{km}$ altitude, the modeled values match the climatology well, much larger median values up to $600\,\mathrm{cm}^{-3}$ are found in the boundary layer. Compared to satellite estimates of N_{d}, these values seem ~~excessively~~ rather high (Quaas et al., 2006; Grosvenor et al., 2018). ~~Furthermore~~On the contrary, in situ observations suggest higher values of N_{d} and, accordingly, closer to those simulated by ICON-LEM~~, but are affected by large instrumental uncertainties (Grosvenor et al., 2018)~~. Hence, efforts should be undertaken to further validate the cloud droplet number concentrations predicted by the double-moment scheme.

Figure 3 depicts the mean profiles of q_{L} and N_{d} normalized over the cloud geometrical extent (from CBH to CTH) for ~~3 June 2016.~~ all the case days on average. The ICON-LEM simulated liquid water profile follows a linear increase from cloud bottom to around ~~60~~50–60 % of the cloud height in agreement with the adiabatic cloud model. Thereafter, the liquid water content decreases towards the cloud top due to evaporation induced by entrainment of dry air mass from cloud top. Furthermore, the mean profile of the droplet number concentration is found roughly constant at verticals depths between ~~20 and 75~~30 and 70 % of H (~~$\sim$ 400~~$\sim$ 480 cm^{-3}) and decreases towards the cloud top at values ~~$\sim$ 150~~$\sim$ 100 cm^{-3} characterized by a large variability.

3.3 Adiabaticity of liquid water clouds

Following the sub-adiabatic cloud model, higher values of the liquid water path are linked with geometrically thicker clouds (see Eq. 10). For all the days, the distribution of the cloud geometrical extent follows a similar pattern, except for 24 April 2013 and 5 May 2013. For the latter two days, only optically thinner clouds are simulated as compared to the rest days, with τ

values of 14.9 and 20, respectively. However, this could also be subject to the very small sample size as compared to the other simulated days. The highest mean value of the sub-adiabatic fraction is found for ~~the~~ 24 April 2013, whereby only optically and geometrically thin clouds are simulated located at the lowermost altitudes (mean CTH of 907 m). One could expect the same findings for ~~the~~ 5 May 2013, but the smaller values of f_{ad} are partly associated with the higher values of H together with their vertical location where entrainment processes can be more pronounced. The lowest mean values of f_{ad} are found for 29 July 2014 reflected by the high frequency of occurrence of larger values of the cloud geometrical extent. Overall, the statistics of f_{ad} for the six days under investigation (161364 liquid water cloudy columns) over Germany introduces a mean value of about $f_{\mathrm{ad}} = 0.45$ (see Table 1) while the interquartile range (IQR) is [0.29, 0.59]. There is a wide range of values of f_{ad} from nearly 0 to 1. The latter is in agreement with the findings of Boers et al. (2006); Merk et al. (2016). Especially, Merk et al. (2016) derived the f_{ad} from ground-based observations over Germany and reported a mean value of 0.45 for the period 2012–2015, with a IQR of [0.29, 0.61]; Boers et al. (2006) reported f_{ad} values within [0.3, 0.9].

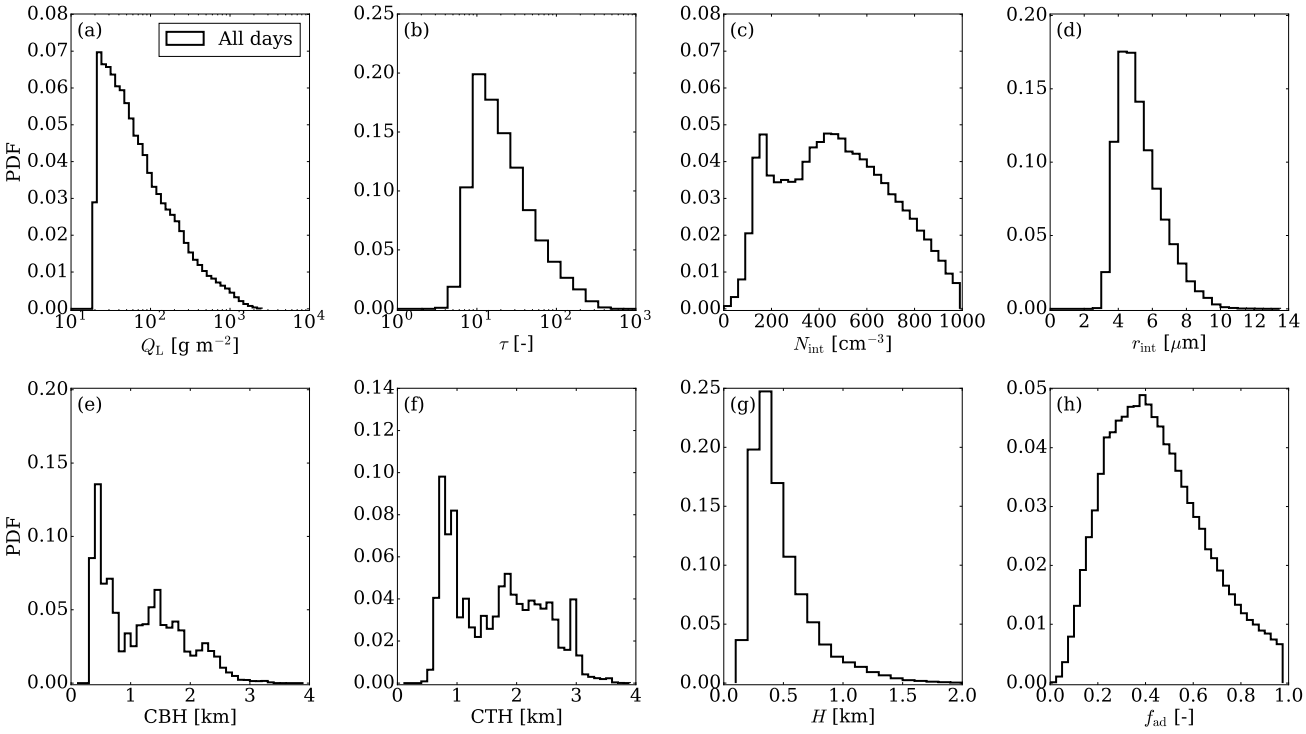

Figure 1. Histograms of cloud properties ~~of low-level clouds in case of 3 June 2016 (red) and on average~~ for all the case days ~~(green)~~ on average as simulated ~~from~~ by ICON-LEM: (a) Q_{L}, (b) τ, (c) N_{int}, (d) r_{int}, (e) CBH, (f) CTH, (g) H, and f_{ad}.

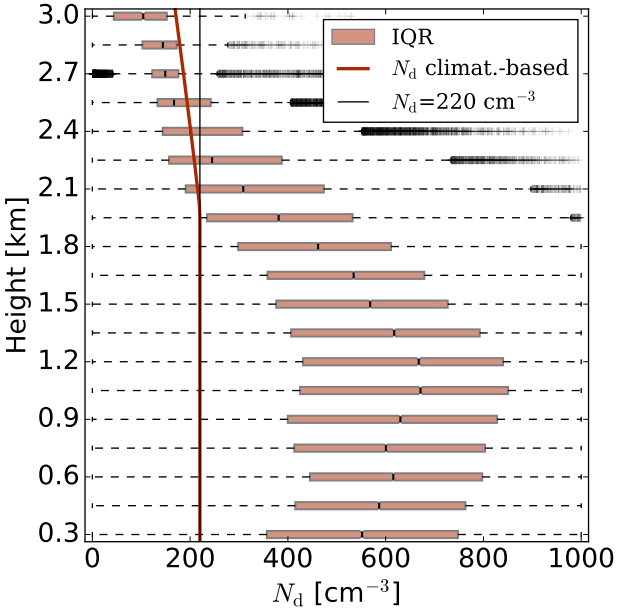

Figure 2. Box-whisker plot of the droplet number concentration for ~~3 June 2016~~all the case days on average, describing the histograms of N_d simulated for different model levels by the double moment scheme of ICON-LEM. Boxes illustrate interquartile range (IQR), dark red line denotes the climatology-based N_d profile adopted by ECHAM, and the thin black line demonstrates the constant N_d profile of 220 cm^{-3}.

Table 2. ~~Ordinary~~ Prediction of cloud optical thickness by an ordinary least squares regression ~~results~~method: Regressor coefficients (a), Y-intercept (a_0), squared correlations (R^2), and ~~root-mean-square~~ root mean square error (RMSE). Theoretical (Th.) values according to the sub-adiabatic model are also included.

$Y = a_0 + a_1 \cdot x_1 + ... + a_n \cdot x_n$						
Y	a_0	$a_1 \cdot \ln(Q_L)$	$a_2 \cdot \ln(f_{ad})$	$a_3 \cdot \ln(N_{int})$	R^2	RMSE
Y_1	-0.557 ± 0.0020	0.849 ± 0.0004	-	-	0.957	0.175
Y_2	-2.037 ± 0.0019	0.808 ± 0.0002	-	0.274 ± 0.0003	0.992	0.075
Y_3	-0.665 ± 0.0024	0.860 ± 0.0005	~~0.065 ± 0.0009~~ -0.065 ± 0.0009	-	0.959	0.172
Y_4	-2.437 ± 0.0008	0.830 ± 0.0001	~~0.147 ± 0.0001~~ -0.147 ± 0.0001	0.303 ± 0.0001	0.999	0.027
Th.	-	$a_1 = 0.833$	~~$a_2 = 0.167$~~ $a_2 = -0.167$	$a_3 = 0.333$	-	-

3.3.1 Cloud optical thickness

One of the fundamental cloud properties describing the SW radiative effect is the cloud optical thickness. ~~Thus~~In this section, we focus on its derivation and its dependencies.

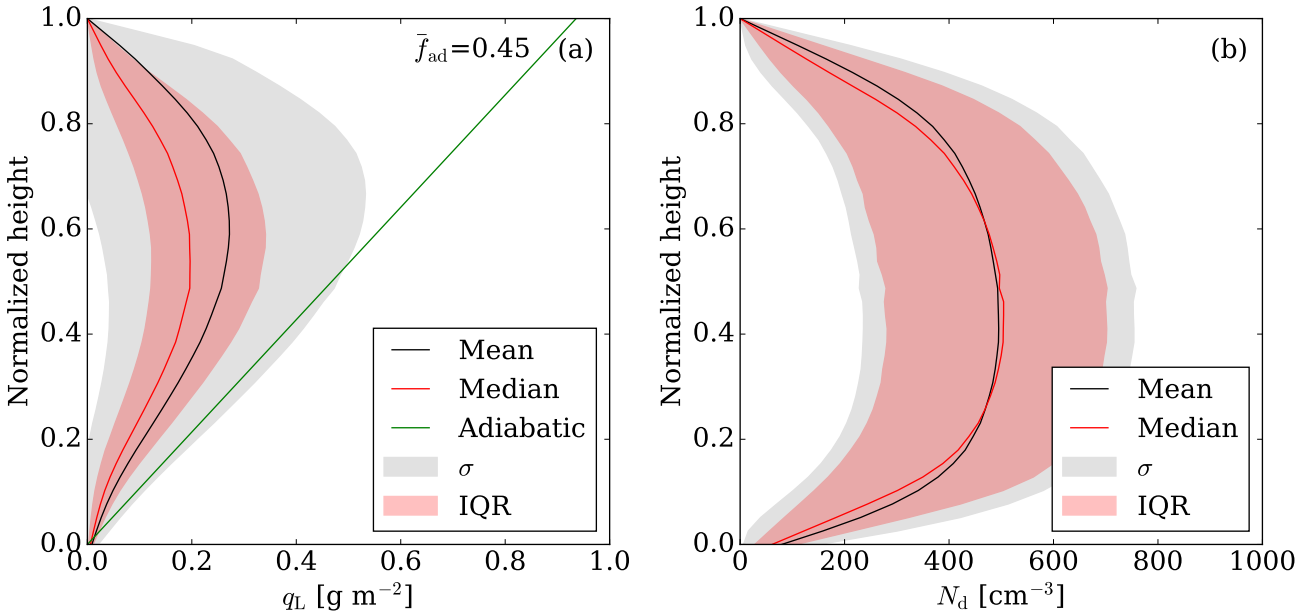

Figure 3. ICON-LEM simulated mean (a) $q_{\rm L}$ and (b) $N_{\rm d}$ profiles for ~~3 June 2016.~~ all the case days on average. Profiles are normalized over height from the CBH to the CTH. Black lines denote the mean, red solid lines the median, gray shaded areas the standard deviation, red shaded areas the interquartile range (IQR), and the green solid line outline the mean adiabatic $q_{\rm L}$ profile characterized by a mean adiabatic fraction ($\bar{f}_{\rm ad}$) of 0.45.

With this intention, an effort has been conducted to predict the cloud optical thickness derived from Eq. (14) by employing the sub-adiabatic model and Eq. (16). On a logarithmic scale, Eq. (16) suggests that τ is a linear function of $Q_{\rm L}$, $f_{\rm ad}$, and $N_{\rm d}$ and it can be seen as a linear regression model. Here, the droplet number concentration weighted over the cloud geometrical extent ($N_{\rm int}$) is used. An advantage of the logarithmic scale is that the variance of the cloud optical thickness can be decomposed into the contributions from each of the regressors ($Q_{\rm L}$, $f_{\rm ad}$, and $N_{\rm int}$). This enables us to attribute the relative importance of the regressors in explaining the variance in τ. In our framework, we employed the ordinary least squares (OLS) regression method. This method finds the projection direction for which $Q_{\rm L}$, $f_{\rm ad}$, and $N_{\rm int}$ are maximally correlated with τ and provides the values of the coefficients that minimize the error in the prediction of τ. Results are compiled in Table 2.

Firstly, we focus on the relative importance of $Q_{\rm L}$ in τ. Model $Y_1(Q_{\rm L})$ suggests that the liquid water path explains 95.7 % of the variance in cloud optical thickness and they follow an excellent linear relationship ~~(see Fig. ?? in Appendix B)~~ with a $5/6$ ~~fit ($\alpha = 0.8489$~~slope ($\alpha = 0.849$) and a root mean square error (RMSE) of ~~0.1751~~0.175. In agreement with the sub-adiabatic model, τ is proportional to $Q_{\rm L}^{5/6}$ and not to $Q_{\rm L}$ as suggested by the vertically homogeneous model; otherwise, a value of $\alpha = 1$ would be expected. Comparing the models $Y_2(Q_{\rm L}, N_{\rm int})$ and $Y_3(Q_{\rm L}, f_{\rm ad})$, Y_2 has a higher R^2 value (~~0.9921 compared to~~

0.9585 0.992 compared to 0.959), a lower RMSE (0.0750 compared to 0.17230.075 compared to 0.172), while the regression coefficients are much closer to the sub-adiabatic theory.

All in all, the liquid water path is able to explain 95.7195.7 % of the variance in cloud optical thickness, while the droplet number concentration and the sub-adiabatic fraction additionally contribute 3.5 % and 0.1402 % to the variance, respectively.

Variability caused by $\Gamma_{\rm ad}$ is insignificant and, thus, is not shown here. This is confirmed by model $Y_4(Q_{\rm L}, f_{\rm ad}, N_{\rm int})$, which, even though it excludes $\Gamma_{\rm ad}$, explains 99.9 % of the variance in cloud optical thickness. In fact, model $Y_4(Q_{\rm L}, f_{\rm ad}, N_{\rm int})$ supports the applicability of the sub-adiabatic model since it is able to approximate the cloud optical thickness with high accuracy (RMSE = 0.027).

4 Principal component analysis

Pearson correlations between the logarithm of the cloud properties and the principal (PC) and rotational components (RC). Degree of correlation (absolute values): (a) very weak: below 0.2, (b) weak: 0.2, 0.4), (c) moderate: 0.40, 0.6), (d) strong: 0.6, 0.8), and (e) very strong 0.8, 1.0. CBH 0.78 0.97 −0.53 0.03 −0.08 0.00 −0.25 0.20 CTH 0.92 0.92 −0.29 −0.28 0.07 0.08 −0.20 0.24 $\Gamma_{\rm ad}$ −0.74 −0.90 0.49 −0.01 0.16 0.07 0.27 −0.18 τ 0.45 −0.06 0.89 −0.97 0.06 −0.19 −0.09 −0.12 $Q_{\rm L}$ 0.59 0.04 0.81 −0.97 0.00 −0.24 0.02 0.05 H 0.66 0.18 0.57 −0.94 0.48 0.29 −0.01 0.09 $f_{\rm ad}$ 0.10 −0.10 0.34 −0.10 −0.94 −0.99 0.00 −0.03 $N_{\rm int}$ −0.53 −0.52 0.70 −0.25 −0.12 −0.24 −0.45 −0.78 $r_{\rm int}$ 0.86 0.38 0.16 −0.54 −0.22 −0.31 0.43 0.68

To identify the minimum set of parameters for the representation of low-level clouds towards the computation of the CREs, the dominating modes of variability among the different cloud properties have been investigated. Cloud properties from all the case days have been considered. $\Gamma_{\rm ad}$ is not a cloud property, but since it is considered by the sub-adiabatic model, we decided to include it in the analysis. Towards this direction, one should first map the correlation of the different properties. Figure 4 identifies groups of variables that tend to covary together. The first group comprises τ, $Q_{\rm L}$, and H that are strongly positively correlated with one another ($R^2 > 0.83$Pearson > 0.837), while in the second group, CTH, CBH are positively correlated ($R^2 > 0.93$Pearson > 0.934) albeit inversely correlated with $\Gamma_{\rm ad}$ ($R^2 < -0.88$Pearson < -0.85). Alternatively, these two groups could be partly noted as the SW and LW (excluding $\Gamma_{\rm ad}$) properties, respectively. Last but not least, only a weak to mediocre correlation was found between $r_{\rm int}$, $N_{\rm int}$, $f_{\rm ad}$ and the other properties.

A principal component analysis (PCA) is and a subsequent varimax rotation (hereafter rotational component analysis) are applied to reveal systematic co-variations among the cloud properties, reducing the degrees of freedom, while preserving the maximum amount of information towards redundancy. This analysis has been conducted by employing the logarithm of the properties. Since our aim is to retain as few degrees of freedom as possible, the first step is to estimate the optimized optimal number of components needed. As a primary solution, we used the same number of components as the original variables (nine in number) and we estimated the fraction of variance explained by each component. Figure ?? Table 3 illustrates the resulting cumulative explained variance as a function of each principal component (PCrotational component (RC). The cumulative explained variance suggests the use of four PCs in the logarithmic space (98RCs (97.7 %), going from a nine-dimensional space to a four-dimensional space; the variance contributed by the fifth component is bellow 1.872.1 %. The interpretation of the

Table 3. Explained variance and cumulative explained variance by different components obtained from the rotational component analysis (RC).

	RC-1	RC-2	RC-3	RC-4	RC-5	RC-6	RC-7	RC-8	RC-9
Explained variance (%)	33.8	35.5	14.8	13.6	2.10	0.10	0.10	0.00	0.00
Cumulative proportion (%)	33.8	69.3	84.1	97.7	99.8	99.9	100	100	100

principal components (not shown here) is based on finding which properties are ~~mostly strong~~ correlated with each ~~component. Table 4 summarizes the quality of reduction in the squared correlations (Pearson)by comparing the residual correlations (PCs) to the logarithm of the original cloud properties~~principal component (PC). However, ~~the~~ PCs are hard to interpret~~since, although~~ . Although each new dimension is clearly dominated by some . of the cloud properties, ~~they~~ the PCs are found moderately or strongly correlated with other properties. ~~For example, PC-2, which explains 33.4 of the total variance, is driven by τ, $Q_{\rm L}$, $N_{\rm int}$, and H and is substantially correlated with CBH and $\Gamma_{\rm ad}$.~~

~~Subsequently, the so-called varimax rotation has been utilized in order to associate~~ However, the rotational component analysis associates each cloud property to at most one ~~principal component~~ rotational component (RC) by maximizing the sum of the variances of the squared correlations between the cloud properties and the PCs (Stegmann et al., 2006). ~~This results in the rotational components~~

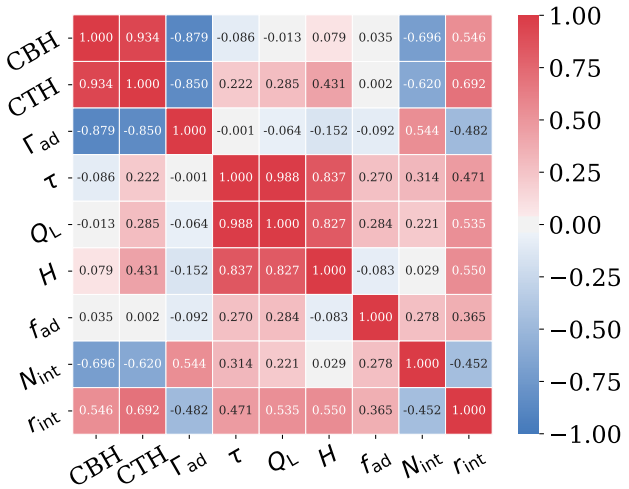

Figure 4. Correlation plot between all the properties (CBH, CTH, $\Gamma_{\rm ad}$, τ, $Q_{\rm L}$, H, $f_{\rm ad}$, $N_{\rm int}$, and $r_{\rm int}$). The colorbar indicates the values of the corresponding Pearson correlations.

Table 4 summarizes the quality of reduction in Pearson correlations by comparing the residual correlations (RCs) ~~. RCs are also compiled in Table 4. Under those circumstances, the resulting squared~~ to the logarithm of the original cloud properties. These correlations are either close to unity or zero, allowing only a few moderate correlations and pointing to how each cloud property loads on each component~~, while preserving the overall number of components (see Fig. ??). Please note the differences between PCs and RCs.~~ Table 3). RC-2, responsible for ~~36~~35.5 % of the ~~variance in logarithmic space~~total variance, is strongly correlated with three of the original variables~~.~~, i.e., τ, $Q_{\rm L}$, and H, with Pearson correlations of -0.971, -0.968, and -0.937, repsectively. Considering the strong correlation found between τ and $Q_{\rm L}$ (see Fig. 4) and their robust linear relation (~~$R^2 = 0.99$~~Pearson $= 0.988$), they can be considered interchangeable. In the same direction are the findings for RC-1 and CBH (Pearson $= 0.969$), CTH (Pearson $= 0.919$), ~~CTH,~~ and $\Gamma_{\rm ad}$ (Pearson $= -0.896$), with an explained variance of about ~~34~~33.8 %. ~~The~~ RC-3 and RC-4 are clearly a function of $f_{\rm ad}$ (Pearson $= -0.995$) and $N_{\rm int}$ (Pearson $= -0.778$), respectively. They explain 14.8 % and 13.6 % of the total variance (see Table 4), ~~respectively,~~ pointing to two clear degrees of freedom. Effective radius is the only property that shows a moderate or strong importance in more than one RCs, namely ~~RC-1, RC-3,~~ RC-2, and RC-4~~. $r_{\rm int}$~~ , but it could be substituted as a degree of freedom from a well defined DSD, with $N_{\rm int}$ as a primary component and k_2. Note here that the first two components account for more than ~~69~~69.3 ~~% (in logarithmic scale)~~ % of the variance of the cloud properties with the first component related to those that dominate in the SW CRE while, the second component, with those that are of great importance in the LW CRE.

The aforementioned analysis points to the reduced set of parameters for the representation of low-level clouds towards the computation of the CREs: $N_{\rm int}$, $Q_{\rm L}$, $f_{\rm ad}$, H, and one of the CTH or CBH.

~~Correlation plot between all the properties (CBH, CTH, $\Gamma_{\rm ad}$, τ, $Q_{\rm L}$, H, $f_{\rm ad}$, $N_{\rm int}$, and $r_{\rm int}$). Explained variance by different components for both the principal component analysis (PC) and the rotational component analysis (RC).~~

Table 4. Pearson correlations between the logarithm of the cloud properties and the rotational components (RC). Degree of correlation (absolute values): (a) very weak: below 0.2, (b) weak: [0.2, 0.4), (c) moderate: [0.4, 0.6), (d) strong: [0.6, 0.8), and (e) very strong [0.8, 1.0].

Properties	RC-1	RC-2	RC-3	RC-4
CBH	0.969	0.025	−0.001	0.201
CTH	0.919	−0.282	0.076	0.237
$\Gamma_{\rm ad}$	−0.896	−0.014	0.073	−0.183
τ	−0.062	−0.971	−0.192	−0.125
$Q_{\rm L}$	0.036	−0.968	−0.240	0.052
H	0.177	−0.937	0.285	0.094
$f_{\rm ad}$	−0.010	−0.099	−0.995	−0.025
$N_{\rm int}$	−0.518	−0.250	−0.244	−0.778
$r_{\rm int}$	0.382	−0.536	−0.314	0.681

5 Cloud radiative effects of low-level clouds

5.1 Radiative transfer simulations

The input for the radiative transfer simulations was constructed on the basis of ICON-LEM. In other words, temperature, pressure, and water vapour profiles, surface temperature and pressure, and ~~the cloud 's~~ cloud liquid water content and droplet number concentration are taken from the high-resolution model. For ozone, the profile of the US standard atmosphere is adopted (Anderson et al., 1986). Note here that ~~the~~ ICON-LEM profiles reach approximately ~~20~~21 km altitude. ~~We~~ Hence, we further extended the atmosphere up to 120 km height ~~again using~~ according to the US standard atmosphere. ~~The carbon dioxide concentration was set to~~ Considering the focus of this study the effects of aerosols are neglected and a maximum cloud overlap of cloudy layers is assumed, since only idealized single-layer water clouds are considered. Table 5 compiles the rest input parameters for the radiative transfer simulations that are not adopted by ICON-LEM. ~~.and near-infrared (0.3) band and the cosine of the solar zenith angle (0.7); the effects of Last but not least, maximum overlap of cloudy layers is assumed, since only idealized single-layer liquid water clouds are considered for this study.. Simulations have been conducted only for one day, 3 June 2016. Considering the focus of this work, the following assumptions have been made: constant values for the direct and a diffuse SW~~

5.1.1 Simulated scenarios

In order to estimate the effects of the bulk microphysical parameterizations and the vertical stratification of the cloud properties on the CREs, the double-moment scheme (ICON-LEM; hereafter reference simulation, Ref.) is confronted against the following scenarios: S1, single-moment scheme, whereby the droplet number concentration follows a fixed profile that varies according to pressure profile (P), sharing the same liquid water content profiles as in Ref.,

$$N_{\mathrm{d}}(P) = N_{\mathrm{d},1} + (N_{\mathrm{d},2} - N_{\mathrm{d},1}) \cdot \mathrm{e}^{f(P)}, \tag{19}$$

with,

$$f(P) = \min(8, P_{\mathrm{b}}/P)^2. \tag{20}$$

Table 5. Input parameters for the RRTMG model.

Parameter	Value
Cosine of solar zenith angle	0.70
Carbon dioxide concentration	399 ppm
Ultraviolet/Visible surface albedo for direct radiation	0.05
Ultraviolet/Visible surface albedo for ~~the ultraviolet/visible (~~diffuse radiation	0.05
Near-infrared surface albedo for direct radiation	0.30
Near-infrared surface albedo for diffuse radiation	0.30

Here, $N_{d,2}$ is the droplet number concentration in the boundary layer, $N_{d,1} = 50\,cm^{-3}$ denotes the corresponding value in the free troposphere, and P_b is the boundary layer height (800 hPa) (Giorgetta et al., 2013). ~~Three~~ Two different scenarios are considered, where the liquid water path ~~in preserved , but redistributed within the profile.~~ is preserved within the vertical profile, but redistributed: In S2, a constant liquid water content profile is used with a fixed droplet number concentration representing the vertically homogeneous cloud model ~~. Scenario~~ and scenario S3 denotes the equivalent sub-adiabatic profile. Finally, ~~following Karstens et al. (1994), Foth and Pospichal (2017), a modified sub-adiabatic profile is considered in~~ scenario S4 ~~accounting for entrainment processes~~employs the mean vertical profile of N_d over all case days (see Fig. 2). For scenarios ~~S1–S4, four~~ S1–S3, three individual simulations have been conducted according to the following droplet number concentration~~profile:~~:

- N_d following the climatology of ~~coarse atmospheric models (e.g., ECHAM, Giorgetta et al., 2013),~~ ECHAM, $220\,cm^{-3}$.
- N_d weighted over H, N_{int}.
- ~~$N_d = 388$~~$N_d = 480\,cm^{-3}$, employing the mean N_{int} ~~for 3 June 2016.~~
- ~~N_d defined according to the two major clusters in the histogram of N_d for 3 June 2016 (see Fig 1). If N_{int} is below 388 , a value of 217 is used, while, if N_{int} is larger than 388 , a value of 686 is used defined as the mean values over the two clusters, respectively~~over all case days.

Note here that all scenarios share the same Q_L and k_2 parameter. The different scenarios are summarized in Table 6.

5.1.2 Modelled CREs

For the reference run, the mean and the standard deviation of the modeled CREs for the SW, LW, and NET (SW+LW) radiation are summarized in Table 7. The atmospheric cloud radiative effect (ATM) defined as the difference between CREs at the TOA and BOA is also included. Results are presented for ~~3 June 2016.~~ all the case days. Low-level clouds induce a strong negative SW CRE, driven by vigorous scattering, and a positive LW CRE, due to absorption of upward radiation, resulting in a net cooling effect. The warming of the atmosphere due to absorption of SW radiation (~~~ 37.3~~$\sim 32.9\,W\,m^{-2}$) is recompensed by the

Table 6. Simulated scenarios. For scenarios S1–S3, three individual simulations (sub-cases) have been conducted according to different values for the droplet number concentration.

Scenarios			
Ref.	Double–moment scheme		
S1	Single–moment scheme		
S2	Vertical homogeneous model		
S3	Sub–adiabatic model		
S4	Mean vertical N_d profile		
Sub-cases	a. $220\,cm^{-3}$	b. N_{int}	c. $480\,cm^{-3}$

Table 7. Mean and standard deviation of modeled CREs ($\mathrm{W\,m^{-2}}$) for the SW, LW, and NET (SW+LW) radiation for the reference simulation over all case days. ~~Radiative transfer simulations have been conducted for 3 June 2016 corresponding to a Julian day number of 155. The cosine of the solar zenith angle is set to 0.7.~~ ATM stands for the atmospheric cloud radiative effect defined as the difference between the CREs at the TOA and BOA.

Ref.	$\mathrm{CRE_{SW}}$	$\mathrm{CRE_{LW}}$	$\mathrm{CRE_{NET}}$
TOA	~~-331.1 ± 77.5~~ -348.7 ± 78.39	~~9.88 ± 6.32~~ 17.51 ± 10.04	~~-323.3 ± 79.2~~ -331.2 ± 77.27
ATM	~~37.3 ± 13.9~~ 32.94 ± 12.11	~~-44.1 ± 12.5~~ -39.16 ± 13.14	~~-6.84 ± 10.1~~ -6.225 ± 12.98
BOA	~~-370.4 ± 89.7~~ -381.6 ± 86.95	~~54.0 ± 6.62~~ 56.66 ± 9.746	~~-316.4 ± 86.8~~ -324.9 ± 86.51

atmospheric LW cooling (~~~ -44.1~~ $\sim -39.2\,\mathrm{W\,m^{-2}}$), leading to a net cooling of the atmosphere (~~~ -6.84~~ $\sim -6.22\,\mathrm{W\,m^{-2}}$). The net CRE is characterized by high variability depending on the distribution of the microphysical and optical cloud properties (see Sect. 5.1.3).

Table 8 lists the difference of the mean CREs between the reference and the rest of the simulated scenarios for the SW radiation for both TOA and BOA. In the LW, all the scenarios are able to reproduce the reference mean CREs (see Table C1 in Appendix C); the difference of the mean CRE is below ~~~ 0.5~~ $\sim 0.55\,\mathrm{W\,m^{-2}}$ (in absolute values) with the vertically homogeneous run leading to the largest differences. Note here that the deviations in the CREs for the BOA and the TOA are of the same magnitude.

Overall, the single-moment radiative transfer simulations underestimate the SW CREs for both the TOA and BOA. Starting from S1a ($220\,\mathrm{cm^{-3}}$), the CREs in the single-moment run is ~~-39.5~~ $-40.1\,\mathrm{W\,m^{-2}}$ less than the double-moment one, with a root mean square error (RMSE) up to ~~48.8~~47 $\mathrm{W\,m^{-2}}$. The latter differences are attributed to the very low droplet number climatology adopted by coarse climate models (such as ECHAM, ICON-NWP) as compared to ICON-LEM. For a given liquid water path, the smaller the droplet number concentration the larger the resulting effective radius and, accordingly, the smaller the cloud reflectance. In other words, this can be seen as the magnitude of the cloud albedo effect, the so-called first indirect effect (e.g., Twomey, 1977; Ackerman et al., 2000; Werner et al., 2014). For ~~3 June 2016~~all the case days, a mean value of ~~388 ± 262~~$480 \pm 232\,\mathrm{cm^{-3}}$ is found for the droplet number concentration and a fixed N_d profile of $220\,\mathrm{cm^{-3}}$ (in the boundary layer) can only represent a small fraction of the bimodal distribution of the droplet number concentration yielded from ICON-LEM (see also Fig. 1). A single-moment run with a more representative ~~profile~~value for the droplet number concentration approximates the SW CRE with more accuracy. By employing the mean ~~N_d~~ N_int (S1c), the differences in the CRE between the single- and the double-moment runs are considerably smaller, but with quite large scatter; for the BOA (TOA), a RMSE of ~~31.2~~23.4 $\mathrm{W\,m^{-2}}$ (~~31.5~~24.3$\mathrm{W\,m^{-2}}$) and a Pearson correlation of ~~0.950 (0.928~~0.964 (0.951) is yielded. ~~Furthermore, representing the two modes in the histogram of the~~ The best scenario is found to be S1b, which is supplied by the droplet number concentration ~~(Fig.1) with the corresponding mean values of each mode (217~~weighted over the cloud geometrical extent, i.e., N_int. The differences of the mean CRES between S1b and the reference simulations leads to a RMSE of 11.7 ~~and 686 , S1d), leads to very small differences (up to 6.84~~ $\mathrm{W\,m^{-2}}$ ~~with a RMSE up to 16.1~~ and a Pearson correlation of at least 0.994 for both the BOA and TOA~~). The best scenario is found to be S1b, with a RMSE of 13.2 and a Pearson correlation~~

Table 8. Mean CRE ($W\,m^{-2}$) for the SW radiation. Results are given as differences between the new scenario minus the reference simulation (Δ). The root mean square error (RMSE) in $W\,m^{-2}$ and the Pearson (Pears.) correlation between the new scenarios and the reference simulation are also given.

Scen.	$CRE_{SW,B}$			$CRE_{SW,T}$		
	Δ	RMSE	Pears.	Δ	RMSE	Pears.
S1a	−39.2	46.4	0.960	−40.1	47.0	0.952
S1b	−7.04	11.7	0.995	−6.53	11.7	0.994
S1c	−2.59	23.4	0.964	−1.86	24.3	0.951
S2a	−26.1	39.2	0.943	−27.1	39.8	0.930
S2b	7.74	14.2	0.991	8.19	13.6	0.990
S2c	12.9	32.4	0.943	13.7	33.6	0.921
S3a	−31.1	41.4	0.950	−32.9	42.9	0.937
S3b	1.47	10.6	0.993	1.17	10.0	0.992
S3c	6.59	27.7	0.953	6.55	29.0	0.934
S4	−3.13	16.7	0.983	−3.16	17.2	0.977

~~of 0.995, but this is~~ . The latter small differences are no surprise considering the quite realistic representation of the droplet number concentration in each profile.

Having preserved the liquid water path profile (but redistributed, scenarios ~~2–4~~2–3), one can regard the changes in the CREs to the vertical stratification of low-level clouds within ICON-LEM. Comparing the SW CREs yielded by the vertically homogeneous (S2) and the sub-adiabatic runs (S3~~and S4~~), it follows that the shape of the liquid water content profile and, thus, the other cloud properties can be well represented by the sub-adiabatic model. ~~For~~ This is in agreement with our findings in Sect. 3.2 and Sect. 3.3. In brief, for the simulations with the more representative droplet number concentration ~~profiles (band d) , differences in~~ values (sub-cases), i.e., N_{int} (b) and mean N_{int} for all case days (c), the differences in the mean CREs are more pronounced for the vertically homogeneous ~~(of about −6.52 with a RMSE of 10.4 for b and −9.31 with a RMSE of 19.4 for d) simulation~~ equivalent simulation (S2) as compared to the sub-adiabatic ~~simulations (of about −1.10 $W\,m^{-2}$ $W\,m^{-2}$ with a RMSE of 8.36 for b and −3.64 $W\,m^{-2}$ with a RMSE of 16.5 $W\,m^{-2}$ for d)~~ one (S3) for both BOA and TOA: for S2b (for S2c) of about 8.19 $W\,m^{-2}$ (13.7 $W\,m^{-2}$) with a RMSE up to 14.2 $W\,m^{-2}$ (33.6 $W\,m^{-2}$) and for S3b (S3c) of about 1.47 $W\,m^{-2}$ (6.59 $W\,m^{-2}$) with a RMSE up to 10.6 $W\,m^{-2}$ (29 $W\,m^{-2}$), respectively The dependency of the latter deviations on the different droplet number concentration ~~profiles~~ values follows the same pattern as that for the single- vs double-moment schemes. For instance, in case of the ~~adiabatic scenarios~~ sub-adiabatic scenario (S3) and, going from the least to the most accurate ones, errors (in terms of the RMSE) up to 42.9 $W\,m^{-2}$ for ~~a, 32.6~~S3a (220 cm^{-3}), 29 $W\,m^{-2}$ for ~~c, 17.6~~S3c (mean N_{int}), 10.6 $W\,m^{-2}$ for ~~d, and 8.83 for b are found . This is in agreement with our findings in Sect. 3.2 and Sect. 3.3. Between the two sub-adiabatic runs (S3 and S4), they both approximate the CREs~~ S3b (N_{int}) are found for both BOA and TOA.

Table 9. ~~Spearman (Spear.) and Pearson (Pears.) correlations~~ Correlations between the cloud radiative effects for the reference simulation (Ref.) and the cloud properties. For the SW (LW) radiation, results are presented in case of the Spearman (Pearson) correlation.

Properties	$CRE_{SW,B}$	$CRE_{SW,T}$	$CRE_{LW,B}$	$CRE_{LW,T}$
	Spearman			Pearson
Q_L	~~−0.953~~ −0.957	~~−0.639~~ −0.955	~~−0.962~~ −0.129	~~−0.649 0.220 0.065 0.106 0.068~~ 0.181
τ	~~−0.998~~ −0.994	~~−0.708~~ −0.987	~~−0.996~~ 0.104	~~−0.714 0.340 0.132 −0.072 −0.005~~ 0.148
N_{int}	~~−0.680~~ −0.471	~~−0.685~~ −0.431	~~−0.649~~ 0.428	~~−0.653 0.519 0.646 −0.512 −0.671~~ −0.290
r_{int}	~~−0.177~~ −0.446	~~−0.149~~ −0.460	~~−0.211~~ −0.395	~~−0.186 −0.401 −0.486 0.694 0.700~~ 0.344
CBH	~~0.390~~ 0.148	~~0.497~~ 0.063	~~0.335~~ −0.389	~~0.435 −0.819 −0.906 0.759 0.941~~ 0.752
CTH	~~0.057~~ 0.143	~~0.294~~ −0.220	~~−0.005~~ −0.428	~~0.226 −0.788 −0.900 0.897 0.975~~ 0.765
H	~~−0.760~~ −0.795	~~−0.696~~ −0.812	~~−0.784~~ −0.200	~~−0.718 −0.014 −0.003 0.248 0.146~~ 0.226
f_{ad}	~~−0.299~~ −0.284	~~−0.267~~ −0.273	~~−0.291~~ 0.145	~~−0.257 0.124 0.101 0.068 0.018~~ 0.134

Last but not least, by replacing the vertical profile of N_d by the mean profile of N_d over all case days (see Fig. 2), emulates the cloud radiative effects of the reference simulation ~~with very high accuracy; slightly larger scatter is found for~~ quite well. Accordingly, scenario S4 ~~as compared to S3 (e. g., for b, a RMSE of 8.83~~slightly underestimates the mean SW CREs, with an mean error up to $-3.16\,\mathrm{W\,m^{-2}}$ and ~~8.36~~a RMSE up to $17.2\,\mathrm{W\,m^{-2}}$ ~~, respectively)~~for both BOA and TOA. In fact, this scenario outperforms the rest scenarios (S1–S3), except from the sub-case b (N_{int}) in all scenarios. For an illustration of the excellent linear correlation between the reference simulation and ~~S4d~~ S4 by means of a bivariate kernel density (BKD) plot, the reader is referred to Fig. B1 in Appendix B. One can see that the CREs computed by these scenarios are in a very good agreement almost everywhere except towards larger values of the CREs in case of the SW radiation.

Note here that ~~discrepancies between the scenarios might exist subject to limitations of the radiative transfer model, i.e., RRTMG~~ the RRTMG model is able to derive the radiative fluxes only for effective radius between 2.5 µm and 60 µm. ~~Scenarios associated with very low (high) values of the droplet number concentration might result in very high (low) values of the effective radius and, thus, might not fulfill the above valid range~~For all scenarios, all columns with effective radius outside this range have been excluded.

5.1.3 Impact of the cloud properties on the CREs

For a better assessment of the impact of the different cloud properties on both the SW and LW CREs their correlations have been investigated (in case of Ref.). Table 9 summarizes the corresponding correlations. Due to the monotonic relation between the SW CREs and the cloud properties and the linear relation between the LW CREs and the cloud properties, results are presented only in terms of the Spearman (monotonic) and Pearson (linear) correlations, respectively. To demonstrate, Fig. 5 and Fig. 6 illustrate the resulting bivariate kernel density between the cloud radiative effects and the cloud properties that are

essential to describe the SW and LW radiation, respectively. Considering the small differences between BOA and TOA, results are only presented for the latter one.

In the SW radiation, there is an excellent monotonic relation between the CREs and τ, Q_{L}, and H for both BOA and TOA, with ~~spearman~~ Spearman correlations higher than ~~−0.996, 0.953, and −0.76~~ −0.987, −0.955, and −0.795, respectively (see Table 9 and Fig. 5), following the second rotational component (RC-2, see Table 4). In particular, the SW CREs increase monotonically with the liquid water path. The latter monotonic relation that is found stronger for lower values of the liquid water path saturates at $Q_{\mathrm{L}} > 300\,\mathrm{g\,m^{-2}}$. In the same direction are the findings for τ (not shown here) and H with the saturation occurring at ~ 60 and $\sim 0.75\,\mathrm{km}$, respectively. This is no surprise considering their relation to Q_{L} (see Eqs. 10 and 16). From Eq. (14), one could expect a similar correlation between the SW cloud radiative effect and the effective radius, but a Spearman correlation below ~~0.21~~ 0.46 (in absolute values) is found for both the BOA and TOA. ~~This is no surprise considering the derivation of the effective radius by the~~ The latter can be explained by the way the droplet number concentration is derived (see Eq. 4) and the two modes that ~~are clearly seen in panels~~ can be seen in panel (c) ~~and (g)~~ of Fig. 5. The Spearman correlations of the SW CRE with the cloud borders and f_{ad} are very weak. In the LW radiation, changes in Q_{L} (and, thus, in τ and H) possess only a minor influence on CREs (see Table 9) with ~~Spearman (Pearson) correlations below 0.34 (0.15~~Pearson correlations below 0.226 (in absolute values). In addition, effective radius and droplet number concentration have a moderate effect on the CRE; Pearson correlations are below ~~0.7~~0.428 (in absolute values). The cloud radiative effect in the LW is mostly dependent on the macrophysical cloud properties, namely the cloud position and vertical extension that impacts the cloud temperature~~(see Table~~ , following the first rotational component (RC-1, see Table 4). Thus, we would expect a strong linear correlation with CBH and CTH. This holds true, but only in case of the TOA, whereby a Pearson correlation above 0.752 was yielded (see Table 9 and Fig. 6)~~with Spearman (Pearson) correlations above 0.76 (0.9)~~ . For the BOA, the correlations are below 0.428 (in absolute values~~, following the first rotational component (RC-1, see Table 4). Thereby~~) for both CBH and CTH. This can be explained by the large variability in CBH and CTH among the different case days (see Table 1). It follows that CRE at the BOA is much more sensitive to the macrophysical cloud properties as compared to the CRE at the TOA.

Finally, we further examined the relation between the first two rotational components and the cloud radiative effects. Confirming our assumption, in Fig. 7, an excellent monotonic relation is found between SW CRE and RC-2 that is comprised by τ, Q_{L}, and H, while a strong linear relation is obtained between LW CRE and RC-1 in case of the TOA, which is described by CBH and CTH. ~~Even the corresponding densities follow similar patterns, e. g., Fig. 5 panels (a) or (b) with~~ The resulting Spearman and Pearson correlations are larger than 0.948 for the SW and 0.86 for the LW (for TOA only), respectively. Once again, low linear correlation is found between the LW CRE and RC-1 for the BOA. In Fig. 7~~panel (b)and Fig. 6 panel (b)with Fig. 7 panel (~~, panel (d)~~. The resulting Spearman and Pearson correlations are larger than 0.96 and 0.91, respectively. ~~, one can clearly identify several clusters that correspond to different days. With this in mind, we further investigated the latter correlation for each day individually (not shown here). For example, the two lower clusters, with $\mathrm{CRE_{LW,B}} < 50\,\mathrm{W\,m^{-2}}$, are linked to 29 July 2014, while the two upper clusters ($\mathrm{CRE_{LW,B}} > 70\,\mathrm{W\,m^{-2}}$) are regarded to 5 May 2013.

~~As described in the beginning of Sect. 3.1, the mean distribution of N_{int} is comprised by two clear modes centered around 217 $\mathrm{cm^{-3}}$ and 686 $\mathrm{cm^{-3}}$ (for 3 June 2016). In addition to this, Fig. 5 further supports this finding and further indicates a strong~~

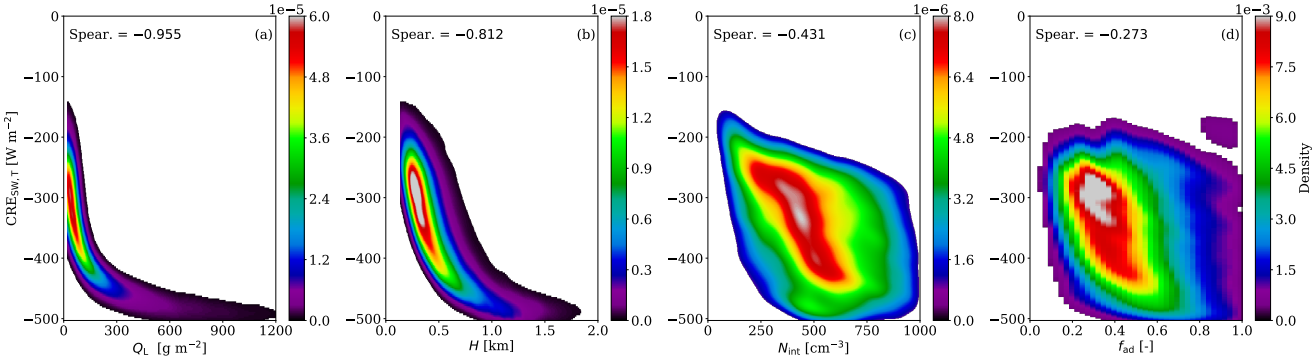

Figure 5. Bivariate kernel density (BKD) between the reference simulation (Ref.) and the cloud properties that are essential for the derivation of the cloud optical thickness that is one of the fundamental properties describing the SW cloud radiative effect. ~~Lower panels~~Panels illustrate the BKD between the $\mathrm{CRE_{SW,T}}$ and (a) Q_L, (b) H, (c) N_int, and (d) f_ad~~, while, the upper panels the BKD between the $\mathrm{CRE_{SW,T}}$ and (e) Q_L, (f) H, (g) N_int, and (h) f_ad~~. The corresponding Spearman (Spear.) ~~and Pearson (Pears.)~~ correlations are highlighted.

~~dependency of the CREs on N_int. Thus, we further separated the cloud profiles according to the latter two clusters using as, a mid point, a droplet number concentration of 388 $\mathrm{cm^{-3}}$. Subsequently, the correlations between the CREs in the shortwave radiation and all the cloud properties have improved significantly in case of clouds that fell into the right part of the distribution of N_int. For the LW radiation, a similar increase in correlations, but smaller in magnitude as compared to the SW, is found only for CREs at the TOA. For details with respect to the resulting correlations, the reader is referred to Table C2 in Appendix C. In particular, the largest increase in correlations is found bettwen $\mathrm{CRE_{SW}}$ and r_int for high values of the droplet number concentration, with Spearman and Pearson correlations above -0.820 and -0.796, respectively. The latter relationship that is more evident at high values of the droplet number concentration can be explained by the first indirect aerosol effect (e.g., Twomey et al., 1977; Ackerman et al., 2000; Werner et al., 2014).~~

To this end, based on the robust evidence over all case days, such a statistical approach, i.e., ~~principal component analysis(plus varimax rotation)~~rotational component analysis, can be ~~used~~ employed as an alternative ~~concept~~ concept for describing the low-level clouds and, ~~consequently~~consequently, their radiative impact.

6 Discussion and conclusions

By analyzing simulations of the high-resolution model ICON-LEM, a sensitivity study has been carried out to investigate the suitability of the vertically homogeneous and the sub-adiabatic cloud models to, firstly, serve as conceptual models for the evaluation of the representation of low-level clouds in ICON-LEM and similar high-resolution models, and to, secondly, capture the relevant properties which determine the cloud radiative effect. Considering the representation of the cloud microphysical

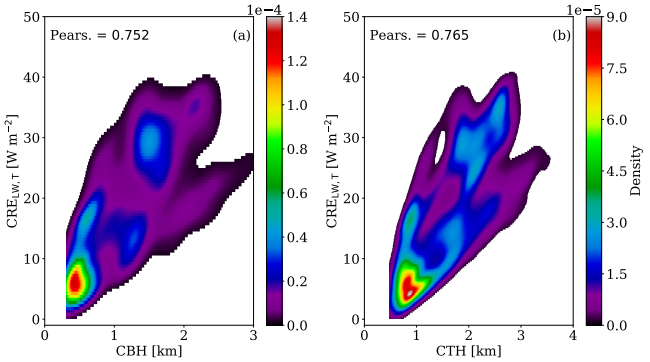

Figure 6. Bivariate kernel density (BKD) between the reference simulation (Ref.) and the cloud properties describing the LW cloud radiative effect ~~for~~ at the TOA and (a) CBH ~~,~~ and (b) CTH~~, and for the TOA and (c) CBH, (d) CTH~~. The corresponding ~~Spearman (Spear.) and~~Pearson (Pears.) correlations are highlighted.

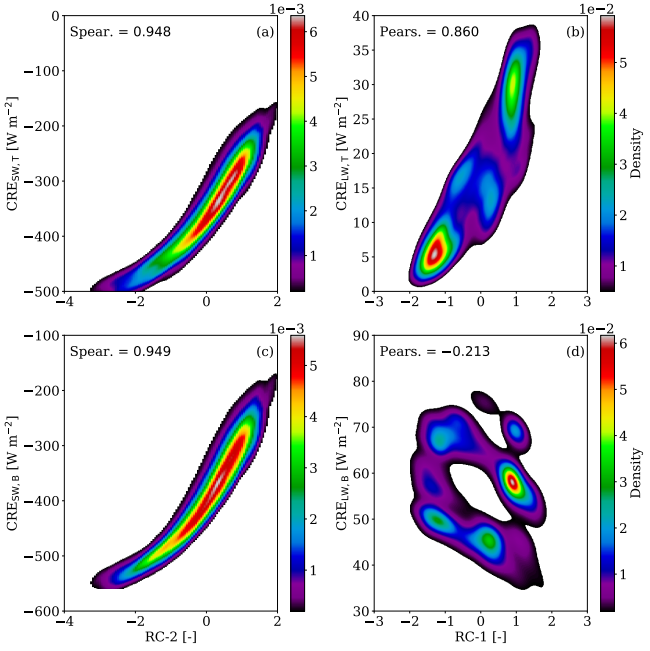

Figure 7. For the reference simulation (Ref.), bivariate kernel density (BKD) between CRE_{SW} and the second rotational component (RC-2) at ~~(a) BOA, (b) TOA and between CRE_{LW} and the first rotational component (RC-1) at (c) BOA, (d) TOA~~(a) TOA, (c) BOA and between CRE_{LW} and the first rotational component (RC-1) at (b) TOA, (d) BOA . The corresponding Spearman (Spear.) and Pearson (Pears.) correlations are highlighted for the SW and LW radiation, respectively .

processes in ICON-LEM, we additionally have highlighted the differences in cloud radiative effect resulting from the use of a double- instead of a single-moment cloud microphysics scheme.

ICON-LEM, with its high vertical resolution, ranging from 25 m to 70 m within the boundary layer, and from 70 m to 100 m further up ~~until the upper altitude level of our area of study~~to the altitude limit for the occurrence of low-level clouds selected for this study (4000 m), enables ~~the~~a significantly improved investigation of the vertical distribution of microphysical properties of ~~low-level~~theseclouds. Based on six case days, we find that the behavior of modeled liquid water clouds over Germany more closely resembles the sub-adiabatic than the vertically homogeneous one, in agreement with ground-based observational studies over the same are of interest (Merk et al., 2016). A rather large number of vertical profiles of modeled low-level clouds has been considered in this study and supports the use of the sub-adiabatic model as a conceptual tool for the evaluation of these profiles in high-resolution models, in agreement with previous studies that supported ~~their~~ its use in parameterizations in GCMs (Brenguier et al., 2000). According to the sub-adiabatic model, the key cloud properties which determine the cloud optical thickness and, thus, the SW CRE are the liquid water path, the vertically integrated droplet number concentration (over the cloud geometrical extend, in agreement with Han et al., 1998), the sub-adiabatic fraction, and the cloud geometrical extent, which provide a simplified approximation of the vertical structure of clouds. Consistent with this model, we have demonstrated that the cloud optical thickness varies proportionally to $Q_{\mathrm{L}}^{5/6}$ and not linearly with Q_{L}, as predicted by the vertically homogeneous model that further supports both observational and theoretical studies (e.g., Brenguier et al., 2000; Merk et al., 2016). In addition, an effort has been conducted to predict the cloud optical thickness resulting from ICON-LEM by the formulation suggested by the sub-adiabatic model. We employed the ordinary least squares (OLS) regression method and we show that~~for our cases, 95.71~~, for all case days, the sub-adiabatic model approximates the cloud optical thickness with high accuracy (RMSE = 0.027). In brief, in this prediction, 95.7 % of the variance in cloud optical thickness is explained by the variance in the liquid water path, while the droplet number concentration and the sub-adiabatic fraction contribute ~~only~~ 3.5 % and ~~0.14~~0.2 % to the total variance, respectively~~, outlining the relative importance of the latter properties for describing the SW radiative effect~~. The sub-adiabatic fraction of clouds is characterized by a large variability ($f_{\mathrm{ad}} = 0.45 \pm 0.21$) that strongly varies from day-to-day, but also within the same day, likely driven by entrainment processes. The latter is in agreement with previous studies based on ground-based observations (e.g., Boers et al., 2006; Kim et al., 2008; Merk et al., 2016) and the identification of influential factors is an important goal for future research. Furthermore, ~~we managed to support the outcome of~~our results confirm the findings of Min et al. (2012); Merk et al. (2016) that the highest values of adiabaticity is linked with optically and geometrically thin clouds. Considering the aforementioned variability of entrainment, the constant and comparatively high values of f_{ad}, which are often adopted in satellite retrievals of cloud droplet number concentration or cloud geometric thickness (e.g., Zeng et al., 2014) are not supported, and might lead to discrepancies in model validation. Therefore, a much lower value of f_{ad} ranging from 0.4 to 0.6 should be utilized in the sub-adiabatic model to link the cloud optical thickness to the prognostic quantities utilized in GCM parameterizations and determine the indirect effect and cloud feedbacks. The latter value of the sub-adiabatic fraction is close to the one adopted by Grosvenor et al. (2018) for the error assessment of the retrieved N_{d}.

The vertical variability of the droplet number concentration was examined. For ~~3 June 2016~~all the case days , above an altitude of about 2 km, values of N_d ~~lie~~are about 200 cm^{-3} and are, thus, close to climatological values, while in the boundary layer, the double moment scheme predicts N_d values ~~of about~~ above 600 cm^{-3}. Such values are ~~considered~~ regarded as rather high compared to satellite remote sensing estimates (Quaas et al., 2006; Grosvenor et al., 2018)~~; in situ observations~~ , but such comparison is rather vague considering, firstly, the large uncertainties of the satellite-derived estimates of cloud droplet number concentration (Grosvenor et al., 2018) and, secondly, they are not available in high resolution. However, in situ observations, which are considered to be the most accurate approach to determine N_d, suggest higher values ~~of N_d and, thus~~and, hence, lie closer to those simulated by ICON-LEM~~, but are affected by large instrumental uncertainties (Grosvenor et al., 2018). This identifies a potential weakness in the~~ . Thus, by means of in situ observations, evaluation activities should be conducted for a better characterization of the droplet number concentration from remote sensing techniques. The latter will scrutinize the double-moment scheme ~~and a scrutinization~~ implemented in ICON-LEM and could potentially ~~could be useful for further evaluation activities of microphysics parameterization that could~~lead to better simulations of cloud processes and radiation. A principal component analysis and a subsequent varimax rotation (rotational component analysis) of cloud properties ~~has~~ have been conducted to explore the covariance of cloud properties and radiative effects, and to identify ~~their degrees of freedom and~~ the dominating modes of variability. The goal ~~has been~~ was ultimately to uncover potential shortcomings in ~~their representation in models~~the representation of clouds towards the computation of the cloud radiative effects. This analysis reveals that, out of the set of nine parameters considered by us, only four components are sufficient to explain ~~98~~97.7 % of the total variance. The first ~~rotational~~ component comprises the cloud bottom and top heights, and thus corresponds to the vertical location of the cloud layer in the atmosphere. The second component combines liquid water path, optical thickness, and geometric extent of the clouds, while the third and fourth component are ~~dominated by the contributions~~ functions of the sub-adiabatic fraction and the cloud droplet number concentration, respectively. By means of such a statistical approach, ~~i.e., principal component analysis (plus varimax rotation),~~ we offer an alternative concept for describing the CREs, with the first and second component representing the main modes of variability determining the LW and SW CREs ~~. While~~ explaining 33.8 % and 35.5 %, respectively. The third and fourth component, while having smaller contributions to the total variance ~~, the third and fourth component are also relevant and~~ (14.8 % and 13.6 %, respectively), point to clear degrees of freedom. Moreover, they potentially capture signatures of the ~~so-called~~ second (cloud geometric extent, Pincus and Baker, 1994) and first indirect aerosol effects (e.g., Twomey, 1977; Ackerman et al., 2000; Werner et al., 2014). This analysis points to the reduced set of parameters for the representation of low-level clouds towards the computation of the CREs: the column effective properties, i.e., N_int, Q_L, f_ad, H, and one of the CTH or CBH. A similar attempt to provide an alternative concept for the description of the CREs was reported by Schewski and Macke (2003); they tried to correlate domain averaged radiative fluxes from 3D fields with domain averaged properties of cloudy atmospheres.

By means of an offline version of the RRTMG radiative transfer model, idealized simulations have been carried out to estimate the effect of the representation of cloud microphysics in ICON-LEM on the cloud radiative effect; the double-moment scheme implemented in ICON-LEM (Seifert and Beheng, 2006) has been compared to that of a single-moment scheme. Special emphasis was given on the characterization of the droplet number concentration ~~profile~~ and, thus, ~~the~~ an effective radius, that

could approximate the microphysical and radiative properties of the modeled low-level clouds as simulated by ICON-LEM (reference scenario). Utilizing a droplet number concentration profile that follows the climatology of a coarse atmospheric model~~s~~ (ECHAM), the single-moment scheme would yield values of the SW CRE which are up to ~~~ 39~~ $\sim 40.1\,\mathrm{W\,m^{-2}}$ less than those of the double-moment scheme, with a RMSE of ~~~ 49~~ $\sim 47\,\mathrm{W\,m^{-2}}$. By employing a more representative profile for the N_d, i.e., ~~two fixed values representing the two modes in the histogram of the droplet number concentration produced by the double-moment scheme~~ a mean vertical profile of N_d for all case days, leads to a rather good approximation; the RMSE is below ~~16~~17.2 $\mathrm{W\,m^{-2}}$. This points to the need to better account for prognostic N_d calculations.

~~We~~ Finally, we investigated the reliability of the vertically homogeneous and the sub-adiabatic model to determine the ~~clouds~~ cloud radiative effects. ~~The dependency of the differences in CREs (compared to the reference run) on the different droplet number concentration profiles follows the same pattern as for the single- vs double-moment scheme. For the more representative N_d profiles~~Overall, the sub-adiabatic cloud model outperforms the vertically homogeneous one for the representation of low-level clouds for calculating their radiative effects. ~~and further suggests its use as basis for evaluation of GCM parameterizations, in agreement with (Brenguier et al., 2000).~~

Based on our results, the following approach is recommended to evaluate the representation of clouds and their radiative effects as simulated by high-resolution atmospheric models: for the shortwave, the vertically integrated water path should be targeted primarily, which is quite reliably retrieved from remote sensing; recent advances in correcting the PP bias enable the retrieval of the liquid water path with high accuracy (Zhang et al., 2016; Werner et al., 2018). In addition, the cloud droplet number concentration and the sub-adiabatic fraction are of relevance and deserve attention, but their reliable derivation remains challenging both due to the limitations of current remote sensing methods and the lack of validation data on the basis of in situ observations (Grosvenor et al., 2018). In this respect, the rather large values of cloud droplet number concentration reported here as predicted by the two-moment scheme of Seifert and Beheng (2006), N_d should be scrutinized on the basis of in situ observations. For the computation of the cloud radiative effects, ~~the vertical profile of~~ a more representative vertical profile for the droplet number concentration ~~is of less importance and fixed profiles~~ could be used, as long as they can represent the different magnitudes in N_d within and above the boundary layer as shown here. For the LW CRE, the cloud base and top heights are the determining factors that are rather well derived from ground- and satellite-based observations, respectively. It has be noted, however, that the reliable determination of cloud base height from satellites remains challenging. The sub-adiabatic fraction is also of interest, as it controls the geometric extent of clouds for a given value of liquid water path. Based on our findings, the sub-adiabatic model seems to be better suited than the vertically homogeneous model for the evaluation of the representation of clouds in models.

In future work, the results presented here should be combined with efforts to also take into account the impact of horizontal cloud variability, and in particular of the cloud fraction, which are well-known factors of relevance for the cloud radiative effect. In order to link deficiencies in the CRE to the model representation of cloud properties, an effort should be made to simultaneously evaluate the ICON-LEM-based fluxes and cloud properties discussed here to observations, e.g., through the combined use of irradiances observed at the top of atmosphere by the Geostationary Earth Radiation Budge (GERB) and at the

ground together with measurements of liquid water path, cloud top and bottom height, cloud droplet number concentration, and solar fluxes. This requires the synergistic combination of active and passive remote sensing instruments.

Appendix A: Derivation of moments of the droplet size distribution

In Sect. 2.1, the generalized gamma distribution describing the mass of hydrometeors was introduced (see Eq. 1). The ηth moment is computed by,

$$M_{\mathrm{m}}^{\eta} = A_{\mathrm{m}} \frac{\Gamma(\frac{\eta+\nu+1}{\xi})}{\xi \cdot B_{\mathrm{m}}^{(\frac{\eta+\nu+1}{\xi})}}. \tag{A1}$$

Γ stands for the gamma function. For cloud droplets $\nu = \xi = 1$ (see Table 1 in Seifert and Beheng, 2006), the zeroth and first moments of the mass size distribution that denote the droplet number concentration and the liquid water content, respectively, are derived,

$$M_{\mathrm{m}}^{0} = A_{\mathrm{m}} \frac{\Gamma(2)}{B_{\mathrm{m}}^{2}} = N_{\mathrm{d}}, \tag{A2}$$

and

$$M_{\mathrm{m}}^{1} = A_{\mathrm{m}} \frac{\Gamma(3)}{B_{\mathrm{m}}^{3}} = q_{\mathrm{L}}. \tag{A3}$$

Dividing Eq. (A2) by Eq. (A3), one can obtain,

$$B_{\mathrm{m}} = \frac{2 \cdot N_{\mathrm{d}}}{q_{\mathrm{L}}}. \tag{A4}$$

Inserting Eq. (A4) in Eq. (A2) and rearranging gives,

$$A_{\mathrm{m}} = \frac{4 \cdot N_{\mathrm{d}}^{3}}{q_{\mathrm{L}}^{2}}. \tag{A5}$$

According to Seifert and Beheng (2006) and Petty and Huang (2011), a power law is applied for the mass-size relation,

$$x_{\mathrm{m}} = \alpha \cdot \mathrm{d}x = \alpha \cdot b \cdot D^{b-1} \mathrm{d}D. \tag{A6}$$

D denotes the geometrical diameter. In case of spherical particles, $\alpha = \frac{\pi \cdot \rho_{\mathrm{w}}}{6}$ and $b = 3$, with ρ_{w} being the water density. In Table 2 in Petty and Huang (2011), one can find the transformation factors between the mass of hydrometers and the diameter of the hydrometers,

$$A = b \cdot A_{\mathrm{m}} \cdot \alpha^{\nu}, \tag{A7}$$

$$\beta = b(\nu + 1) - 1, \tag{A8}$$

$$B = B_{\mathrm{m}} \cdot \alpha^{\nu}, \tag{A9}$$

$$\mu = b \cdot \nu. \tag{A10}$$

Given the aforementioned relations, the formula describing the modified gamma distribution of the DSD is,

$$n(D) = A \cdot D^{\beta} \cdot \exp(-B \cdot D). \tag{A11}$$

Accordingly, the ηth moments of the DSD are given by,

$$M^{\eta} = A\frac{\Gamma(\eta+\beta+1)}{B^{(\eta+\beta+1)}}. \tag{A12}$$

For the reconstructed DSD, $n(D)$, the zeroth moment (M^0) stands for the droplet number concentration. The volume-equivalent radius, r_{V}, is derived from the third moment,

$$r_{\mathrm{V}} = \frac{1}{2}\sqrt[3]{\frac{\int_0^{\infty} n(D)\,(D)^3\,\mathrm{d}D}{(D)^0}\,\frac{\int_0^{\infty} n(D)\,(D)^3\,\mathrm{d}D}{N_{\mathrm{d}}}}. \tag{A13}$$

Appendix B: ~~Figures~~Correlation between reference simulation and scenario S4

In sect. 5.1.2, by conducting idealized radiative transfer simulations, we estimated the impact of the representation of cloud properties in ICON-LEM on the cloud radiative effects (CREs). Special emphasis was given on identifying the droplet number concentration (N_{d}), which approximates the microphysical and radiative properties of low-level clouds as simulated by ICON-LEM (reference scenario). A radiative transfer simulation, which employs a mean vertical profile of N_{d} of all the case days (scenario S4), approximates the CREs of the reference scenario quite well. Figure B1 depicts the excellent linear correlation between the reference simulation and S4 by means of a bivariate kernel density (BKD).

Appendix C: ~~Tables~~Differences of the mean CREs between the reference simulation and the new scenarios for the LW radiation

Table C1 lists the difference of the mean CREs between the reference and the rest of the simulated scenarios for the LW radiation for both TOA and BOA. All scenarios are able to reproduce the reference mean CREs; the difference of the mean CREs is below $\sim 0.55\,\mathrm{W\,m^{-2}}$ (in absolute values).

~~Spearman and Pearson (Spearman/Pearson) between the cloud radiative effects and the cloud properties for the two major clusters characterized by low N_{int} values (L) and high N_{int} values (H).~~

Data availability. The full 3D large eddy simulation fields used for this paper are stored at the Deutsche Klima Rechenzentrum archive (DKRZ) as part of the HD(CP)2 project.

Code and data availability. The Python RRTMG interface (pyRRTMG) used in this study is available ~~online~~ at https://github.com/hdeneke/pyRRTMG.

Author contributions. VB conceived and refined the overall structure of the investigation, based on discussions with and feedback from all co-authors. VB carried out and refined the data analysis. HD implemented the Python interface to RRTMG used in the analysis. VB wrote the draft manuscript, with all authors contributing to the interpretation of the results and to its improvement.

Competing interests. The authors declare that they have no conflict of interest.

Acknowledgements. This work has been conducted in the framework of the High Definition Clouds and Precipitation for Advancing Climate Prediction HD(CP)^2, funded by the German Federal Ministry of Education and Research BMBF under grant no. 01LK1504B. We thank our colleagues, Anja Hünerbein and Frank Werner, for the many thoughtful comments that led to the improvement of the manuscript.

~~Bivariate kernel density (BKD) between the cloud optical thickness and the liquid water path on a logarithmic scale.~~

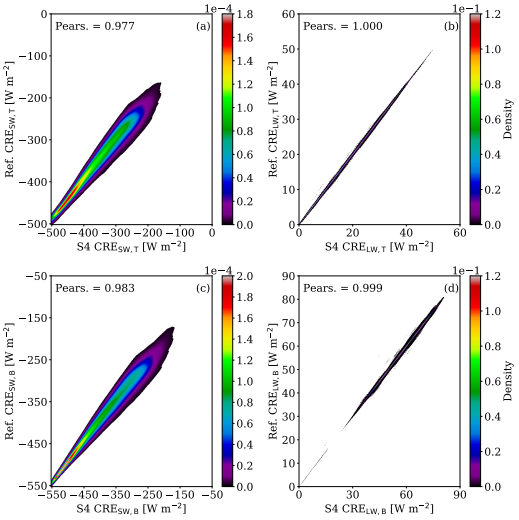

Figure B1. ~~Bivariate kernel density (BKD) between the reference simulation (Ref.) and the modified sub-adiabatic run (S4d) in case of the droplet number concentration representing the two clusters in the histogram of N_{int} (see Fig. 1). For the CREs, BKD are presented for the SW radiation at the BOA (a), TOA (b), and for the LW radiation at the BOA (c) and TOA (d).~~Bivariate kernel density (BKD) between the reference simulation (Ref.) and the scenario that employs the mean vertical N_{d} profile (S4). For the CREs, BKD are presented for the SW radiation at the TOA (a) and BOA (c), and for the LW radiation at the TOA (b) and BOA (d) The corresponding ~~Spearman (Spear.) and~~Pearson (Pears.) correlations are highlighted.

Table C1. Mean CRE ($W\,m^{-2}$) for the LW radiation. Results are given as differences between the new scenario minus the reference simulation (Δ). The root mean square error (RMSE) in $W\,m^{-2}$ and the Pearson (Pears.) correlation between the new scenarios and the reference simulation are also given.

Scen.	$CRE_{LW,B}$			$CRE_{LW,T}$		
	Δ	RMSE	Pears.	Δ	RMSE	Pears.
S1a	−0.11	0.48	0.999	−0.04	0.19	1.000
S1b	−0.05	0.40	0.999	−0.03	0.18	1.000
S1c	−0.01	0.50	0.999	−0.01	0.22	1.000
S2a	0.40	0.79	0.998	0.23	0.51	0.999
S2b	0.51	0.82	0.998	0.27	0.53	0.999
S2c	0.55	0.85	0.998	0.29	0.54	0.999
S3a	−0.05	0.74	0.997	0.33	0.64	0.999
S3b	−0.01	0.73	0.997	0.36	0.65	0.999
S3c	0.02	0.83	0.996	0.37	0.68	0.998
S4	−0.02	0.49	0.999	−0.02	0.22	1.000

References

Ackerman, A., Toon, O., Taylor, J., Johnson, D., Hobbs, P., and Ferek, R.: Effects of aerosols on cloud albedo: Evaluation of Twomey's parameterization of cloud susceptibility using measurements of ship tracks, J. Atmos. Sci., 57, 2684–2695, 2000.

Albrecht, B. A., Fairall, C. W., Thomson, D. W., White, A. B., Snider, J. B., and Schubert, W. H.: Surface-based remote sensing of the observed and the Adiabatic liquid water content of stratocumulus clouds, Geophys. Res. Lett., 17, 89–92, https://doi.org/10.1029/GL017i001p00089, 1990.

Anderson, G., Clough, S., Kneizys, F., Chetwynd, J., and Shettle, E.: AFGL Atmospheric Constituent Profiles (0–120 km), Tech. Rep. AFGL-TR-86-0110, AFGL (OPI), Hanscom AFB, MA 01736, 1986.

Barker, H. W.: Indirect Aerosol Forcing by Homogeneous and Inhomogeneous Clouds, J. Climate, 13, 4042–4049, https://doi.org/10.1175/1520-0442(2000)013<4042:IAFBHA>2.0.CO;2, 2000.

Barker, H. W. and Räisänen, P.: Neglect by GCMs of subgrid-scale horizontal variations in cloud-droplet effective radius: A diagnostic radiative analysis, Q. J. Roy. Meteor. Soc., 130, 1905–1920, https://doi.org/10.1256/qj.03.116, 2004.

Bennartz, R.: Global assessment of marine boundary layer cloud droplet number concentration from satellite, J. Geophys. Res.-Atmos., 112, n/a–n/a, https://doi.org/10.1029/2006JD007547, 2007.

Boers, R., Acarreta, J. R., and Gras, J. L.: Satellite monitoring of the first indirect aerosol effect: Retrieval of the droplet concentration of water clouds, J. Geophys. Res.-Atmos., 111, n/a–n/a, https://doi.org/10.1029/2005JD006838, 2006.

Brenguier, J.-L., Pawlowska, H., Schüller, L., Preusker, R., Fischer, J., and Fouquart, Y.: Radiative Properties of Boundary Layer Clouds: Droplet Effective Radius versus Number Concentration, J. Atmos. Sci., 57, 803–821, https://doi.org/10.1175/1520-0469(2000)057<0803:RPOBLC>2.0.CO;2, 2000.

Cahalan, R. F., Ridgway, W., Wiscombe, W. J., Gollmer, S., and Harshvardhan: Independent Pixel and Monte Carlo Estimates of Stratocumulus Albedo, J. Atmos. Sci., 51, 3776–3790, doi:10.1175/1520-0469(1994)051<3776:IPAMCE>2.0.CO;2, 1994.

Cairns, B., Lacis, A. A., and Carlson, B. E.: Absorption within Inhomogeneous Clouds and Its Parameterization in General Circulation Models, J. Atmos. Sci., 57, 700–714, https://doi.org/10.1175/1520-0469(2000)057<0700:AWICAI>2.0.CO;2, 2000.

Chosson, F., Brenguier, J.-L., and Schüller, L.: Entrainment-Mixing and Radiative Transfer Simulation in Boundary Layer Clouds, J. Atmos. Sci., 64, 2670–2682, https://doi.org/10.1175/JAS3975.1, 2007.

Clough, S., Shephard, M., Mlawer, E., Delamere, J., Iacono, M., Cady-Pereira, K., Boukabara, S., and Brown, P.: Atmospheric radiative transfer modeling: a summary of the AER codes, J. Quant. Spectrosc. Radiat. Transfer, 91, 233–244, https://doi.org/https://doi.org/10.1016/j.jqsrt.2004.05.058, 2005.

Collins, W. D., Rasch, P. J., Boville, B. A., Hack, J. J., McCaa, J. R., Williamson, D. L., Briegleb, B. P., Bitz, C. M., Lin, S.-J., and Zhang, M.: The Formulation and Atmospheric Simulation of the Community Atmosphere Model Version 3 (CAM3), J. Climate, 19, 2144–2161, https://doi.org/10.1175/JCLI3760.1, 2006.

Di Giuseppe, F. and Tompkins, A. M.: Effect of Spatial Organization on Solar Radiative Transfer in Three-Dimensional Idealized Stratocumulus Cloud Fields, J. Atmos. Sci., 60, 1774–1794, https://doi.org/10.1175/1520-0469(2003)060<1774:EOSOOS>2.0.CO;2, 2003.

Dipankar, A., Stevens, B., Heinze, R., Moseley, C., Zängl, G., Giorgetta, M., and Brdar, S.: Large eddy simulation using the general circulation model ICON, J. Adv. Model. Earth Syst., 7, 963–986, https://doi.org/10.1002/2015MS000431, 2015.

Foth, A. and Pospichal, B.: Optimal estimation of water vapour profiles using a combination of Raman lidar and microwave radiometer, Atmos. Meas. Tech., 10, 3325–3344, https://doi.org/10.5194/amt-10-3325-2017, 2017.

Gassmann, A. and Herzog, H.-J.: Towards a consistent numerical compressible non-hydrostatic model using generalized Hamiltonian tools, Q. J. Roy. Meteor. Soc., 134, 1597–1613, https://doi.org/10.1002/qj.297, https://rmets.onlinelibrary.wiley.com/doi/abs/10.1002/qj.297, 2008.

Giorgetta, M., Roeckner, E., Mauritsen, T., Bader, J., Crueger, T., Esch, M., Rast, S., Kornblueh, L., Schmidt, H., Kinne, S., Hohenegger, C., Möbis, B., Krismer, T., Wieners, K.-H., and Stevens, B.: The atmospheric general circulation model ECHAM6 - Model description, Max-Planck-Institut für Meteorologie, 135, https://doi.org/10.17617/2.1810480, 2013.

Grosvenor, D. P., Sourdeval, O., Zuidema, P., Ackerman, A., Alexandrov, M. D., Bennartz, R., Boers, R., Cairns, B., Chiu, J. C., Christensen, M., Deneke, H., Diamond, M., Feingold, G., Fridlind, A., Hünerbein, A., Knist, C., Kollias, P., Marshak, A., McCoy, D., Merk, D., Painemal, D., Rausch, J., Rosenfeld, D., Russchenberg, H., Seifert, P., Sinclair, K., Stier, P., van Diedenhoven, B., Wendisch, M., Werner, F., Wood, R., Zhang, Z., and Quaas, J.: Remote Sensing of Droplet Number Concentration in Warm Clouds: A Review of the Current State of Knowledge and Perspectives, Rev. Geophys., 56, 409–453, https://doi.org/10.1029/2017RG000593, 2018.

Han, Q., Rossow, W. B., Chou, J., and Welch, R. M.: Global variation of column droplet concentration in low-level clouds, Geophys. Res. Lett., 25, 1419–1422, https://doi.org/10.1029/98GL01095, 1998.

Hande, L. B., Engler, C., Hoose, C., and Tegen, I.: Parameterizing cloud condensation nuclei concentrations during HOPE, Atmos. Chem. Phys., 16, 12 059–12 079, https://doi.org/10.5194/acp-16-12059-2016, 2016.

Hansen, J. E. and Travis, L. D.: Light scattering in planetary atmospheres, Space Sci Rev, 16, 527–610, https://doi.org/10.1007/BF00168069, 1974.

Heinze, R., Dipankar, A., Henken, C. C., Moseley, C., Sourdeval, O., Trömel, S., Xie, X., Adamidis, P., Ament, F., Baars, H., Barthlott, C., Behrendt, A., Blahak, U., Bley, S., Brdar, S., Brueck, M., Crewell, S., Deneke, H., Di Girolamo, P., Evaristo, R., Fischer, J., Frank, C., Friederichs, P., Göcke, T., Gorges, K., Hande, L., Hanke, M., Hansen, A., Hege, H.-C., Hoose, C., Jahns, T., Kalthoff, N., Klocke,

D., Kneifel, S., Knippertz, P., Kuhn, A., van Laar, T., Macke, A., Maurer, V., Mayer, B., Meyer, C. I., Muppa, S. K., Neggers, R. A. J., Orlandi, E., Pantillon, F., Pospichal, B., Röber, N., Scheck, L., Seifert, A., Seifert, P., Senf, F., Siligam, P., Simmer, C., Steinke, S., Stevens, B., Wapler, K., Weniger, M., Wulfmeyer, V., Zängl, G., Zhang, D., and Quaas, J.: Large-eddy simulations over Germany using ICON: a comprehensive evaluation, Q. J. R. Meteorol. Soc., 143, 69–100, https://doi.org/10.1002/qj.2947, 2017.

Hu, Y. X. and Stamnes, K.: An Accurate Parameterization of the Radiative Properties of Water Clouds Suitable for Use in Climate Models, J. Climate, 6, 728–742, https://doi.org/10.1175/1520-0442(1993)006<0728:AAPOTR>2.0.CO;2, 1993.

Iacono, M. J., Delamere, J. S., Mlawer, E. J., Shephard, M. W., Clough, S. A., and Collins, W. D.: Radiative forcing by long-lived greenhouse gases: Calculations with the AER radiative transfer models, J. Geophys. Res.-Atmos., 113, https://doi.org/https://doi.org/10.1029/2008JD009944, 2008.

Illingworth, A. J., Hogan, R. J., O'Connor, E., Bouniol, D., Brooks, M. E., Delanoë, J., Donovan, D. P., Eastment, J. D., Gaussiat, N., Goddard, J. W. F., Haeffelin, M., Baltink, H. K., Krasnov, O. A., Pelon, J., Piriou, J.-M., Protat, A., Russchenberg, H. W. J., Seifert, A., Tompkins, A. M., van Zadelhoff, G.-J., Vinit, F., Willén, U., Wilson, D. R., and Wrench, C. L.: Cloudnet, Bull. Amer. Meteor. Soc., 88, 883–898, https://doi.org/10.1175/BAMS-88-6-883, 2007.

Illingworth, A. J., Barker, H. W., Beljaars, A., Ceccaldi, M., Chepfer, H., Clerbaux, N., Cole, J., Delanoë, J., Domenech, C., Donovan, D. P., Fukuda, S., Hirakata, M., Hogan, R. J., Huenerbein, A., Kollias, P., Kubota, T., Nakajima, T., Nakajima, T. Y., Nishizawa, T., Ohno, Y., Okamoto, H., Oki, R., Sato, K., Satoh, M., Shephard, M. W., Velázquez-Blázquez, A., Wandinger, U., Wehr, T., and van Zadelhoff, G.-J.: The EarthCARE Satellite: The Next Step Forward in Global Measurements of Clouds, Aerosols, Precipitation, and Radiation, Bull. Amer. Meteor. Soc., 96, 1311–1332, https://doi.org/10.1175/BAMS-D-12-00227.1, 2015.

IPCC: Climate Change 2013: The Physical Science Basis. Contribution of Working Group I to the Fifth Assessment Report of the Intergovernmental Panel on Climate Change, Cambridge University Press, Cambridge, United Kingdom and New York, NY, USA, https://doi.org/10.1017/CBO9781107415324.004, 2013.

Karstens, U., Simmer, C., and Ruprecht, E.: Remote sensing of cloud liquid water, Meteorol. Atmos. Phys., 54, 157–171, https://doi.org/10.1007/BF01030057, 1994.

Kim, B.-G., Miller, M. A., Schwartz, S. E., Liu, Y., and Min, Q.: The role of adiabaticity in the aerosol first indirect effect, J. Geophys. Res.-Atmos., 113, n/a–n/a, https://doi.org/10.1029/2007JD008961, 2008.

Lebsock, M. and Su, H.: Application of active spaceborne remote sensing for understanding biases between passive cloud water path retrievals, J. Geophys. Res.-Atmos., 119, 8962–8979, https://doi.org/10.1002/2014JD021568, 2014.

Macke, A., Seifert, P., Baars, H., Barthlott, C., Beekmans, C., Behrendt, A., Bohn, B., Brueck, M., Bühl, J., Crewell, S., Damian, T., Deneke, H., Düsing, S., Foth, A., Di Girolamo, P., Hammann, E., Heinze, R., Hirsikko, A., Kalisch, J., Kalthoff, N., Kinne, S., Kohler, M., Löhnert, U., Madhavan, B. L., Maurer, V., Muppa, S. K., Schween, J., Serikov, I., Siebert, H., Simmer, C., Späth, F., Steinke, S., Träumner, K., Trömel, S., Wehner, B., Wieser, A., Wulfmeyer, V., and Xie, X.: The HD(CP)^2 Observational Prototype Experiment (HOPE) – an overview, Atmos. Chem. Phys., 17, 4887–4914, https://doi.org/10.5194/acp-17-4887-2017, 2017.

Merk, D., Deneke, H., Pospichal, B., and Seifert, P.: Investigation of the adiabatic assumption for estimating cloud micro- and macrophysical properties from satellite and ground observations, Atmos. Chem. Phys., 16, 933–952, https://doi.org/10.5194/acp-16-933-2016, 2016.

Miller, D. J., Zhang, Z., Ackerman, A. S., Platnick, S., and Baum, B. A.: The impact of cloud vertical profile on liquid water path retrieval based on the bispectral method: A theoretical study based on large-eddy simulations of shallow marine boundary layer clouds, J. Geophys. Res.-Atmos., 121, 4122–4141, https://doi.org/10.1002/2015JD024322, 2016.

Min, Q., Joseph, E., Lin, Y., Min, L., Yin, B., Daum, P. H., Kleinman, L. I., Wang, J., and Lee, Y.-N.: Comparison of MODIS cloud microphysical properties with in-situ measurements over the Southeast Pacific, Atmos. Chem. Phys., 12, 11 261–11 273, https://doi.org/10.5194/acp-12-11261-2012, 2012.

Mlawer, E. J., Taubman, S. J., Brown, P. D., Iacono, M. J., and Clough, S. A.: Radiative transfer for inhomogeneous atmospheres: RRTM, a validated correlated-k model for the longwave, J. Geophys. Res.-Atmos., 102, 16 663–16 682, https://doi.org/https://doi.org/10.1029/97JD00237, 1997.

Nakajima, T. and King, M. D.: Determination of the Optical Thickness and Effective Particle Radius of Clouds from Reflected Solar Radiation Measurements. Part I: Theory, J. Atmos. Sci., 47, 1878–1893, https://doi.org/10.1175/1520-0469(1990)047<1878:DOTOTA>2.0.CO;2, 1990.

Oreopoulos, L. and Barker, H. W.: Accounting for subgrid-scale cloud variability in a multi-layer 1d solar radiative transfer algorithm, Q. J. Roy. Meteor. Soc., 125, 301–330, https://doi.org/10.1002/qj.49712555316, 2006.

Petty, G. W. and Huang, W.: The Modified Gamma Size Distribution Applied to Inhomogeneous and Nonspherical Particles: Key Relationships and Conversions, J. Atmos. Sci., 68, 1460–1473, https://doi.org/10.1175/2011JAS3645.1, 2011.

Pincus, R. and Baker, M. B.: Effect of precipitation on the albedo susceptibility of clouds in the marine boundary layer, Nature, 372, 250–252, https://doi.org/10.1038/372250a0, 1994.

Pincus, R., Barker, H. W., and Morcrette, J.-J.: A fast, flexible, approximate technique for computing radiative transfer in inhomogeneous cloud fields, J. Geophys. Res.-Atmos., 108, https://doi.org/10.1029/2002JD003322, 2003.

Quaas, J., Boucher, O., and Lohmann, U.: Constraining the total aerosol indirect effect in the LMDZ and ECHAM4 GCMs using MODIS satellite data, Atmos. Chem. Phys., 6, 947–955, https://doi.org/10.5194/acp-6-947-2006, 2006.

Rémillard, J., Kollias, P., and Szyrmer, W.: Radar-radiometer retrievals of cloud number concentration and dispersion parameter in nondrizzling marine stratocumulus, Atmos. Meas. Tech., 6, 1817–1828, https://doi.org/10.5194/amt-6-1817-2013, 2013.

Roebeling, R., Baum, B., Bennartz, R., Hamann, U., Heidinger, A., Thoss, A., and Walther, A.: Outcome of the third cloud retrieval evaluation workshop, AIP Conf. Proc., 1531, 416–419, https://doi.org/10.1063/1.4804795, 2013.

Roebeling, R. A., Feijt, A. J., and Stammes, P.: Cloud property retrievals for climate monitoring: Implications of differences between Spinning Enhanced Visible and Infrared Imager (SEVIRI) on METEOSAT-8 and Advanced Very High Resolution Radiometer (AVHRR) on NOAA-17, J. Geophys. Res.-Atmos., 111, n/a–n/a, https://doi.org/10.1029/2005JD006990, 2006.

Schewski, M. and Macke, A.: Correlation between domain averaged cloud properties, and solar radiative fluxes for three-dimensional inhomogeneous mixed phase clouds, Meteorol. Z., 12, 293–299, https://doi.org/doi:10.1127/0941-2948/2003/0012-0293, 2003.

Seifert, A. and Beheng, K. D.: A two-moment cloud microphysics parameterization for mixed-phase clouds. Part 1: Model description, Meteorol. Atmos. Phys., 92, 45–66, https://doi.org/10.1007/s00703-005-0112-4, 2006.

Shonk, J. K. P. and Hogan, R. J.: Tripleclouds: An Efficient Method for Representing Horizontal Cloud Inhomogeneity in 1D Radiation Schemes by Using Three Regions at Each Height, J. Climate, 21, 2352–2370, https://doi.org/10.1175/2007JCLI1940.1, 2008.

Slingo, A.: A GCM Parameterization for the Shortwave Radiative Properties of Water Clouds, J. Atmos. Sci., 46, 1419–1427, https://doi.org/10.1175/1520-0469(1989)046<1419:AGPFTS>2.0.CO;2, 1989.

Stegmann, M. B., Sjöstrand, K., and Larsen, R.: Sparse modeling of landmark and texture variability using the orthomax criterion, https://doi.org/10.1117/12.651293, 2006.

Stephens, G. L., Vane, D. G., Boain, R. J., Mace, G. G., Sassen, K., Wang, Z., Illingworth, A. J., O'connor, E. J., Rossow, W. B., Durden, S. L., Miller, S. D., Austin, R. T., Benedetti, A., and Mitrescu, C. a.: THE CLOUDSAT MISSION AND THE A-TRAIN, Bull. Amer. Meteor. Soc., 83, 1771–1790, https://doi.org/10.1175/BAMS-83-12-1771, 2002.

Stuhlmann, R., Rodriguez, A., Tjemkes, S., Grandell, J., Arriaga, A., Bézy, J.-L., Aminou, D., and Bensi, P.: Plans for EUMETSAT's Third Generation Meteosat geostationary satellite programme, Adv. Space Res., 36, 975–981, https://doi.org/https://doi.org/10.1016/j.asr.2005.03.091, 2005.

Turner, D. D., Vogelmann, A. M., Austin, R. T., Barnard, J. C., Cady-Pereira, K., Chiu, J. C., Clough, S. A., Flynn, C., Khaiyer, M. M., Liljegren, J., Johnson, K., Lin, B., Long, C., Marshak, A., Matrosov, S. Y., McFarlane, S. A., Miller, M., Min, Q., Minimis, P., O'Hirok, W., Wang, Z., and Wiscombe, W.: Thin Liquid Water Clouds: Their Importance and Our Challenge, B. Am. Meteorol. Soc., 88, 177–190, https://doi.org/10.1175/BAMS-88-2-177, 2007.

Twomey, S.: The influence of pollution on the shortwave albedo of clouds, J. Atmos. Sci., 34, 1149–1152, https://doi.org/10.1175/1520-0469(1977)034<1149:TIOPOT>2.0.CO;2, 1977.

Wan, H., Giorgetta, M. A., Zängl, G., Restelli, M., Majewski, D., Bonaventura, L., Fröhlich, K., Reinert, D., Rípodas, P., Kornblueh, L., and Förstner, J.: The ICON-1.2 hydrostatic atmospheric dynamical core on triangular grids – Part 1: Formulation and performance of the baseline version, Geosci. Model Dev., 6, 735–763, https://doi.org/10.5194/gmd-6-735-2013, 2013.

Werner, F., Ditas, F., Siebert, H., Simmel, M., Wehner, B., Pilewskie, P., Schmeissner, T., Shaw, R. A., Hartmann, S., Wex, H., Roberts, G. C., and Wendisch, M.: Twomey effect observed from collocated microphysical and remote sensing measurements over shallow cumulus, J. Geophys. Res.-Atmos., 119, 1534–1545, https://doi.org/10.1002/2013JD020131, 2014.

Werner, F., Zhang, Z., Wind, G., Miller, D. J., Platnick, S., and Di Girolamo, L.: Improving Cloud Optical Property Retrievals for Partly Cloudy Pixels Using Coincident Higher-Resolution Single Band Measurements: A Feasibility Study Using ASTER Observations, J. Geophys. Res.-Atmos., 123, 12,253–12,276, https://doi.org/10.1029/2018JD028902, 2018.

Wood, R.: Relationships between optical depth, liquid water path, droplet concentration, and effective radius in adiabatic layer cloud, University of Washington, 3, 2006.

Wood, R. and Hartmann, D. L.: Spatial Variability of Liquid Water Path in Marine Low Cloud: The Importance of Mesoscale Cellular Convection, J. Climate, 19, 1748–1764, https://doi.org/10.1175/JCLI3702.1, https://doi.org/10.1175/JCLI3702.1, 2006.

Zeng, S., Riedi, J., Trepte, C. R., Winker, D. M., and Hu, Y.-X.: Study of global cloud droplet number concentration with A-Train satellites, Atmos. Chem. Phys., 14, 7125–7134, https://doi.org/10.5194/acp-14-7125-2014, 2014.

Zhang, Z., Werner, F., Cho, H.-M., Wind, G., Platnick, S., Ackerman, A. S., Di Girolamo, L., Marshak, A., and Meyer, K.: A framework based on 2-D Taylor expansion for quantifying the impacts of subpixel reflectance variance and covariance on cloud optical thickness and effective radius retrievals based on the bispectral method, J. Geophys. Res.-Atmos., 121, 7007–7025, https://doi.org/10.1002/2016JD024837, 2016.